Rock Fabric Controls on Pore Evolution and Porosity-Permeability Trends in Oolitic Grainstone Reservoirs and Reservoir Analogs

By
Hamilton Miller Goodner

Submitted to the graduate degree program in Geology and the Graduate Faculty of the University of Kansas in partial fulfillment of the requirements for the degree of Master of Science.

_____
Chair: Dr. Eugene C. Rankey

_____
Dr. W. Lynn Watney

_____
Dr. Chi Zhang

Date Defended: 29 November 2018

The Thesis Committee for Hamilton Miller Goodner certifies that this is the approved version of the following thesis:

Rock Fabric Controls on Pore Evolution and Porosity-Permeability Trends in Oolitic Grainstone Reservoirs and Reservoir Analogs

_____

Chair: Dr. Eugene C. Rankey

_____

Dr. W. Lynn Watney

_____

Dr. Chi Zhang

Date Approved: 29 November 2018

Abstract

Although the general influence of rock fabric on porosity and permeability (Φ-k) within carbonates is well documented, if and how pore evolution and Φ-k scatter quantitatively relate to depositional fabric remains poorly constrained. This project empirically explores this uncertainty within oolitic grainstones from a range of geologic ages and diagenetic histories to understand depositional sediment-pore relationships, and how they can evolve with lithification. Integrating data from point counting, digital image analysis, nuclear magnetic resonance and core analysis of Holocene, Pleistocene, Pennsylvanian, and Mississippian oolitic grainstones reveals quantitative relations among rock fabric, pores, and petrophysical parameters. Oolitic grainstones of similar sedimentology taken from distinct diagenetic scenarios display a unique combination of pore size, shape, spatial distribution, and Φ-k character. Within each scenario, grain size, sorting, and type are correlated more closely with pore attributes and k than cementation and compaction. Collectively, these results are interpreted to suggest that diagenesis defines the absolute values of pore attributes and petrophysical parameters, but sedimentology controls the trends or variability within an oolitic succession. The implication of these findings is that petrophysical variability within oolitic reservoirs closely follows sedimentologic trends, which may be predictable within a stratigraphic framework.

Acknowledgments

This research was funded by Kansas Interdisciplinary Carbonates Consortium at the University of Kansas and the Geological Society of America. Many have contributed to my experience and progression through the Master's program at the University of Kansas's Department of Geology. First and foremost, I am especially grateful for my advisor Gene Rankey. I am eternally grateful for him believing in me and giving me the opportunity to work under him. Gene's investment in his students' overall success is unmatched. His guidance and patience embodies the exemplary advisor. His technical and non-technical support gave me the opportunity to be successful as a geologist and person throughout life. I also recognize my advisory committee members of Drs. Chi Zhang and Lynn Watney. Chi's NMR laboratory facilities were crucial to the completion of this study, and she provided valuable guidance on petrophysical methodologies and interpretation. Lynn's experience and knowledge of Kansas geology was instrumental in shaping this study.

I thank Nikki Potter and the Kansas Geological Survey for lending their time and facilities during the selection and collection of the core samples in this study. I also would like to highlight the KGS for their exceptional organization and documentation, which provides aspiring scientists with the public resources and structure to contribute to the greater geoscience community. In addition, I thank Dr. Jon Smith at the KGS for allowing me to use his petrographic facilities, which allowed me to obtain data that was fundamental to this study. I am also grateful for the fellow students in Dr. Rankey's research group, who provided countless conversations, brainstorms, and feedback that helped me progress throughout my time at KU.

I cannot conclude without thanking my friends and family. My friends at KU kept me positive and productive during these past few years, and I will always think fondly on my time in Lawrence. My family kept me grounded and never allowed me to lose sight of who I am despite the anxiety, pressure, and loneliness which can sometimes accompany graduate school. I am extremely grateful for their tremendous love and support from states away. In no small part are they responsible for the man I have grown to be and the work I produce.

Table of Contents

Abstract ..... **iii**

Acknowledgments ..... **iv**

List of Figures and Tables ..... **viii**

Introduction **1**

Background **2**

Methods **4**

Sample Collection and Preparation *4*

Characterization of Rock Fabric *4*

Characterization of Pore Attributes *6*

Characterization of Porosity and Permeability *10*

Results **11**

Sedimentologic and Diagenetic Variability among Sample Groups *11*

Comparison of Pores and Φ-k among Sample Groups *12*

Depositional Fabric: Influence on Pore Attributes *14*

Pore Attribute Controls on Φ-k *16*

Sedimentologic Controls on Φ-k *18*

Discussion **19**

Implications **26**

Conclusions **30**

References Cited **32**

Figures **42**

Tables **54**

Appendices **57**

Appendix 1: Results of Multivariate Linear Regression *57*

Appendix 2: Raw Data from Holocene Samples *58*

Appendix 3: Raw Data from Pleistocene Samples *64*

Appendix 4: Raw Data from Pennsylvanian Samples *74*

Appendix 5: Raw Data from Mississippian Samples *83*

List of Figures and Tables

FIGURES

Figure 1 – Illustrative thin section photos of sedimentologic and diagenetic variability

Figure 2 – Quantitative data on variability of rock fabric among samples

Figure 3 – Thin section photos of representative samples and associated NMR T_2 curves

Figure 4 – Digital image analysis data characterizing pore size and shape

Figure 5 – Lacunarity data and illustrative examples

Figure 6 – Scatterplot of porosity and permeability data

Figure 7 – Photomicrographs and NMR T_2 curves of illustrative Holocene sediment

Figure 8 – Quantitative relations among rock fabric and pore attributes in lithified sample groups

Figure 9 – Photomicrographs and NMR T_2 curves of samples with permeability varying 3+ orders of magnitude

Figure 10 – Scatterplots of pore attributes and permeability

Figure 11 – Scatterplots and correlation coefficients revealing quantitative relations between depositional fabric and permeability

Figure 12 – Photomicrographs and scatterplots illustrating relations among depositional fabric, pores, and Φ-k across diagenetic scenarios

TABLES

Table 1 – Sedimentologic, stratigraphic, and diagenetic character of sample groups

Table 2 – Definitions of pore attributes defined by digital image analysis

Table 3 – Data types used throughout the study

Introduction

Many prolific hydrocarbon reservoirs produce from carbonate strata, but carbonate reservoir characterization can prove challenging due to complex pore networks. In seeking to understand the controls on these pore networks, numerous studies have documented variations in porosity and permeability (Φ-k), and how these relate to carbonate rock fabrics (Lucia 1983, 1995, 1999; Jennings and Lucia, 2001; Cruz et al., 2006; Lønøy 2006), integrating parameters such as particle size (Lucia, 1983; Jennings and Lucia, 2001) or depositional texture (Jones and Xiao, 2006). These and other studies of carbonate pores commonly assume part or all of a logical linkage: a) rock fabric defines pore attributes (e.g., pore-size distribution); b) pore attributes control permeability; and c) as a result, rock fabric controls permeability (Enos and Sawatsky, 1981; Lucia, 1983, 1995, 1999; Melim et al., 2001; Weger et al., 2009).

As rock fabric is shaped by depositional aspects (e.g., grain size, sorting, and type) and diagenetic attributes (e.g., cement abundance, compaction porosity loss), a question of "nature or nurture?" commonly arises. Are pore networks (and, subsequently, Φ-k) controlled more by their sedimentary starting point (i.e., the attributes of sedimentologic components) or by the changes they undergo (i.e., diagenetic modifications)? Carbonate rocks can display pronounced diagenetic overprinting; thus, the links from depositional attributes to petrophysics have the potential to be tenuous. Perhaps as a result, efforts to systematically and quantitatively link attributes of depositional fabric (primary sedimentologic components; Choquette and Pray, 1970) to pores, and further, to petrophysical variability, are few.

To explore these challenges, this project quantitatively tests two linked hypotheses: **1) varied depositional fabrics correlate to distinct pore attributes;** and **2) pore attributes and total**

porosity control permeability. To explore these hypotheses and unravel rock fabric-pore attribute links, and pore attribute-k links, this project examines oolitic grainstones, a class of deposits present in carbonate accumulations of almost every geologic age. Oolitic deposits also represent important hydrocarbon reservoirs across the globe, from the U.S. Midcontinent (Watney and French, 1988; Abegg, 1991) and Gulf Coast (Melas and Friedman, 1992) to the Middle East (Lindsay et al., 2006; Esrafili-Dizaji and Rahimpour-Bonab, 2014; Hollis et al., 2017) and Far East (Ma et al., 2011). This study statistically integrates results from petrographic point counting, digital image analysis (DIA), nuclear magnetic resonance (NMR), and core analysis. Characterizing strata from a range of ages, the ultimate goal is to resolve the degree to which relationships among sedimentology, pores, and petrophysical responses are maintained in oolites that have undergone a range of diagenetic histories. The results illustrate how different depositional properties can influence petrophysical trends and heterogeneity within comparable oolitic reservoirs, information pivotal to advancing conceptual understanding and quantitative models of oolitic carbonate reservoirs.

Background

This study examines four groups of samples which represent distinct diagenetic settings (Figure 1; Table 1) but include similar ranges of sedimentologic character (i.e., granulometry, grain type proportions) (Figure 2). These four sample groups could be considered distinct diagenetic 'scenarios': un-lithified sediment, early diagenesis, and two distinct late diagenetic end members. Together, these groups represent "snapshots" along potential diagenetic pathways, facilitating understanding of original pores and how they can be modified by diagenesis. Not every possible

diagenetic scenario is included, however, and certainly other diagenetic pathways could be considered.

The sediment and rock samples include a range of sedimentologic, stratigraphic, and diagenetic character (Table 1; Figures 1, 2). Holocene samples are unlithified oolitic sediment (i.e., the starting point for all oolitic grainstones) from Schooner Cays, Great Bahama Bank and Fish Cays, Crooked-Acklins Platform, Bahamas (Ball, 1967; Rankey and Reeder, 2011, 2012; Huber, 2016; Rush and Rankey, 2017) (Table 1; Figure 1A, B). Pleistocene samples are lithified strata from Long Cay and Crooked Island, Crooked-Acklins Platform, Bahamas, units which have been exposed to marine and early meteoric diagenetic alterations (shallow burial [< 10m], low to moderate cementation [16.9% cement by volumetric abundance]) (Table 1) (A. Goers, 2018, personal communication). These rocks were deposited as dominantly aragonitic sediment, and their mineralogy has stabilized only partly. Cementation has occluded pores incompletely, and dissolution has created pores within grains (e.g., dissolved ooid laminae) and enlarged pre-existing pores (Figure 1C, D). These samples display pore systems that include a mix of interparticle pores, moldic pores, and microporosity. Pennsylvanian samples are from reservoir intervals (Bethany Falls Limestone, Missourian Lansing-Kansas City Group) in multiple fields in Kansas (Watney and French, 1988; French and Watney, 1993; Byrnes et al., 2003) (Table 1). These rocks likely also were deposited as aragonitic sediment (e.g., Sandberg, 1983) but, after extensive dissolution and cementation, now display well-developed moldic pores and some relict interparticle pores. Oomolds are generally large (commonly hundreds of microns) and isolated; they may be crushed or preserved as round to oval shapes (Figure 1E, F). As Pennsylvanian samples represent a moldic end member oolitic reservoir, they are distinct from Mississippian

samples (Abegg, 1991; Parham and Sutterlin, 1993) which display well-connected interparticle pores. These samples were taken from the St. Louis B interval in productive fields in Southwest Kansas (Qi and Carr, 2005) and were deposited as dominantly calcitic sediment (e.g., Sandberg, 1983), which is less susceptible to dissolution, preserving grains and much of the primary interparticle porosity (Figure 1G, H). These rocks are broadly comparable to that of the Holocene in terms of grain condition and pore type, but have undergone various degrees of cementation and compaction.

The samples from the Pennsylvanian and Mississippian intervals focus on porous zones within reservoirs, and do not include tight zones. Furthermore, samples from all groups were selected to avoid fractures and touching vugs (non-fabric selective, interconnected pores; Lucia, 1995), which can also impact permeability.

Methods

Sample Collection and Preparation

Holocene sediment (n = 12) samples were collected at the sediment-water interface, whereas Pleistocene (n = 19) rocks were taken from outcrops as hand samples. Downhole cores provided Mississippian (n = 18) and Pennsylvanian (n = 17) samples. One-inch (2.54 cm) diameter plugs from hand samples or cores included ends that provided billets for thin sections. Billets were impregnated with blue epoxy and subsequently cut for standard thin section preparation.

Characterization of Rock Fabric

This study uses the term *rock fabric* to describe the solid constituents of a sediment or rock (Choquette and Pray, 1970). Genetically, rock fabric includes both depositional (sedimentologic) and diagenetic components. *Depositional fabric* refers to the characteristics of primary sedimentologic components (e.g., grain size), whereas characteristics of diagenetic origin are termed *diagenetic attributes*.

To characterize the rocks, quantitative digital petrography using JMicroVision captured grain-size distribution. Using this program, 100 grain-size measurements were taken at randomly generated points on thin section images. As grain-size measurements extracted from thin sections are apparent sizes, they require conversion to be compared to sieve distributions of sediment samples (Flugel, 2010). This study implements the regression model of Merta (1991) to transform thin section distributions to sieve-size distributions. The cumulative frequency curves of these distributions facilitate the graphical extraction of graphic mean size ("grain size"), inclusive graphic standard deviation ("sorting"), inclusive graphic skewness ("skewness"), and graphic kurtosis ("kurtosis") (Folk and Ward, 1957; Flugel, 2010). These quantitative measurements were confirmed qualitatively against comparative grain-size and sorting charts. Grain size data presented herein use Udden size divisions with the Krumbein phi scale (Udden, 1914; Krumbein, 1939).

Point counting included grain type quantification. Using a mechanical petrographic stage programmed for regular grid stepping, at least 300 observations per thin section differentiated ooids, composite grains, peloids, and various skeletal grains. In addition to grain type, point counting facilitated the quantification of diagenetic parameters such as cement abundance and intergranular volume (IGV). To characterize compaction, the relative abundance of grains,

interparticle cement, and interparticle porosity were documented, which was then used to calculate a compaction index ("COPL" in Lundegaard, 1992; Budd 2002):

$$COPL = P_i - ((100 - P_i) * IGV / (100 - IGV))$$

COPL estimates interparticle porosity loss due to compaction. $\mathbf{P_i}$ represents an assumed value of initial interparticle porosity, herein assumed to be 43%. This value is consistent with porosity data for sedimentologically similar oolitic samples in Enos and Sawatsky (1981) and the NMR porosity data of Holocene sediment samples presented herein. Fractures and stylolites are also documented, but generally are absent or very rare.

Characterization of Pore Attributes

Pore attributes such as pore size, shape, spatial distribution, and type are quantified using point counting, nuclear magnetic resonance (NMR), and digital image analysis (DIA). Point counting differentiated the proportions of pore types. The dominant pore types (Choquette and Pray, 1970) in these strata include interparticle, intraparticle, and moldic.

NMR provides bulk-property, three-dimensional estimations of porosity and pore-size distribution (Coates et al., 1999; Song, 2013). During experiments, the NMR machine repeatedly transmits a magnetic pulse through fluid-saturated sediment or rock samples. After each pulse, a receiver records the decay of resonating hydrogen ions in the pore fluids in the form of an echo decay (Coates et al., 1999). These echo decays provide a multitude of information about pore networks. This study utilizes T_2 relaxation (transverse-relaxation-time) curves, which describe the time record of the full spectrum of decay signals (Coates et al., 1999). T_2 data are common in both laboratory and borehole settings (NMR logs). Typically, T_2 curves plot relaxation time

against amplitude, so that the area under the curve equals the initial amplitude of the echo decay, thus providing a measure of total porosity (Coates et al., 1999). The full spectrum of relaxation times serves as a crude proxy for a pore-size distribution (T_2 time ≈ pore size) (Coates et al., 1999; Vincent, 2011; Song, 2013). These T_2 relaxation curves (time domain) may be used to calculate pore-size distributions (length domain) quantitatively, by using certain calibrations and assumptions which may or may not hold for carbonate strata (Brownstein and Tarr, 1979; Godefroy et al., 2001; Vincent et al., 2011). As such, this study presents T_2 relaxation times instead of pore-size distributions. Relaxation times are plotted on a logarithmic scale against porosity units (cf. Westphal et al., 2005). From these T_2 distributions, certain pore attributes can be extracted, including modal time (T_2 Mode; cf. Doveton and Watney, 2014), mean time (logarithmic), curve peakedness (T_2 Kurtosis), total porosity, and macro-/micro-porosity.

Prior to laboratory NMR analysis, all sediment samples and plugs from core and outcrop were dried for at least 24 hours at 60°C. Dried samples were weighed, subsequently saturated with deionized water under vacuum conditions for 10 hours, and then weighed again using a water displacement method. Bulk volume calculated from these measurements provided input for each NMR experiment. Samples were wrapped in Teflon tape during experiments to prevent water loss. NMR experiments utilized a Magritek 2MHz NMR Rock Core Analyzer, and all experiments attained a signal-to-noise ratio (SNR) of at least 100:1.

Digital image analysis (DIA) includes a suite of methods to quantify attributes of pores, such as size, shape, and spatial distribution (Ehrlich et al., 1984; Fortey, 1995; Anselmetti et al., 1998; Russ, 1998; Lindqvist and Akesson, 2001; Weger et al., 2009) from digital images of thin sections. Herein, DIA analyses generally mimic the methodology outlined in Weger (2006), and

include three broad steps: image acquisition, pore network segmentation, and pore geometry calculations. Two-dimensional thin section images of each sample were acquired under plane-polarized light (PPL). Pore space in these images is distinguished readily because samples are saturated with blue epoxy. Through image segmentation, a binary image of the pore network was created by designating all blue pixels as pore and non-blue pixels as rock matrix. Any air bubbles were mapped as "pore" in the binary images.

DIA data used for pore geometry characterizations include two broad categories: metrics which represent the geometry of individual pores ("local parameters") and metrics which characterize the pore network as a whole ("global parameters") (Russ, 1998; Weger, 2006). ImageJ software quantifies the raw measurements of pore area, perimeter, axis lengths of bounding ellipse, and the angle between axes. These basic measurements facilitate the calculation of local parameters for each pore on each thin section image and include equivalent diameter, gamma, aspect ratio, circularity, roundness, and compactness (Weger, 2006; see Table 2 for explanations). These local parameters are summarized by statistics (e.g., mean, median, area-weighted mean) of their frequency distributions, which serve as global parameters. Additional global parameters are calculated to further describe the pore network, including: sum of pore area, sum of pore perimeters, and total perimeter over area (PoA). DomSize is a size parameter (Weger, 2006) that represents the maximum pore size required to constitute 50% of the total pore area, or the pore size at the 50% threshold of a cumulative area curve, given in equivalent diameter. Pores smaller than 100 pixels were omitted from data analysis (following Weger, 2006) to avoid distortion of geometric data by pores whose shapes may not be reliably

characterized. As Holocene samples are loose sediment disturbed by collection and absent of compaction, DIA was not applied to these samples.

Beyond pore size and shape, the spatial distribution of pores can be characterized using lacunarity analysis (Allain and Cloitre, 1991; Plotnick et al., 1993). Lacunarity is a scale-dependent measure of spatial heterogeneity, which was assessed using the FracLac plug-in for ImageJ (Karperian, 2015). Following Allain and Cloitre (1991), Plotnick et al. (1993), and Rankey (2002, 2016), binary images (pore vs. non-pore) are scanned systematically at successive scales using a gliding box algorithm. In this method, a square box of width ***r*** starts in the upper left corner of the thin section image, and the number of pixels within that box which represent pore space is documented, referred to as the box mass ***S***. The box then slides one increment to the right, again documenting ***S***. This process is repeated until all areas of the image have been analyzed. A box mass probability distribution, ***Q(S,r)***, is generated:

$$Q(S,r) = n(S,r) / N(r),$$

such that ***n(S,r)*** is the number of boxes with size ***r*** which contain a box mass ***S***, and ***N(r)*** is the total number of boxes (Plotnick et al., 1993). From this distribution, the first and second moments are calculated, representing the mean (Z1) and standard deviation (Z2), respectively. Lacunarity (***L***) of box size ***r*** is then calculated using the formula:

$$L(r) = Z2 / (Z1)^2$$

This entire process and generation of a single lacunarity value is replicated for 9 incrementally larger box sizes, with the largest box size equal to 45% of the thin section area. A single lacunarity value is the dimensionless ratio of variance to $(\text{mean})^2$ for a given box size, but ultimately is calculated across a range of box sizes.

The calculated lacunarity is a function of three factors. First, the total porosity present in a thin section: at a given box size, samples of higher porosity will exhibit lower lacunarity than lower porosity samples. Second, the box size: as box size increases, lacunarity will also decrease as the standard deviation decreases relative to the mean. Third, the "gappiness" of the pore network: for a given porosity, samples with clumped or isolated pores will exhibit higher lacunarity (Plotnick et al., 1996; Rankey, 2016). Conversely, rocks with homogenously distributed pore networks exhibit lower lacunarity.

Lacunarity data typically are presented by plotting lacunarity (in this study, 10 values for each thin section image) against box size on a log-log scale, to capture the scale dependence of the metric. In addition, to recognize lacunarity distinctions among sample groups, lacunarity values at each box size were averaged for an entire sample group, providing a "characteristic" lacunarity distribution for each group. Furthermore, to mitigate the effects of porosity differences between samples and sample groups, lacunarity distributions were normalized by dividing each value by the lacunarity at the smallest box size. Where correlations of linear regressions required a singular lacunarity value, the value at the smallest box size was chosen.

Across these analysis methods, pore attributes can be categorized by what they describe about a pore (Table 3). For example, modal pore size or DomSize characterize pore size. Compactness or circularity characterize pore shape, and lacunarity assesses the spatial distribution of pores.

Characterization of Porosity and Permeability

Routine core analysis measured Helium porosity (%), air permeability (md), and grain density (g/cm^3) for Pleistocene (n = 13), Pennsylvanian (n = 16), and Mississippian (n = 16) rocks. Some samples were unfit for analysis due to laboratory restrictions or sample quality (e.g., irregular plug shape or poor lithification), and thus, do not have Φ-k data.

These Φ-k measurements are supplemented by NMR and DIA data. NMR T_2 curves provide porosity data, and a T_2 cutoff (Coates et al., 1999) distinguishes micro- and macroporosity contributions. Microporosity has been defined using any of a variety of criteria (summarized in Vincent et al., 2011), and many studies have investigated the T_2 cutoffs that distinguish microporosity from macroporosity (Coates et al., 1999; Al-Marzouqi et al., 2010; Vincent et al., 2011). This study implemented a microporosity-macroporosity cutoff of 100 milliseconds (cf. Coates et al., 1999), corresponding roughly to a 5 micron pore (Al-Marzouqi et al., 2010). Porosity derived from NMR is typically 3-4% porosity less than that from Helium analysis of samples herein. Image analysis also provides porosity estimates, but DIA does not reliably resolve microporosity as defined in this study, because those pores are below the resolution of the thickness of the thin section (32 μm).

Results

Sedimentologic and Diagenetic Variability among Sample Groups

Petrographic point counting quantifies the sedimentologic and diagenetic character of the four sample groups (Figure 2). Samples are fine to coarse grained and moderately to very well sorted. Ooid abundance typically is greater than 50%. Pleistocene samples have undergone relatively low cementation (reported as the percentage of the intergranular volume [IGV] occupied by

cement) and compaction (reported as interparticle porosity loss due to compaction, COPL). Pennsylvanian samples include the greatest cementation but low compaction, whereas Mississippian samples display relatively moderate cementation and high compaction.

Comparison of Pores and Φ-k among Sample Groups

T_2 distributions of representative samples from each sample group (Figure 3) reveal the general characteristics of the distinct pore-size distributions among groups. For example, Holocene samples (n = 12) exhibit unimodal distributions with high-amplitude peaks (> 1 porosity units) in the macroporosity domain (average modal time = 563 ms), and total porosity averages 43.6%. T_2 curves of Pleistocene samples (n = 15) are more complex, and commonly include bimodal distributions with low-amplitude T_2 peaks (~0.5 porosity units) and modal T_2 times in the macro-porosity domain that are slightly smaller than Holocene sediment (average = 502 ms). Average total porosity is 34.6%. The peaks in the microporosity domain are pronounced, and microporosity commonly contributes more than 50% of total porosity.

In contrast, Pennsylvanian samples (n = 12) exhibit unimodal T_2 curves dominated by macroporosity. Curves include moderate to high amplitude (> 0.5 porosity units) peaks with large modal relaxation times (average = 1.4 s), and an average total porosity of 20.0%. T_2 curves of Mississippian oolites (n = 17) are consistently unimodal with low amplitude peaks (< 0.5 porosity units) at large relaxation times (average = 1.1 s) and an average total porosity of 14.1%.

Quantitative pore attributes calculated using digital image analysis reveal differences in pore size, roundness, and spatial distribution in all three rock groups (Figures 4, 5). Pores of Pleistocene samples are moderate in size (average DomSize = 131 µm) and exhibit low roundness

(average = 0.53). In contrast, Pennsylvanian samples included larger (average DomSize = 189 μm) and rounder (average roundness = 0.58) pores, and Mississippian samples have the smallest (average DomSize = 84 μm) pores with relatively low roundness (average roundness = 0.53) (Figure 4).

Pores are not uniformly distributed. Some samples (Figure 5A) include small pores that are evenly distributed, whereas others include larger pores which are more clumped (Figure 5B). The metric of lacunarity provides a means to quantify spatial heterogeneity in pores across a range of scales. Analysis of samples reveals a range of lacunarity among individual samples. In samples with similar porosity, pore networks which are more evenly distributed exhibit lower lacunarity (Figure 5A-C).

However, not all samples have similar porosity. In fact, differing total porosity among sample groups (e.g., Figure 3) is just one factor that contributes to each group displaying distinct average lacunarity distributions (Figure 5D). To mitigate the effects of differing porosity, normalized lacunarity distributions were also compared (Figure 5E). Data reveal pores of Pennsylvanian samples display relatively high lacunarity (i.e., isolated oomolds), whereas Mississippian samples include lowest lacunarity (i.e., evenly distributed intergranular pores). In contrast, Pleistocene samples display relatively low lacunarity at box sizes < 7,000 μm^2 (i.e., an even distribution similar to Mississippian examples), but have relatively high lacunarity at larger scales (i.e., clumped distribution akin to Pennsylvanian examples).

A plot of porosity versus permeability reveals that each sample group falls in distinct regions (Figure 6), akin to the data of Byrnes et al. (2003), which are also plotted. Pleistocene rocks (n = 9) have high porosity (25.2 – 38.3%) and generally high permeability (70 md – 12.9 d)

but include scatter on Φ-k plots. Pennsylvanian samples (n = 15) display variable porosity (6.3 – 30.0%) and generally low but variable permeability (0.02 – 145 md). Pennsylvanian data broadly represent an extension of the Pleistocene Φ-k trend (consistent with Cruz et al., 2006). In contrast, Mississippian samples (n = 16) display a distinct trend, with low to moderate porosity (9.6 – 21.2%) and moderate to high permeability (37 – 1134 md), higher than Pennsylvanian samples of comparable porosity.

Depositional Fabric: Influence on Pore Attributes

The oolitic grainstones exhibit variability in terms of size, shape, and spatial distribution of pores (Figures 4, 5), distinctions that might be related to sedimentology. For example, within the simplest case (uncemented Holocene sediment), fine-grained samples with low ooid abundance exhibit modal pore sizes smaller than coarse-grained samples with higher ooid abundance (Figure 7A-C). A three-dimensional scatterplot visually reflects how differences in grain size and ooid abundance are accompanied by changes in modal pore size (Figure 7D).

These qualitative relationships can be quantified using multivariate linear regression by modeling the relationship between several independent variables (metrics of depositional fabric) and a dependent variable (e.g., one of the various attributes of pores or porosity). For example, in these Holocene sediment samples, metrics of depositional fabric (including of grain size, sorting, ooid abundance and skeletal abundance) are correlated statistically (R^2 = 0.92) with modal pore size (cf. Figure 7D). These parameters also influence the range of pore sizes (T_2 Kurtosis; R^2 = 0.83) and total abundance of macro-porosity (R^2 = 0.69). These relations quantify the qualitative observations that uncemented samples with larger grain sizes, better sorting, and

higher ooid abundance exhibit higher porosity (cf. Beard and Weyl, 1973), larger pores, and peaked (i.e., high kurtosis) pore-size distributions.

In lithified rocks, rock fabric is more complicated because it represents a combination of both depositional and diagenetic components. Pleistocene pore networks reveal the effects of early diagenetic alterations, with pore-size distributions that are complex and commonly bimodal (e.g., Figure 3). Despite these changes in the pore-size distribution, the modal macro-pore size is influenced by depositional fabric, as is pore complexity (i.e., perimeter over area) (Figure 8A-B). Fine-grained, poorly sorted rocks exhibit complex pore networks (high PoA); samples with larger grain size and increased sorting include simpler pores (low PoA). Multivariate regression quantifies these relationships and reveals that attributes of Pleistocene depositional fabric exhibits significant ($P < 0.05$) quantitative relationships with pore size (measured as T_2Mode, $R^2 = 0.63$) and pore complexity (PoA, $R^2 = 0.81$) (Figure 8B, blue bars). To assess the combined influence of sedimentology and diagenesis on pores, regressions included both depositional fabric and diagenetic metrics of cement abundance (% of IGV) and compaction porosity loss (COPL). Integrating depositional and diagenetic attributes into the regressions with T_2Mode, DomSize, and PoA increases R^2 values to at least 0.80 (Figure 8B, orange bars).

Pennsylvanian samples are dominated by oomoldic pores, created by dissolution of ooids (Figures 1, 3C). Thus, it is not surprising that pore size generally increases with grain size (Figure 8C). Metrics of depositional fabric also appear to influence the spatial distribution of pores in Pennsylvanian samples. Higher ooid abundance is associated with higher porosity and lower lacunarity (i.e., a more evenly distributed pore network). Multivariate regression reveals depositional fabric correlates with pore size, complexity, and lacunarity (Figure 8D), each with a

R^2 of at least 0.55. Including cementation and compaction porosity loss as inputs in the pore attribute regressions boosts correlations only marginally to between 0.58 and 0.78.

Similar to Pennsylvanian samples, pore sizes of Mississippian samples generally increase with larger grain size. Differing pore sizes also coincide with changes in grain type: rocks with a higher ooid abundance correspond to larger pores (Figure 8E). Depositional fabric exhibits significant statistical relationships with not only pore size, but also pore complexity and lacunarity (R^2 > 0.54 for all) (Figure 8F; Appendix 1). Including diagenetic factors of cementation and compaction increases the R^2 of all three correlations, ranging from 0.65 to 0.91.

Pore Attribute Controls on Φ-k

Porosity and permeability data reveal that each sample group displays distinct character on Φ-k plots (Figure 6). Pore-size distributions, one means to characterize pores, are approximated through NMR T_2 curves. T_2 curves of Pleistocene samples indicate bimodal distributions revealing variable but pronounced (commonly > 50% of total Φ) contributions from microporosity (T_2 < 100ms) (Figure 3). The bimodal Pleistocene T_2 curves are distinct from curves of Pennsylvanian and Mississippian samples, which generally display similar unimodal distributions with large (> 1 s) modal relaxation times (Figure 3).

Additionally, an explicit comparison of Pennsylvanian and Mississippian samples of comparable total porosity (Figure 9) reveals similarity among T_2 curves across a range of permeability. This observation of similar T_2 curves, which suggests similar pore-size distributions, in samples with distinct permeability is surprising because pore-size distributions have been interpreted to control permeability (e.g., Lucia, 1983). That rocks with visually comparable T_2

curves (and presumably, pore-size distributions) include permeabilities spanning more than three orders of magnitude suggests that pore attributes other than pore-size distribution impact permeability (cf. Bliefnick and Kaldi, 1996; Melim et al., 2001; Weger et al., 2009).

To assess the influence of pore attributes other than pore-size distribution on permeability, analyses also explicitly related pore geometry and spatial distribution to permeability variations. Linear regressions reveal that pore complexity is the single parameter correlated most closely with k for Pleistocene samples (R^2 = 0.74), followed by intergranular porosity (R^2 = 0.61) and pore size (R^2 = 0.57). A 3D scatterplot (Figure 10A) illustrates that samples with low pore complexity, large pore sizes, and abundant intergranular porosity have high permeability. A multivariate linear regression including those three pore attributes to estimate permeability indicates an R^2 of 0.90 in Pleistocene rocks.

Pennsylvanian samples include somewhat different trends. Total porosity (NMR) displays the strongest correlation with k (R^2 = 0.67). Factoring in pore circularity and complexity as independent variables in a regression with permeability yields an R^2 of 0.84. These results demonstrate that Pennsylvanian samples with high porosity, circular pores, and low pore complexity include high permeability (Figure 10B). In Mississippian samples, porosity (He) exhibits the strongest correlation of any individual parameter with permeability (R^2 = 0.64), but pore size and spatial distribution are also correlated (R^2 of 0.60 and 0.49, respectively). Rocks with high porosity and large, evenly distributed pores yield high permeability (regression among these parameters has R^2 of 0.88; Figure 10C).

Some pore attributes consistently yield a statistically significant relationship with permeability across all sample groups. For example, abundant macroporosity and circular (high

circularity) pores favor elevated permeability in all groups (Appendix 1). However, the pore attributes which are most closely correlated with k varies among ages, suggesting that certain pore attributes are more important in some sample groups than others. For example, pore size shows no statistically significant relationship with k in Pennsylvanian samples (R^2 = 0.02, P = 0.60), but it correlates to permeability of Mississippian samples (R^2 = 0.60, P = 0.0004) (Appendix 1).

Sedimentologic Controls on Φ-k

These results show the relations between depositional fabric and pore attributes, and among pore attributes and porosity and permeability. The question remains: is there a direct link from depositional fabric to Φ-k? In short, the answer appears yes, as metrics of depositional fabric correlate to permeability in Pleistocene (R^2 = 0.73), Pennsylvanian (R^2 = 0.50), and Mississippian (R^2 = 0.68) samples (Figure 11). The details of which parameters are most relevant do vary among sample groups, however. For example, in terms of individual parameters, grain size and ooid abundance are the parameters of Pleistocene depositional fabric most closely correlated to permeability: coarse grained deposits with high ooid abundance display high permeability (Figure 11A). Although Pennsylvanian samples display more variability in permeability than Pleistocene samples, their sedimentologic attributes also correlate with permeability. In contrast to Pleistocene samples, sorting has an impact greater than grain size on permeability, and well-sorted samples with high ooid abundance yield the highest permeability (Figure 11B). Interestingly, although they include pore types distinct from Pennsylvanian samples, Mississippian samples document similar relationships, with well-sorted samples with high ooid abundance displaying high permeability (Figure 11C). Including the diagenetic attributes of

cement abundance and compaction strengthens correlations within each sample group only marginally, increasing the R^2 between 0.12 and 0.15 (Figure 11).

Although the specific metrics of depositional and diagenetic variability that are most strongly related to pore attributes and on to permeability are distinct among sample groups, one link appears consistent. In each, ooid abundance and sorting are related to lacunarity (Figure 12A) - higher ooid abundance and better sorting result in lower lacunarity, or more evenly distributed pore networks. Such relations are intuitive for samples both with interparticle pores and moldic pores. These relations can be extended to permeability, as well. A plot of lacunarity, pore compactness, and k illustrates that samples with compact and evenly distributed pores have high k (Figure 12B). These findings indicate a linkage of depositional fabric to pore attributes, and pore attributes to permeability across several diagenetic scenarios.

Discussion

Oolitic grainstones have excellent reservoir potential at the time of deposition; however, as diagenesis ensues, pore structure and connectivity can vary widely (Hollis et al., 2017). To address this variability, this study examines oolitic samples from multiple geologic ages that represent a range of diagenetic scenarios (i.e., deposition, early lithification, and two distinct late diagenetic pathways). In doing so, it tests the hypothesis that varied depositional fabrics correlate to changes in pore attributes, and those variations in pore attributes control differences in permeability.

Although the absolute magnitude of influence of specific sedimentologic attributes (e.g., grain size, sorting, or type) changes among sample groups, these measures exhibit statistically significant relationships with the size, shape, spatial distribution, and abundance of pores in all groups (Figure 8). In Holocene examples, distinctions in depositional fabric correspond to changes in pore-size distributions, revealing that depositional fabrics control initial pore networks. These depositional fabrics and associated pore networks are the framework for subsequent modification via diagenesis.

In the early stages of diagenesis, depositional fabric retains an imprint on pore attributes, but the influence of diagenesis is also evident. For example, T_2 curves of Pleistocene samples include bimodal distributions, reflecting partial ooid dissolution, but the mode of macro-pore sizes also correlates to metrics of depositional fabric (R^2 = 0.63). These data quantify the qualitative observation that the sizes and types of grains impacts the size and shape of pores between those grains (Figure 2).

Pennsylvanian samples experienced extensive diagenetic modification, in many cases resulting in an almost complete inversion of the rock matrix and pore network. Yet, depositional fabrics display statistical correlations with pore size, complexity, and lacunarity, probably because many pores simply are former grains. Perhaps surprisingly, because they are arguably the most diagenetically altered sample group, accounting for diagenesis (e.g., cement abundance and compaction porosity loss) boosts R^2 values less in Pennsylvanian samples than in other sample groups. One possible reason why "diagenesis" (as measured here) has a limited influence on pore attributes is that the intergranular space in most of the Pennsylvanian samples is filled almost entirely with cement (Figure 2B, average = 93%). As such, the sample set does not provide

much variability, differences which could drive statistical distinctions in pore attributes. Alternatively, the Pennsylvanian samples herein show relatively limited compaction, and only 10.4 % compaction porosity loss on average (Figure 2B). Thus, it is not surprising that compaction – as measured here – does not have a marked statistical influence on prediction of pore attributes or permeability. Nonetheless, other studies have documented the role of compaction and crushed molds in markedly enhancing permeability (e.g., Byrnes et al., 2003; Poteet, 2007). Perhaps using different metrics or a broader range of samples would reveal more subtle associations.

As they are dominated by well-connected interparticle pores rather than isolated moldic pores, Mississippian samples represents a rock type that contrasts markedly with Pennsylvanian oomoldic samples. Similar to Holocene examples, the sizes and shapes of grains have a direct impact on the attributes of intergranular pores. Thus, despite considerable compaction and cementation, metrics of depositional fabric display statistically significant correlations to pore attributes describing pore size, complexity, and lacunarity.

These results are consistent with numerous studies on siliciclastic and carbonate sediment which illustrate how depositional fabrics can control original pore networks (Krumbein and Monk, 1942; Beard and Weyl, 1973; Enos and Sawatsky, 1981; Sprunt et al., 1993). For example, Krumbein and Monk (1942) and Sprunt et al. (1993) demonstrated that permeability of unconsolidated siliciclastic sand could be estimated reliably using grain size and sorting. Similarly, Enos and Sawatsky (1981) demonstrated that depositional porosity and permeability of carbonate sediment varies with Dunham textural classification and grain-size distribution.

Similarly, even with a complete porosity inversion, in which pores become matrix and grains become pore, sedimentary attributes can markedly influence pore attributes at a reservoir scale. For example, Byrnes et al. (2003) recognized multiple shallowing-upward cycles in a Pennsylvanian oomoldic reservoir in the Hall-Gurney Field of central Kansas. These cycles include an upward increase in grain size, sorting, and ooid abundance, and are accompanied by an upward increase in oomold pore size and total porosity. Similarly, examining the same reservoir of Hall-Gurney Field as Byrnes et al. (2003), Watney et al. (2006) demonstrated grain size distribution and grain type trends paralleled by changes in pore type. They documented an upward increase in grain size, sorting, and ooid abundance that corresponded to increased abundance of oomoldic pores. Collectively, the results document that trends between depositional fabric and pore attributes persevere across a range of diagenetic scenarios, although their absolute values do vary.

An additional goal of this study is to understand which pore attributes control permeability. Pore-throat-size distributions have been cited as a primary control on permeability (H. D. Winland, Amoco Production Co., unpublished; Pittman, 1992; Sigal, 2002). Typically, pore throats are characterized via mercury injection-capillary pressure experiments, which can be expensive and are limited to laboratory measurements of cored samples. In efforts to conserve cost and time, numerous methods more readily applied can estimate permeability. NMR, a relatively cheap and fast, non-invasive technique which can be undertaken using downhole logs in the absence of core, has been utilized to estimate permeability by several models (most notably, “Coates” in Coates et al., 1999; “SDR” in Kenyon et al., 1998). Previous research on carbonate pore networks has even suggested that pore-size distribution controls permeability

(Lucia, 1983, 1995, 1999; Coates et al., 1999; Jennings and Lucia, 2001; Weger et al., 2009; Smith and Hamilton, 2014). In this context, the comparison of NMR T_2 curves and Φ-k data provides an interesting perspective. Four illustrative T_2 curves (from samples of comparable porosity) (Figure 9) are nearly identical despite permeabilities that span almost 4 orders of magnitude. These observations suggests that pore-size distributions are not sole controls on Φ-k.

These data reveal that pore-size distribution alone does not control permeability; rather, it is but one of several factors that impact permeability (Figure 10). Among sample groups, fundamental differences in the geologic nature of pore networks (Figures 1, 4, 5; Table 1) are reflected in the variability in pore attributes which most directly influence k.

An example of geologic influences is provided by the Pleistocene samples, rocks impacted only by early diagenesis. As such, the possible effects of diagenesis are developed incompletely and, in some cases, unevenly distributed. For example, cementation is uneven between laminations (Figure 1C) and ooid dissolution is incomplete (bluish hue of ooids, Figure 1D). These geologic controls are reflected in the high total porosity (average 34.6%), and microporosity that accounts for more than half of total pore volume in some samples (Figure 3E). Following Keith and Pittman (1982), Cantrell and Hagerty (1999), Byrnes et al. (2003), and Cruz et al. (2006), this microporosity may be isolated or poorly connected and thus have a negligible contribution to fluid flow. As a result, total porosity is not a significant predictor of permeability. Instead, pore complexity (PoA), pore size (DomSize), and intergranular porosity are the strongest permeability predictors (Figure 10A).

In contrast, diagenesis is more advanced in Pennsylvanian samples. A considerable portion of interparticle porosity is occluded by cement, and many ooids are dissolved completely

(e.g., Figure 1F), although neither process is universal in all samples (e.g., remnant interparticle porosity, minor grain preservation, Figure 1E). These geologic effects result in pore networks characterized by (1) a volumetric contribution from microporosity less than that in Pleistocene samples (Figure 3), and (2) large, isolated pores representing oomolds (Figure 1E, 1F, 4, 5). Because microporosity is not as prevalent, the correlation between total porosity and permeability is clearer, showing a significant, positive statistical correlation (R^2 = 0.67; P = 0.0001). Qualitatively, pore size does not appear to control pore throat size (Figure 1E, 1F), contrasting with Pleistocene and Mississippian samples in which larger pores are associated with larger throats (Figure 1C, 1D, 1G, 1H). Assuming pore throat sizes control permeability, it is no surprise that pore size of Pennsylvanian samples does not show a significant statistical relationship with permeability (R^2 = 0.03, P = 0.58). In contrast, lacunarity has a significant correlation with permeability (R^2 = 0.59, P = 0.002), suggesting that pore spatial distribution influences permeability markedly, but just a bit less than total porosity in Pennsylvanian samples.

Mississippian samples have been subjected to advanced diagenetic modifications, although the effects are distinct from Pennsylvanian strata. For example, on the whole, Mississippian samples display fewer dissolution features (e.g., moldic pores) and lower cement abundance, but commonly include well-developed compaction features (Figures 1G, 1H, 2B). As a result, many Mississippian samples include lower porosity and pores which are smaller but more evenly distributed than Pennsylvanian examples (Figures 4, 5, 6). Despite these geologic distinctions, as in Pennsylvanian samples, porosity of Mississippian samples displays the strongest relationship with permeability (R^2 = 0.64). However, in contrast to trends of Pennsylvanian samples, pore size displays a significant positive relationship with permeability (R^2

= 0.60, P = 0.0004). Similar to trends in Pleistocene samples, qualitative observations suggest that Mississippian samples with larger pores include larger pore throats (e.g., Figures 1G, 1H).

Preceding results are consistent with hypotheses that varied depositional fabrics correlate to changes in pore attributes, and pore attributes control permeability. If these concepts are valid, links between depositional fabric and permeability should be evident. Although correlations between depositional fabric and permeability are lower than those linking pore attributes and k (Figures 10, 11), sedimentologic attributes display statistically significant correlations with permeability in all three sample groups (Appendix 1). Furthermore, results are consistent with the notions articulated by Lucia (1983, 1995, 1999), Jennings and Lucia (2001), and Jones and Xiao (2006), which suggested particle (i.e., grain) size is a primary control on porosity-permeability relationships, and the shape and sorting of those particles is also important. This general concept that porosity and permeability are a function of deposition is broadly (albeit implicitly) applied in constructing facies-based geological models that use distinct Φ-k distributions for each facies (e.g., Cavallo and Smosna, 1997; Palermo et al., 2012; Rush and Rankey, 2017).

The results herein quantify how specific parameters of depositional fabric combine to influence permeability for different diagenetic scenarios. The correlations between depositional fabric and permeability for each sample group (R^2 = 0.73, 0.50, and 0.68 for Figure 10A, 10B, and 10C, respectively) are stronger than those between diagenetic attributes (compaction porosity loss, % cement) and permeability (R^2 = 0.61, 0.31, 0.41, respectively). Collectively, these results suggest that, within each sample group, depositional fabric is a more direct control on pore

attributes and permeability than diagenetic attributes, at least for those metrics considered in this study (cf. Lucia, 1983; Qiao et al., 2016; Hazard et al., 2017).

These findings do not imply that diagenesis has no role in determining rock fabric-k relationships. Diagenesis clearly impacted these samples, which include over-compacted and highly cemented rocks, as well as moldic pores (Figures 1, 2). Rather, the present-day pore network is a complex function of both the initial sedimentologic character and the changes it underwent (i.e., nature *and* nurture). For example, sedimentology defines the depositional pore network, can influence subsequent modifications, and as a result, controls the *trends or variability* of pores and Φ-k within a succession (Figures 8, 11, 12). However, as each sample group (representing distinct diagenetic scenarios) has a unique combination of pore size, shape, spatial distribution, abundance, and connectivity, diagenesis may define the *absolute values* of pore attributes and petrophysical parameters (Figures 3, 4, 5, 6). This variability in diagenesis that effects different absolute values in porosity and permeability may also explain why correlations – statistically significant within groups – lack significant correlations across groups.

Implications

Many studies have illustrated how sediment character varies in Holocene oolitic tidal sand shoals (Newell et al., 1960; Ball, 1967; Hine 1977; Harris, 1979; Reeder and Rankey, 2011; Sparks and Rankey, 2013; Rush and Rankey, 2017). In these shoals, systematic changes in sediment granulometry and grain type occur from bar crests to bar flanks, and among different geomorphic bar types (e.g., linear, parabolic, shoulder), which also include distinct internal architecture and sedimentologic character (Sparks and Rankey, 2013; Rush and Rankey, 2017). As such, Holocene

shoals appear to include systematic stratigraphic (vertical and lateral) changes in grain size, sorting and type; these type of trends can persist as sediment becomes rock (Cantrell and Walker, 1985; Evans et al. 1987; Lindsay et al., 2006; Hazard et al., 2017). These types of sedimentological changes have the potential to influence a reservoir's pore network in at least two ways.

First, sediment character defines the depositional pore network, which is the framework for subsequent modifications. This concept is consistent with data of this study (Figures 1A-B, 7), and is well documented in literature (Krumbein and Monk, 1942; Beard and Weyl, 1973; Enos and Sawatsky, 1981; Sprunt et al., 1993).

Second, sedimentologic differences can influence diagenetic processes that modify depositional pores. On a shoal scale, for example, Cantrell and Walker (1985) described an Ordovician oolite from Tennessee in which each shoal subenvironment was associated with distinct paragenetic sequences. Mobile shoal and tidal channel facies experienced extensive early marine cementation, whereas bankward, stabilized environments underwent limited early cementation and retained primary porosity into later diagenesis.

Similarly, Keith and Pittman (1982) documented trends within a Cretaceous shoal complex of the Rodessa Limestone in East Texas. This study interpreted a skeletal-rich subfacies on the flanks of the shoal to have been exposed to active circulation of marine waters, facilitating extensive cementation and porosity reduction. In contrast, the ooid-rich subfacies in the shoal crest was exposed to stagnant, near-equilibrium pore fluids, and had less cement, thus preserving porosity.

At a finer scale, Halley and Evans (1983) and Evans and Ginsburg (1987) highlighted fabric-selective diagenesis in the Pleistocene Miami Limestone. In that unit, depositional fabrics within

individual cross-bed laminae control early cementation and pore development; coarser-grained laminae commonly show less abundant cement than finer-grained laminae. This dynamic was interpreted to result from finer-grained layers that preferentially held water by capillary forces and included more possible cement nucleation sites. Their observations are consistent with data from laminated Pleistocene samples in this study, in which laminae with contrasting grain sizes commonly show differences in cementation, with the finer-grained lamina including more abundant cement and lower porosity (e.g., Figure 1C). Quantitatively, grain size in Pleistocene and Mississippian samples is inversely related to cement abundance (R^2 = 0.40 and 0.22, respectively) - not strong correlations, but they are both statistically significant (P = 0.005 and 0.05, respectively). One possible reason these correlations are not stronger stems from the metrics used in the correlations. In this study, grain size is represented by the mean of a sample's grain size distribution; however, mean grain size does not capture the bimodal distribution of grain sizes in a laminated sample. If grain size and cement abundance were compared within individual laminae, correlations would likely would be stronger. Regardless, these examples at multiple scales demonstrate how depositional fabric (and hence, Φ-k distribution) influences early fluid flow and cement nucleation sites, which in turn, can control diagenesis.

As initial sediment character controls depositional pores and influences subsequent modifications, systematic stratigraphic changes in grain size, sorting, and type have the ultimate potential to influence petrophysical properties within oolitic reservoirs (cf. Jennings and Lucia, 2001; Rankey et al., 2018).

For example, Cantrell and Walker (1985) documented an Ordovician ooid shoal complex from Tennessee in which different shoal subenvironments include distinct sedimentologic

character and display distinct paragenetic sequences and porosity preservation. Rocks interpreted to represent mobile shoal settings include coarse to very coarse, very well sorted sediment with high ooid abundance (presumably high depositional Φ-k) and experienced extensive early marine cementation. In contrast, rocks interpreted to represent a tidal channel facies are poorly sorted and include diverse grain types. The channel deposits (presumably lower depositional Φ-k) display less early marine cementation and preserve interparticle porosity. These observations are consistent with results of this study, in that sedimentologically distinct samples display differences in diagenetic effects, pore attributes, and petrophysical parameters.

In another example, Cavallo and Smosna (1997) demonstrated how porosity trends mimic depositional patterns within a Mississippian oolitic shoal system of the Appalachian basin. Environments interpreted as shoal crests are coarse, well sorted sediment with high ooid abundance and relatively high porosity. In contrast, shoal flanks include less porous interbedded packstone and grainstone of finer grain size, poorer sorting, and lower ooid abundance, and channels include non-porous bioturbated packstone. The study documented that grain size, sorting, and ooid abundance increase towards the bar center and upward within the shoal, parallel to trends in porosity. These conclusions are consistent with observations of this study which suggest increased grain size, sorting, and ooid abundance results in more favorable reservoir character.

In a third example, Esrafili-Dizaji and Rahimpour-Bonab (2014) documented detailed sedimentologic patterns and associated petrophysical responses from the Permo-Triassic Dalan and Kangan formations of Iran (Khuff equivalents). These strata include an upward increase in grain size, sorting, and ooid abundance within several shallowing-upward oolitic successions.

These sedimentologic changes are associated with concomitant upward increases in porosity and permeability within each succession. These patterns are consistent with results of this study, as samples which show increased sorting and ooid abundance display favorable pore attributes (e.g., compact, evenly distributed pores) and resultant higher permeability (cf. Figure 12).

Certainly, there are situations in which relations between depositional fabric and reservoir character do not hold. For example, Wagner and Matthews (1981) interpreted porosity distribution within the Jurassic Smackover Formation of Arkansas to be unrelated to grain size, sorting, or type. Instead, the study invoked a purely diagenetic control on petrophysical parameters. Sediment which underwent mineral stabilization prior to burial resisted compaction and preserved porosity. In contrast, sediment which had not stabilized mineralogically prior to burial experienced extensive compaction and porosity reduction. In another study of the Smackover Formation, Heydari (2003) documents an example from southern Mississippi in which diagenesis has destroyed nearly all porosity, eliminating any potential influence of depositional fabric on reservoir character.

Conclusions

This study analyzes oolitic grainstones of four geologic ages which include similar ranges of grain size, sorting, and type, but represent distinct diagenetic scenarios (e.g., deposition, early diagenesis, distinct late diagenetic pathways). These diagenetic distinctions result in each group including a unique combination of pore size, shape, spatial distribution, and connectivity. Within each scenario, metrics of depositional fabric correlate more closely to changes in pore attributes and permeability than do diagenetic attributes. Collectively, these results are interpreted to

suggest that sedimentology controls the trends or variability within a succession, but diagenesis may define the absolute values of pore attributes and petrophysical parameters. The implication of these findings is that petrophysical trends within oolitic reservoirs are driven largely by differences established at the time of deposition, which may be predictable within a stratigraphic framework.

References Cited

Abegg, F.E., 1991, Sedimentology and lithostratigraphy of the Upper Mississippian Ste. Genevieve and St. Louis Limestones, southwestern Kansas: Kansas Geological Survey, Open-File Report 91-52, p. 1-33.

Al-Marzouqi, M. I., S. Budebes, E. Sultan, I. Bush, R. Griffiths, K.B. Gzara, R. Ramamoorthy, A. Husser, Z. Jeha, J. Roth, B. Montaron, S.B. Narhari, S.K. Singh, X. Poirier-Coutansais, 2010, Resolving carbonate complexity: Oilfield Review, v. 22, p. 40-55.

Allain, C. and M. Cloitre, 1991, Characterizing the lacunarity of random and deterministic fractal sets: Physical Review A, v. 44, p. 3552-3558.

Anselmetti, F. S., S. M. Luthi, and G. P. Eberli, 1998, Quantitative characterization of carbonate pore systems by digital image analysis: AAPG Bulletin, v. 82, p. 1815–1836.

Archie, G.E., Classification of carbonate reservoir rocks and petrophysical considerations: AAPG Bulletin, v. 36, p. 278-298.

Ball, M. M., 1967, Carbonate sand bodies of Florida and the Bahamas: Journal of Sedimentary Petrology, v. 37, p. 556–591.

Beard, D.C, and P.K. Weyl, 1973, Influence of texture on porosity and permeability of unconsolidated sand: AAPG Bulletin, v. 57, p. 349-369.

Bliefnick, D.M. and J.G. Kaldi, 1996, Pore geometry: control on reservoir properties, Walker Creek Field, Columbia and Lafayette Counties, Arkansas: AAPG Bulletin, v. 80, p. 1027-1044.

Brownstein, K.R., and C. E. Tarr, 1979, Importance of classical diffusion in NMR studies of water in biological cells: Physical Review A, v. 19, p. 2446-2453.

Budd, D.A., 2002, The relative roles of compaction and early cementation in the destruction of permeability in carbonate grainstones: a case study from the Paleogene of west-central Florida, U.S.A.: Journal of Sedimentary Research, v. 72, p. 116-128.

Byrnes, A.P., E.K. Franseen, W.L. Watney, and M.K. Dubois, 2003, The role of moldic porosity in Paleozoic Kansas reservoirs and the association of original depositional facies and early diagenesis with reservoir properties: Kansas Geological Survey, Open-File Report, 2003-32.

Cantrell, D.L., and R.M. Hagerty, 1999, Microporosity in Arab Formation carbonates, Saudi Arabia: GeoArabia, v. 4, 129-154.

Cantrell, D.L., and K.R. Walker, 1985, Depositional and diagenetic patterns, ancient oolite Middle Ordovician, eastern Tennessee: Journal of Sedimentary Petrology, v. 55, p. 518-531.

Cavallo, L.J., and R. Smosna, 1997, Predicting porosity distribution within oolitic tidal bars, *in* J.A. Kupecz, J. Gluyas, and S. Bloch, eds., Reservoir quality prediction in sandstones and carbonates: AAPG Memoir 69, p. 211-229.

Coates, G.R., L. Xiao, and M.G. Prammer, 1999, NMR logging principles and applications, Houston, Halliburton Energy Services, 234 p.

Choquette, P.W., and L.C. Pray, 1970, Geologic nomenclature and classification of porosity in sedimentary carbonates: AAPG Bulletin, v. 54, p. 207-250.

Cruz, F.E., G.P. Eberli, and A.P. Byrnes, 2006, Petrophysical heterogeneity of a Pleistocene oolitic shoal: lessons for ancient reservoirs, *in* R.M. Slatt, N.C. Rosen, M. Bowman, J. Castagna, T. Good, R. Loucks, R. Latimer, M. Scheihing, R. Smith, eds., Reservoir

characterization: integrating technology and business practices: 26th Annual Research Conference: Houston, TX, GCSSEPM, p. 813-848.

Doveton, J. and W.L. Watney, 2014, Textural and pore size analysis of carbonates from integrated core and nuclear magnetic resonance logging: An Arbuckle study: Interpretation, v. 3, SA77-SA89.

Ehrlich, R., S. K. Kennedy, S. J. Crabtree, and R. L. Cannon, 1984, Petrographic image analysis, I. Analysis of reservoir pore complexes: Journal of Sedimentary Petrology, v. 54, p. 1365-1378.

Enos, P., and L.H. Sawatsky, 1981, Pore networks in Holocene carbonate sediments: Journal of Sedimentary Petrology, v. 51, p. 961-985.

Esrafili-Dizaji, B., and H. Rahimpour-Bonab, 2014, Generation and evolution of oolitic shoal reservoirs in the Permo-Triassic carbonates in the South Pars Field, Iran: Facies, v. 60, p. 921-940.

Evans, C.C., and R.N. Ginsburg, 1987, Fabric-selective diagenesis in the late Pleistocene Miami Limestone: Journal of Sedimentary Petrology, v. 57, p. 311-318.

Flügel, E., 2010, Microfacies of carbonate rocks: analysis, interpretation, and application, 2nd ed.: Berlin Heidelberg, Springer-Verlag, 984 p.

Folk, R.L., and W.C. Ward, 1957, Brazos River bar: a study in the significance of grain size parameters: Journal of Sedimentary Petrology, v. 27, p. 3-26.

Fortey, N.J., 1995, Image analysis in mineralogy and petrology: Mineralogical Magazine, v. 59, p. 177-178.

Fournier, F., M. Pellerin, Q. Villenueve, T. Teillet, F. Hong, E. Poli, J. Borgomano, P. Léonide, and A. Hairabian, 2017 (in press; preliminary version published online Ahead of Print), The equivalent pore aspect ratio as a tool for pore type prediction in carbonate reservoirs: AAPG Bulletin, doi: 10.1306/10181717058.

French, J.A., and W.L. Watney, 1993, Stratigraphy and depositional setting of the lower Missourian (Pennsylvanian) Bethany Falls and Mound Valley limestones, analogues for age-equivalent ooid-grainstone reservoirs, Kansas: Kansas Geological Survey Current Research on Kansas Geology, Bulletin 235, p. 27–39.

Godefroy, S., M. Fleury, F. Deflandre, and J.-P. Korb, 2001, Temperature effect on NMR surface relaxation: SPE Annual Technical Conference and Exhibition, New Orleans, LA, SPE 71700, 13 p.

Halley, R.B., and C.C., Evans, 1983, The Miami Limestone: A guide to selected outcrops and their interpretation: Miami Geological Society, 67 p.

Harris, P.M., 1979, Facies anatomy and diagenesis of a Bahamian ooid shoal: Sedimenta VII, 163 p.

Hazard, C.S., S.M. Ritter, J.H. McBride, D.G. Tingey, and R.W. Keach III, 2017, Ground-penetrating-radar characterization and porosity evolution of an upper Pleistocene oolite-capped depositional cycle, Red Bays, northwest Andros Island, Great Bahama Bank: Journal of Sedimentary Research, v. 87, p. 523-545.

Hollis, C., D.A. Lawrence, M. Deville de Perière, F. Al Darmaki, 2017, Controls on porosity preservation within a Jurassic oolitic reservoir complex, UAE: Marine and Petroleum Geology, v. 88, p. 888-906.

Huber, M.E., 2016, Relationships between foraminifera and geomorphology: Holocene, Crooked-Acklins Platform, southern Bahamas: Master's thesis, University of Kansas, 63 p.

Jennings, J.W., and F.J. Lucia, 2001, Predicting permeability from well logs in carbonates with a link to geology for interwell permeability mapping: SPE Annual Technical Conference and Exhibition, New Orleans, LA, SPE 71336, 16 p.

Karperian, A., 2015, FracLac for ImageJ, available online at http://rsb.info.nih.gov/ij/plugins/fraclac/FLHelp/Introduction.htm, accessed April 12, 2017.

Kenyon, W. E., P.I. Day, C. Straley, and J.F. Willemsen, 1988, A three-part study of NMR longitudinal relaxation properties of water-saturated sandstones: SPE Formation Evaluation, v. 3, p. 622-636.

Keith, B.D., and E.D. Pittman, 1982, Bimodal porosity in oolitic reservoir – effect on productivity and log response, Rodessa Limestone (Lower Cretaceous), East Texas Basin: AAPG Bulletin, v. 67, p. 1391-1399.

Krumbein, W.C., 1939, Graphic presentation and statistical analyses of sedimentary data: Recent Marine Sediments, p. 558-591.

Krumbein, W.C., and G.D. Monk, 1942, Permeability as a function of size parameters of unconsolidated sands: Petroleum Technology, AIME Technical Publication 1492, v. 5, p. 1-11.

Lindqvist, J.E., and U. Akesson, 2001, Image analysis applied to engineering geology, a literature review: Bulletin of Engineering Geology and the Environment, v. 60, p. 117-122.

Lindsay, R. F., D. L. Cantrell, G. W. Hughes, T. H. Keith, H. W. Mueller III, and S. D. Russell, 2006, Ghawar Arab-D reservoir: Widespread porosity in shoaling-upward carbonate cycles, Saudi Arabia, *in* P. M. Harris and L. J. Weber, eds., Giant hydrocarbon reservoirs of the world: From rocks to reservoir characterization and modeling: AAPG Memoir 88, p. 97-137.

Lønøy, A., 2006, Making sense of carbonate pore systems: AAPG Bulletin, v. 90, p. 1381-1405.

Lucia, F. J., 1983, Petrophysical parameters estimated from visual descriptions of carbonate rocks: A field classification of carbonate pore space: Journal of Petroleum Technology, v. 216, p. 221-224.

Lucia, F. J., 1995, Rock-fabric/petrophysical classification of carbonate pore space for reservoir characterization: AAPG Bulletin, v. 79, p. 1275–1300.

Lucia, F. J., 1999, Carbonate Reservoir Characterization: Berlin, Springer-Verlag, 226 p.

Lundegaard, P.D., 1992, Sandstone porosity loss – a “big picture” view of the importance of compaction: Journal of Sedimentary Petrology, v. 62, p. 250-260.

Ma, Y.S., X.Y. Cai, P.R. Zhao, 2011, The research status and advances in porosity evolution and diagenesis of deep carbonate reservoir (in Chinese with English abstract): Earth Science Frontiers, v. 18, p. 181-192

Melas, F.F., and G.M. Friedman, 1992, Petrophysical characteristics of the Jurassic Smackover Formation, Jay Field, Conecuh Embayment, Alabama and Florida: AAPG Bulletin, v. 76, p. 81-100.

Melim, L.A., F.S. Anselmetti, and G.P. Eberli, 2001, The importance of pore type on permeability of Neogene carbonates, Great Bahama Bank, *in* R. N. Ginsburg, ed., Subsurface geology

of a prograding carbonate platform margin, Great Bahama Bank: Results of the Bahamas Drilling Project: SEPM Special Publication 70, p. 217-238.

Merta, T., 1991, A new, universal method of thin-section – to – sieve transformation of granulometric data: Acta Geologica Polonica, v. 41, p. 117-146.

Newell, N.D., E.G. Purdy, and J. Imbrie, 1960, Bahamian oolitic sand: Journal of Geology, v. 68, p. 481-497.

Palermo, D., T. Aigner, B. Seyfang, S. Nardon, 2012, Reservoir properties and petrophysical modelling of carbonate sand bodies: outcrop analogue study in an epicontinental basin (Triassic, Germany), *in* J. Garland, J.E. Neilson, S.E. Laubach, and K.J. Whidden, eds., Advances in Carbonate Exploration and Reservoir Analysis: Geological Society of London Special Publication 370, p. 11-138

Parham, K.D., and P.G. Sutterlin, 1993, Ooid shoals of the Mississippian St. Louis Formation, Gray County, Kansas, *in* C. W. Zuppann and B. Keith, eds., Mississippian oolites and modern analogs: AAPG Studies in Geology 35, p. 185–198.

Plotnick, R.E., R.H. Gardner, and R.V. O'Neill, 1993, Lacunarity indexes as measures of landscape texture: Landscape Ecology, v. 8, p. 201-211.

Plotnick, R.E., R.H. Gardner, W. Hargrove, K. Prestegaard, and M. Perlmutter, 1996, Lacunarity analysis: A general technique for the analysis of spatial patterns: Physical Review E, v. 53, p. 461-468.

Poteet, J.E., 2007, Porosity and permeability evolution of the Raytown Limestone oolite, central Kansas: Master's thesis, University of Kansas, 200 p.

Qi, L. S., and T. R. Carr, 2005, Core description of the St. Louis Limestone, Big Bow and Sand Arroyo Creek fields, southwest Kansas: Kansas Geological Survey Open-File Report 2005-16: http://www.kgs.ku.edu/PRS/publication/2005/OFR05_16/index.html (accessed April 19, 2018).

Qiao, Z., X. Janson, A. Shen, J. Zheng, H. Zeng, X. Wang, 2016, Lithofacies, architecture, and reservoir heterogeneity of tidal-dominated platform marginal oolitic shoal: An analogue of oolitic reservoirs of Lower Triassic Feixianguan Formation, Sichuan Basin, SW China: Marine and Petroleum Geology, v. 76, p. 290-309.

Rankey, E.C., 2002, Spatial patterns of sediment accumulation on a Holocene carbonate tidal flat, northwest Andros Island, Bahamas: Journal of Sedimentary Research, v. 72, p. 591-601.

Rankey, E.C., 2014, Contrasts between wave- and tide-dominated oolitic systems: Holocene of Crooked–Acklins Platform, southern Bahamas:

Rankey, E.C., 2016, On facies belts and facies mosaics: Holocene isolated platforms, South China Sea: Sedimentology, v. 63, p. 2190-2216.

Rankey, E.C., H. Goodner, and J. Doveton, 2018, Depositional architecture and petrophysical variability of an oolitic tidal sand shoal: Pennsylvanian (Missourian), Kansas, U.S.A.: Journal of Sedimentary Research, v. 88, p. 1114–1131.

Rankey, E.C., and S. L. Reeder, 2010, Controls on platform-scale patterns of surface sediments, shallow Holocene platforms, Bahamas: Sedimentology, v. 57, p. 1545-1565.

Rankey, E.C., and S. L. Reeder, 2011, Holocene oolitic marine sand complexes of the Bahamas: Journal of Sedimentary Research, v. 81, p. 97–117.

Rankey, E.C., and S. L. Reeder, 2012, Tidal sands of the Bahamian archipelago, *in* R. A. Davis Jr. and R. W. Dalrymple, eds., Principles of tidal sedimentology: The Netherlands, Springer, p. 537–565.

Rush, J.W., and E.C. Rankey, 2017, Geostatistical facies modeling trends for oolitic tidal sand shoals: AAPG Bulletin, v. 101, p. 1341-1379.

Russ, J. C., 1998, The image processing handbook: Boca Raton, FL, CRCPress, 771 p.

Sandberg, P.A., 1983, An oscillating trend in Phanerozoic non-skeletal carbonate mineralogy: Nature, v. 305, p. 19-22.

Sigal, R., 2002, Coates and SDR permeability: Two variations on the same theme: Petrophysics, v. 43, p. 38-46.

Song, Y-Q., 2013, Magnetic resonance of porous media (MRPM): A perspective: Journal of Magnetic Resonance, v. 229, p. 12-24.

Smith, C., and L. Hamilton, 2014, Carbonate reservoir permeability from nuclear magnetic resonance logs: International Petroleum Technology Conference, IPTC-17869, 14 p.

Sparks, A.G., and E.C. Rankey, 2013, Relations between geomorphic form and sedimentologic-stratigraphic variability: Holocene ooid sand shoal, Lily Bank, Bahamas: AAPG Bulletin, v. 97, p. 61-85.

Udden, J.A., 1914, Mechanical composition of clastic sediments: GSA Bulletin, v. 25, p. 655-744.

Vincent, B., M. Fleury, Y. Santerre, and B. Brigaud, 2011, NMR relaxation of neritic carbonates: An integrated petrophysical and petrographical approach: Journal of Applied Geophysics, v. 74, p. 38-58.

Watney, W.L., and J. French, 1988, Characterization of carbonate reservoirs in the Lansing-Kansas City Groups (Upper Pennsylvanian) in Victory Field, Haskell County, Kansas, *in* S.M. Goolsby, and M.W. Longman, eds., Occurrence and petrophysical properties of carbonate reservoirs in the Rocky Mountain region: The Rocky Mountain Association of Geologists, p. 27-45.

Watney, W. L., E.K. Franseen, A.P. Byrnes, R.D. Miller, A.E. Raef, S.L. Reeder, and E.C. Rankey, 2006, Characterization of seismically imaged Pennsylvanian ooid shoal geometries and comparison with modern: AAPG Annual Convention abstract.

Weger, R.J., 2006, Quantitative pore/rock type parameters in carbonates and their relationship to velocity deviations: unpublished Ph.D. dissertation, University of Miami, 232 p.

Weger, R.J., G.P. Eberli, G.T. Baechle, J.L. Massaferro, and Y. Sun, 2009, Quantification of pore structure and its effect on sonic velocity and permeability in carbonates: AAPG Bulletin, v. 93, p. 1297-1317.

Westphal, H., I. Surholt, C. Kiesl, H.F. Thern, and T. Kruspe, 2005, NMR measurements in carbonate rocks: problems and an approach to a solution: Pure and Applied Geophysics, v. 162, p. 549-570.

Figures

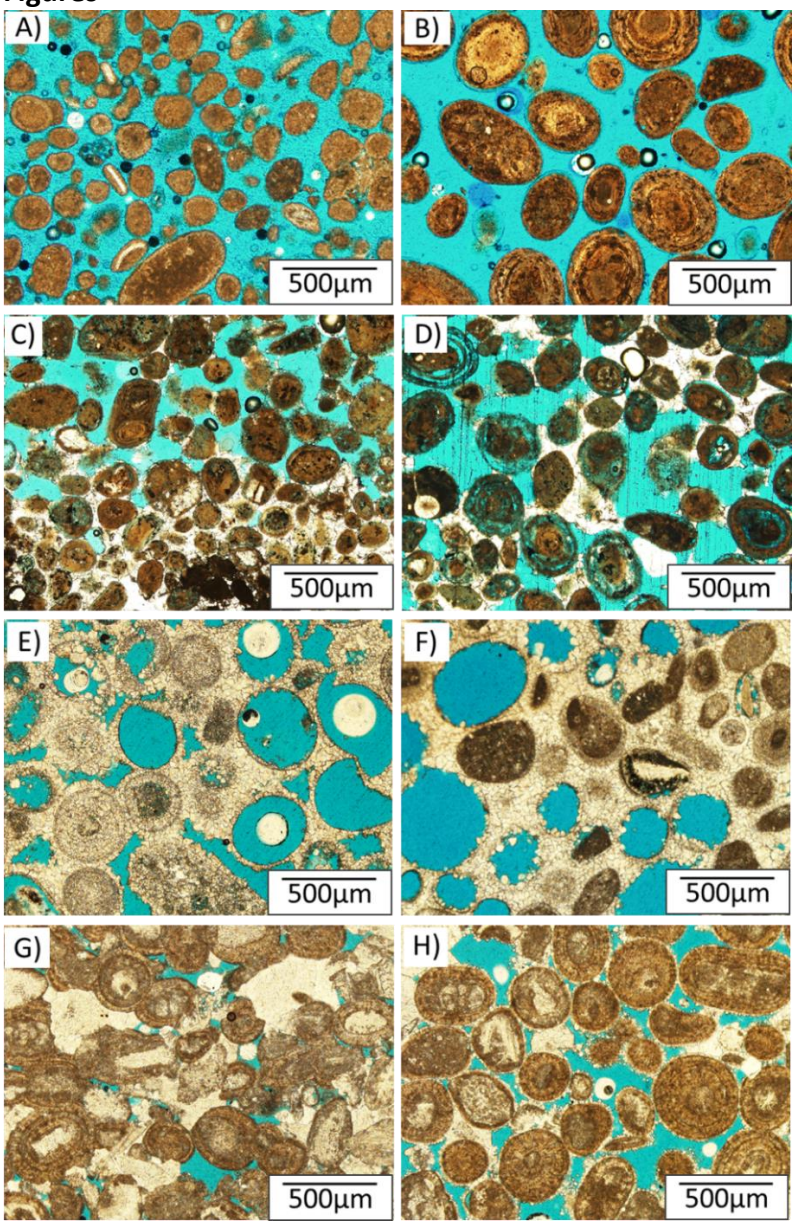

Figure 1: Thin section photomicrographs illustrating sedimentologic and diagenetic variability within and among sample groups. A) Fine, moderately sorted sand, Holocene. B) Medium, well-sorted sand, Holocene. C) Pleistocene sample showing parts of laminae. The lower, fine-grained part includes more abundant cement; in contrast, the upper part is coarser and less well cemented. D) Medium sand-sized, well-sorted Pleistocene sediment displaying partly dissolved ooids, associated moldic pores, and patchy cement. E) Medium sand-sized, very well-sorted Pennsylvanian sample including oomoldic pores, occluded oomolds, recrystallized ooids, and some preserved interparticle pores. F) Medium sand-sized, moderately sorted Pennsylvanian sediment with diverse grain types. G) Medium sand-sized, well-sorted Mississippian sediment with patchy cement and compaction indicators such as sutured grain contacts and reduced intergranular volume. H) Medium sand-sized, well-sorted Mississippian sediment with thin isopachous cement rims and few compaction features.

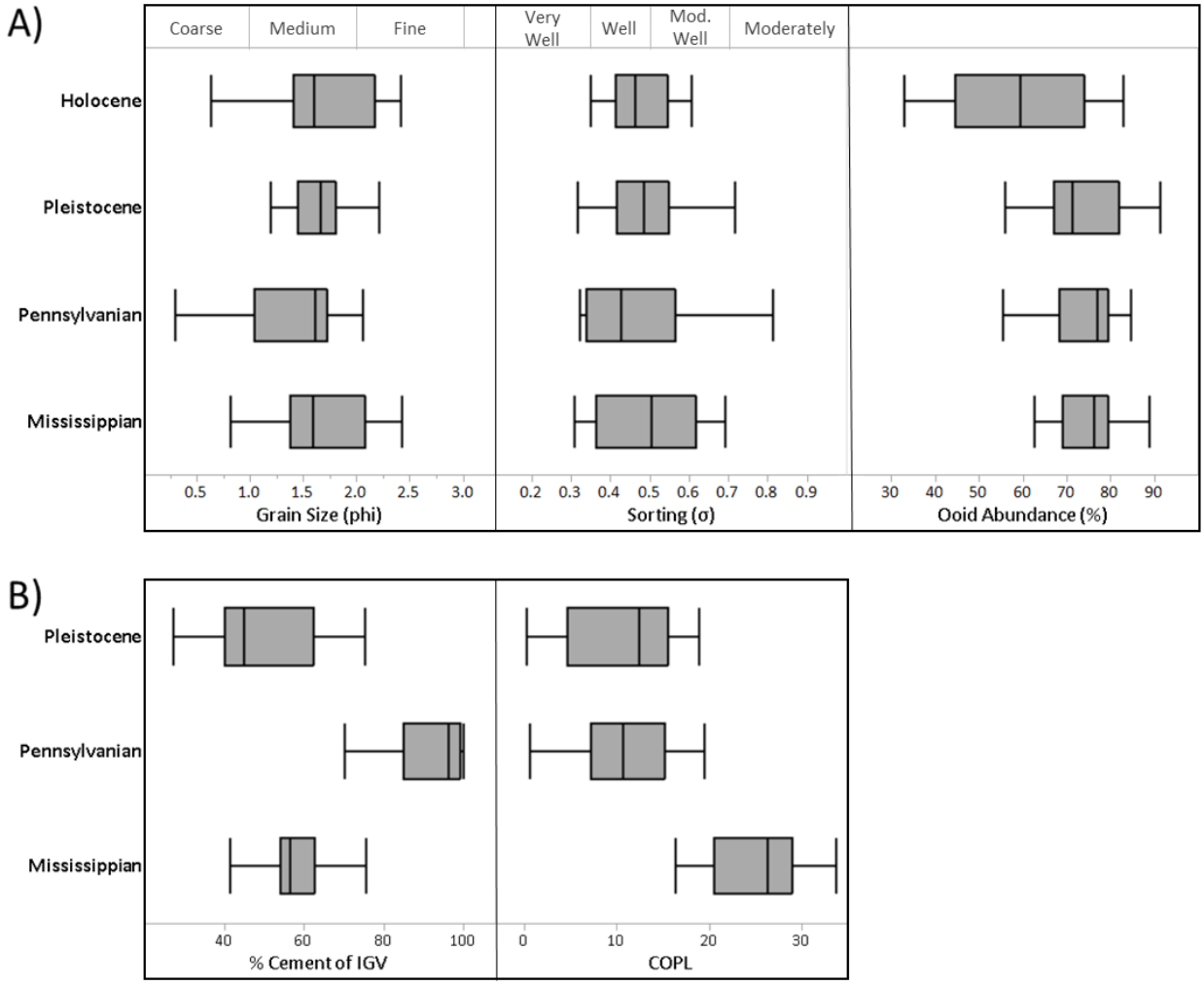

Figure 2: Quantitative metrics describing sedimentologic character and diagenetic attributes of the four sample groups. On plots, whiskers represent minimum and maximum, and boxes represent 25th, 50th, and 75th percentiles. A) Granulometry data, illustrating that samples are fine to coarse grained and moderately to very well-sorted. Ooid abundance typically is greater than 50%. B) Cementation is reported as the percentage of the intergranular volume (IGV) which is occupied by cement, whereas compaction is reported as interparticle porosity loss due to compaction (COPL; calculated as in Lundegaard, 1992). Note that Pleistocene samples have suffered relatively little cementation and compaction. Pennsylvanian rocks include highest cement abundance but low compaction, whereas Mississippian samples display moderate cement abundance and high compaction.

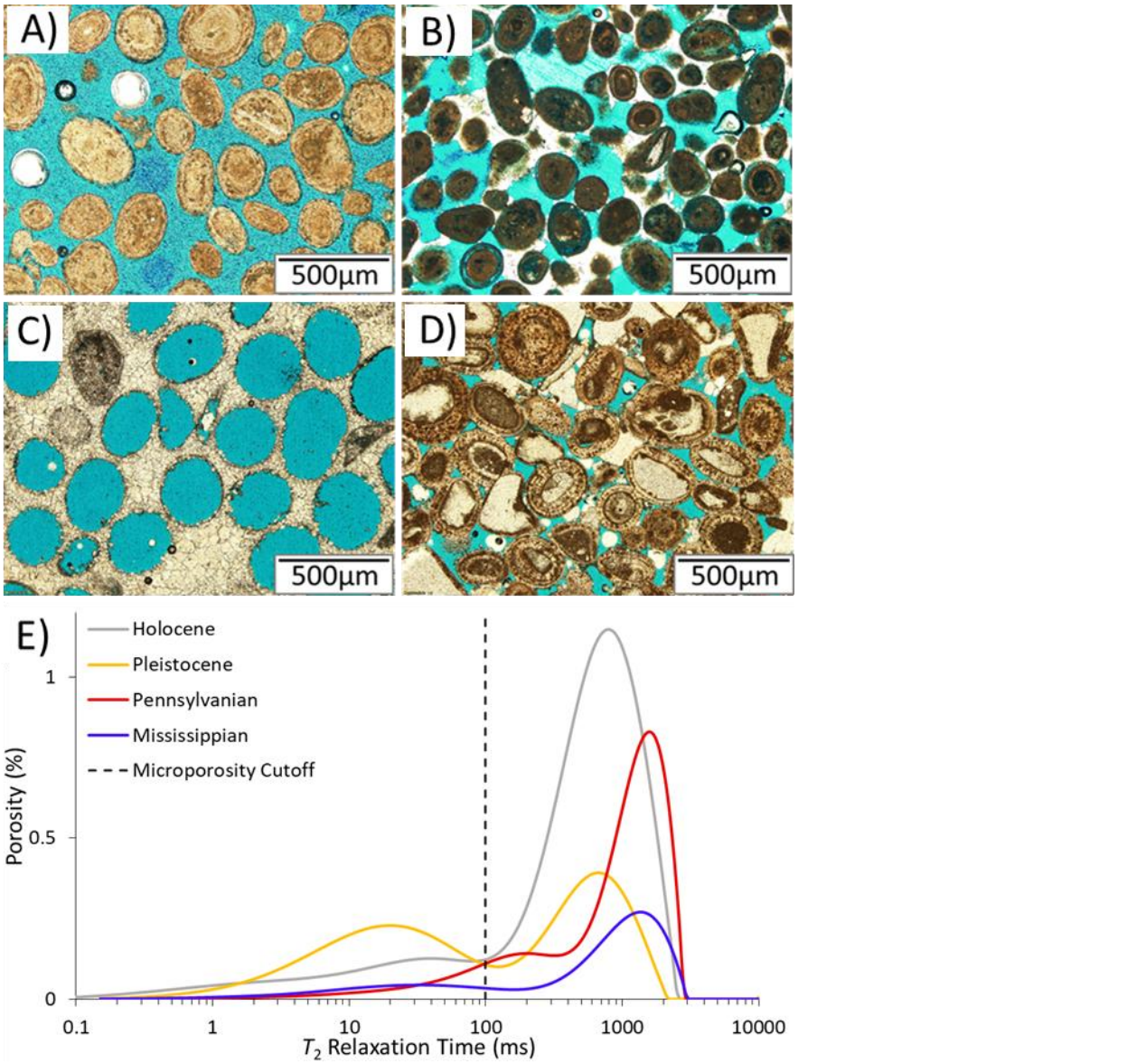

Figure 3: Thin section photomicrographs (A-D) and associated NMR T_2 relaxation curves (E) of representative, sedimentologically similar samples (well-sorted, medium sand) of each age (e.g., diagenetic scenarios). For each T_2 curve (Part E), relaxation time (a proxy for pore size) is plotted against porosity units so that the area under the curve corresponds to total porosity (%). A) Unconsolidated Holocene oolitic sand with interparticle porosity. This sample displays a high-amplitude, unimodal peak in the macroporosity domain (> 100 ms) (see Part E). B) Pleistocene grainstone. Note cementation of interparticle pores and partial dissolution of grains (bluish tint). Resultant pore-size distribution is more complex, exhibiting a bimodal distribution with a moderate amplitude macroporosity mode and clear contributions of microporosity (Part E). C) Pennsylvanian grainstone. Grains are dissolved and original interparticle pores are largely occluded with cement, leaving large isolated oomolds within a cement matrix. T_2 curve (Part E) is dominantly unimodal with high amplitude mode at relaxation times greater than 1000 ms. D) Mississippian grainstone. Note preserved ooids and interparticle pores; corresponding T_2 curve (part E) displays low amplitude modes at relaxation times greater than 1000 ms.

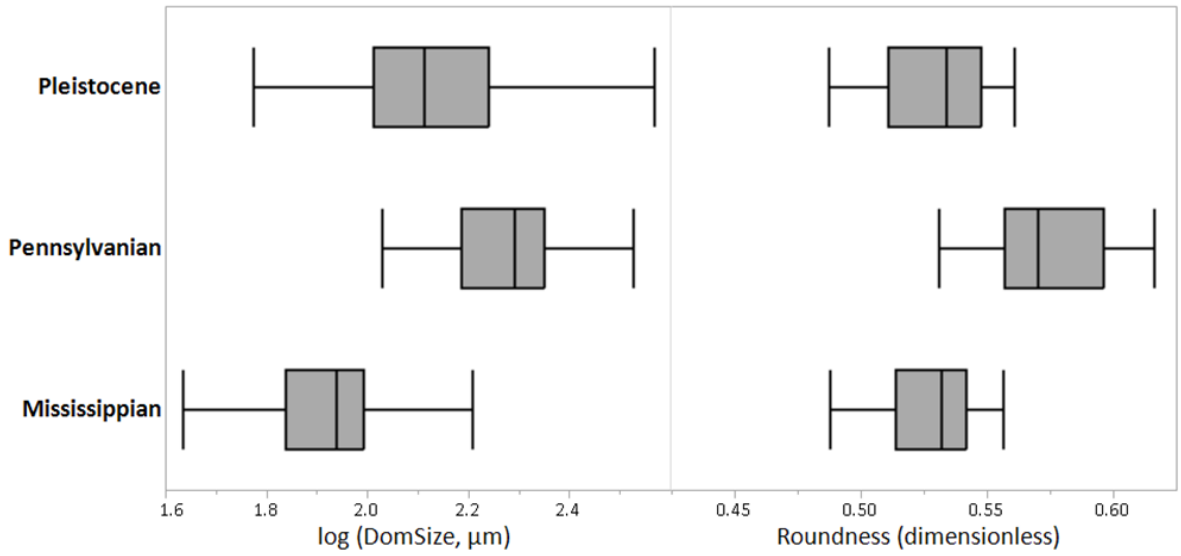

Figure 4: Digital image analysis (DIA) data illustrating differences in pore size (DomSize) and shape (Roundness) of all three lithified sample groups. On plots, whiskers represent minimum and maximum, whereas boxes represent 25th, 50th, and 75th percentiles. Data show that Pleistocene pores are of moderate size and roundness, Pennsylvanian rocks display large, rounder pores, and Mississippian samples contain relatively small and less round pores.

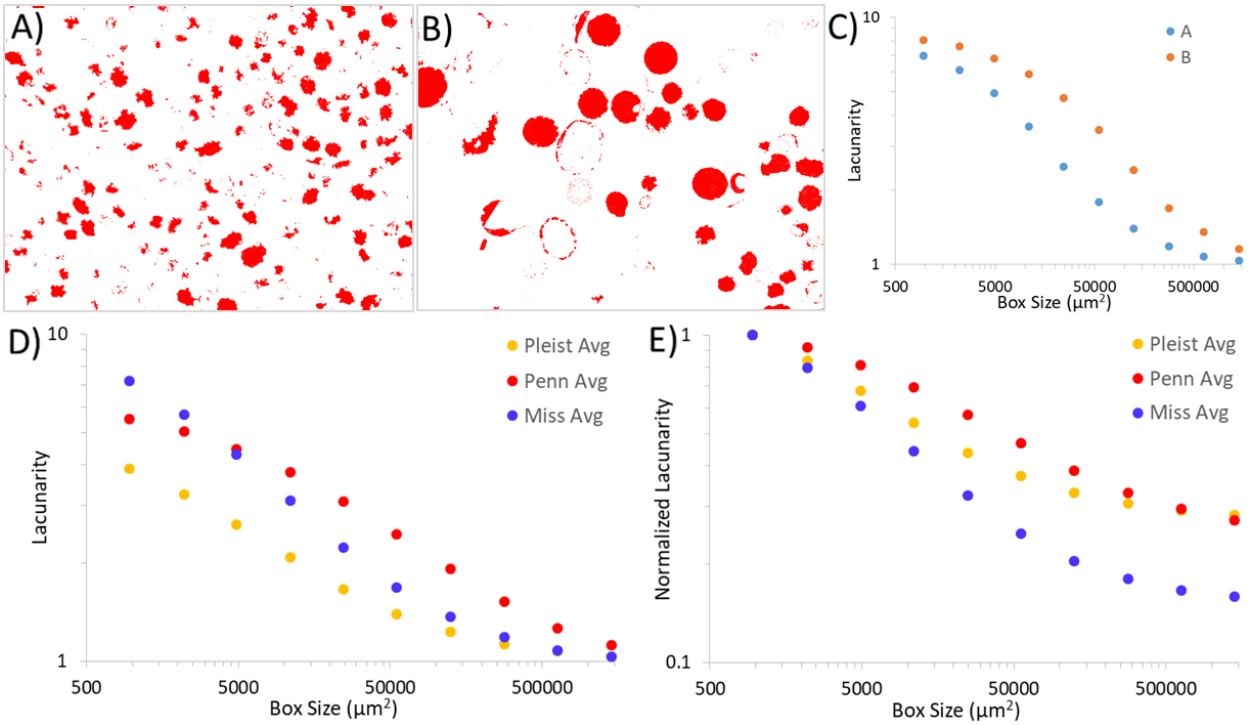

Figure 5: Plot illustrating distinct patterns of pore configuration among samples and sample groups. A-B) Binary images (red = pore) of two Pennsylvanian oomoldic samples with similar porosity (~10%, from DIA), each representing an area ~1.5 cm in width. Sample in part A includes relatively small, evenly distributed pores, whereas sample in part B includes relatively clumped, isolated pores. C) Lacunarity distributions from samples A and B. Note that sample B displays higher lacunarity at each box size, a result of the gappier pore network. Lacunarity values used for linear regressions were taken at the smallest box size. D) Average lacunarity from each sample group at each box size. E) Lacunarity distributions which have been normalized to account for varying porosity among samples, and subsequently averaged for each sample group at each box size. Data reveal pores of Pennsylvanian samples display relatively high lacunarity (i.e., isolated oomolds), whereas Mississippian samples include lowest lacunarity (i.e., evenly distributed intergranular pores). These distinctions have implications on permeability, as a gappy pore network (e.g., Pennsylvanian) yields lower k than an evenly distributed pore network (e.g., Mississippian) given similar porosity. Pleistocene samples display similar lacunarity to Mississippian examples at box sizes < 7,000 µm^2 (i.e., evenly distributed pores), but are more like Pennsylvanian examples at larger scales (i.e., gappy pore network). These results are interpreted to reflect the influence of a bimodal (micro- and macro-) pore network. At small scales, pores are widely distributed within grains (e.g., intragranular micropores) and between them (e.g., intercrystalline micropores and intergranular macropores). However, as the scale of observation is increased, increasing portions of the total porosity are recognized as clumps of intergranular macropores.

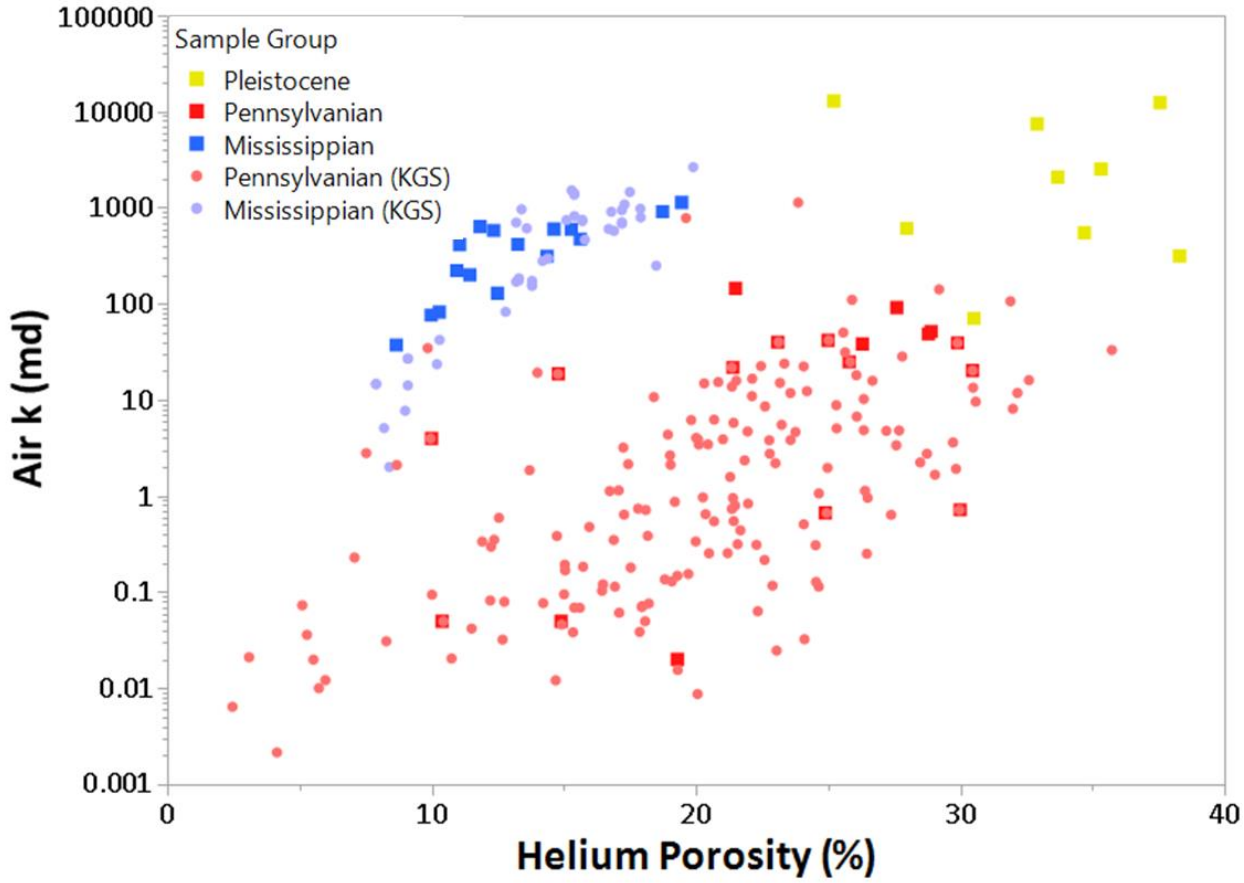

Figure 6: Porosity and permeability scatterplot, with data colored by geologic age. Samples collected as part of this study are noted by square markers, whereas unpublished data points from the Kansas Geological Survey (KGS) reservoir database are marked with lighter circles. Of the samples of this study, Pleistocene samples (n = 9) generally exhibit the highest porosity and permeability. Pennsylvanian samples (n = 15) display variable porosity and relatively low permeability. In contrast, Mississippian samples (n = 16) display lower porosity but a higher permeability for a given porosity than Pennsylvanian samples, and plot on a well-defined trend.

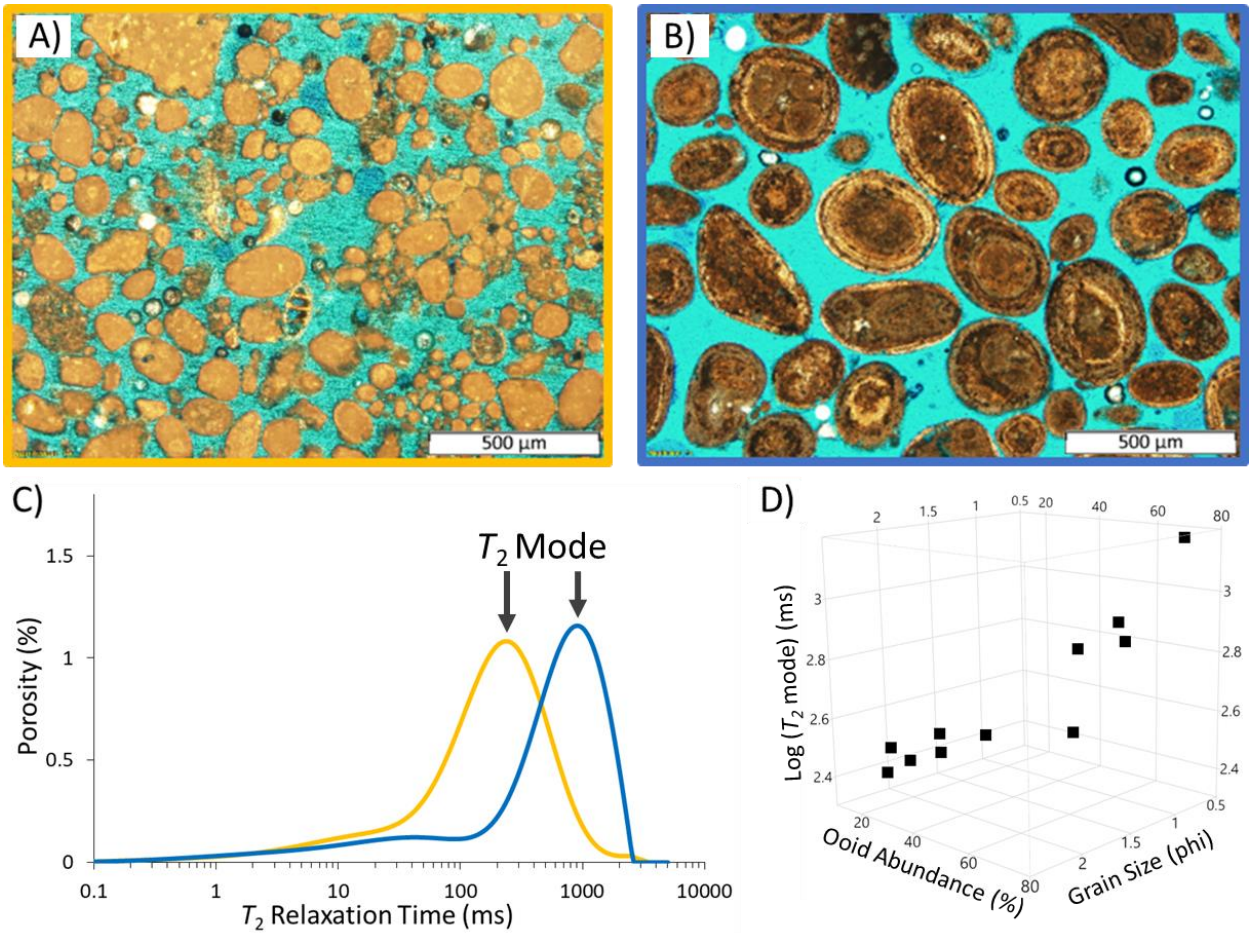

Figure 7: Relations among depositional fabric and NMR T_2 curves for Holocene sediment. A) Photomicrograph of fine-grained, moderately sorted oolitic and peloidal sediment. B) Photmicrograph of medium, well-sorted oolitic sediment. C) T_2 curves of sediment illustrated in part A (gold) and B (blue) illustrating distinct porosity, mode times, and mode porosity contributions. D) 3D scatterplot revealing relationship among grain size, ooid abundance, and modal pore size.

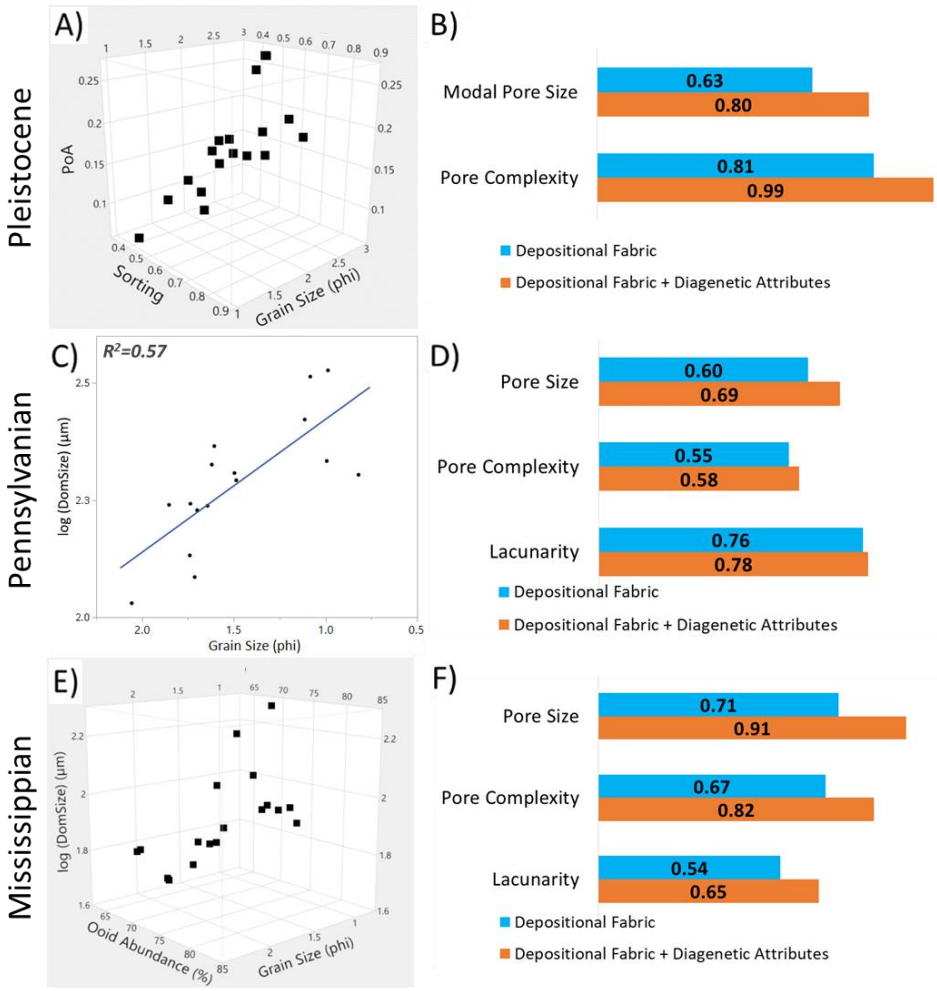

*Parameters of depositional fabric: grain size, sorting, ooid abundance, and skeletal abundance
** Diagenetic attributes: cement abundance, compaction porosity loss

Figure 8: Comparison of depositional and diagenetic attributes with pore attribute variability for the three groups. Each bar in the bar graphs (parts B, D, and F) represents an R^2 value of the correlation between rock fabric metrics (independent variable) and a single pore attribute (dependent variable); the pore attributes vary among groups, and are noted below. In this analysis, rock fabric is split into metrics of depositional (grain size, sorting, ooid abundance, skeletal abundance) and diagenetic (cement abundance, compaction porosity loss) character. Regression strength (R^2) using solely depositional fabric metrics is illustrated by the blue bars, whereas R^2 values using depositional fabric and diagenetic attributes is noted by the orange bars. A) 3D scatterplot, illustrating how grain size and sorting are inversely related to pore complexity (PoA) in Pleistocene samples. B) Correlations between metrics of Pleistocene rock fabric and modal pore size (T_2) and pore complexity. C) Cross-plot illustrating positive relationship between grain size and DomSize (plotted on log scale), Pennsylvanian samples. D) R^2 values of correlations between rock fabric and pore size (captured as log(DomSize)), pore complexity, and lacunarity, Pennsylvanian samples. E) 3D scatterplot illustrating relations among grain size, ooid content, and pore size (DomSize), Mississippian samples. F) R^2 of correlations among rock fabric and pore size (DomSize), pore complexity, and lacunarity, Mississippian samples. Collectively, these data reveal that varied depositional fabrics are associated with changes in pore attributes.

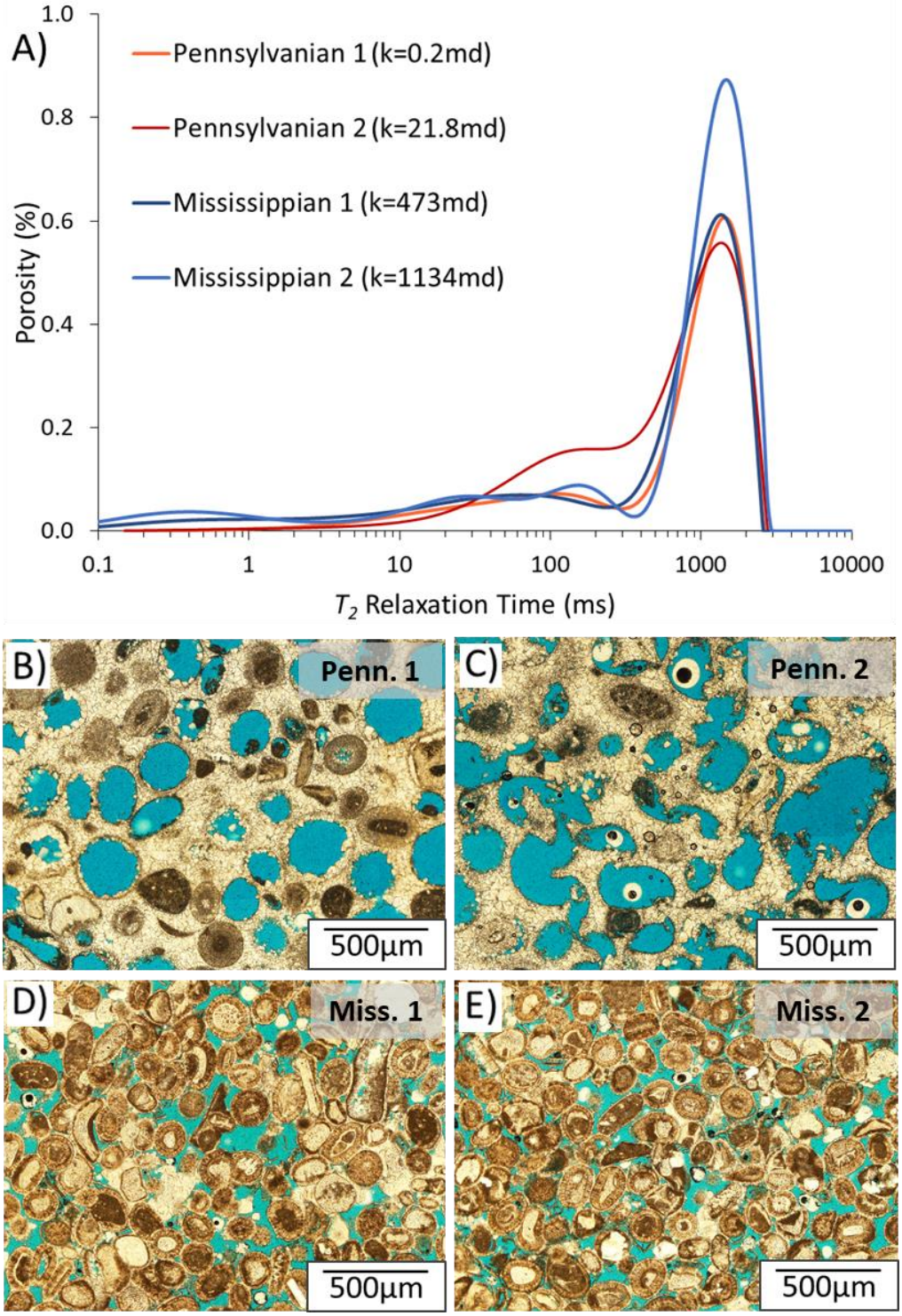

Figure 9: Relations between NMR curves and petrographic character. All samples have comparable porosity (18-20%). (A) NMR T_2 curves of illustrative samples from Pennsylvanian Lansing-Kansas City Group and Mississippian St. Louis Formation oolitic strata. B-E) Thin section photomicrographs of the samples from part A, of Pennsylvanian (B,C) and Mississippian (D,E) age. These data show that samples of very distinct pore types and connectivity can have similar NMR character.

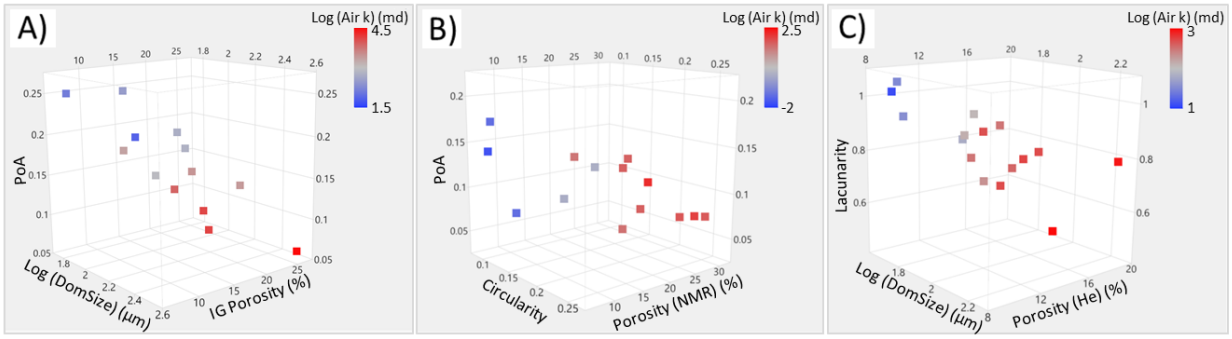

Figure 10: Three-dimensional scatterplots illustrating some relations among pore attributes (x, y, and z axes) and permeability (color scale) for each rock sample group. A) In Pleistocene samples, pore complexity, pore size, and intergranular porosity are most closely related to permeability. Multiple linear regression between these three pore attributes and permeability exhibits an R^2 of 0.90. B) In the Pennsylvanian subset, NMR porosity, pore circularity, and pore complexity estimate permeability most closely. Multiple linear regression reveals an R^2 of 0.84. C) Helium porosity, pore size, and lacunarity (at min. box size) are most closely related to permeability in Mississippian samples; multiple linear regression yields an R^2 of 0.88. Collectively, these relations suggest that the pore attributes most closely related to permeability varies among groups.

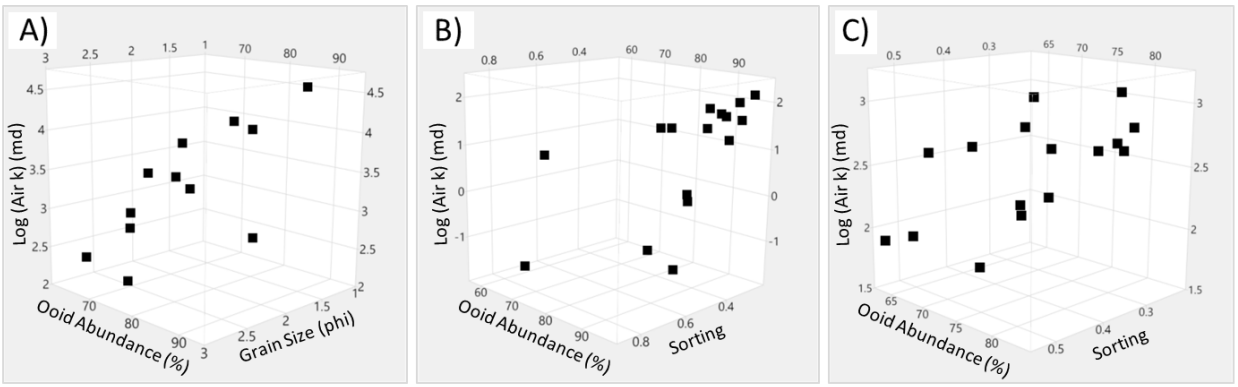

Estimators for k Prediction	R^2
Grain Size	0.49
+ Ooid Abundance	0.59
+ Sorting	0.68
+ Skeletal Abundance	0.73
+ % Cement + COPL	0.86

Estimators for k Prediction	R^2
Sorting	0.32
+ Ooid Abundance	0.43
+ Skeletal Abundance	0.48
+ Grain Size	0.50
+ % Cement + COPL	0.62

Estimators for k Prediction	R^2
Ooid Abundance	0.33
+ Skeletal Abundance	0.57
+ Sorting	0.68
+ Grain Size	0.68
+ % Cement + COPL	0.83

Figure 11: Three dimensional scatterplots and multivariate linear regression correlations illustrating relations among rock fabric metrics (independent variables) and permeability (dependent variable) among sample groups. In the tables below each plot, the metric of depositional fabric most closely correlated to permeability is listed in the top row, along with correlation coefficient between that variable and permeability. The metrics of depositional fabric (determined by stepwise regression of all possible combinations) most influential on permeability prediction are included successively in the regression, as noted by the "+ [variable]" in successive rows. A) Grain size, sorting, and ooid abundance exhibit a positive correlation with permeability in Pleistocene samples. B) Sorting and ooid abundance display a positive correlation with permeability of Pennsylvanian samples. C) Sorting and ooid abundance include a positive correlation with permeability in Mississippian samples. These data reveal that varied depositional fabrics are associated with distinct permeability, though the sedimentologic metrics most closely related to permeability changes among groups.

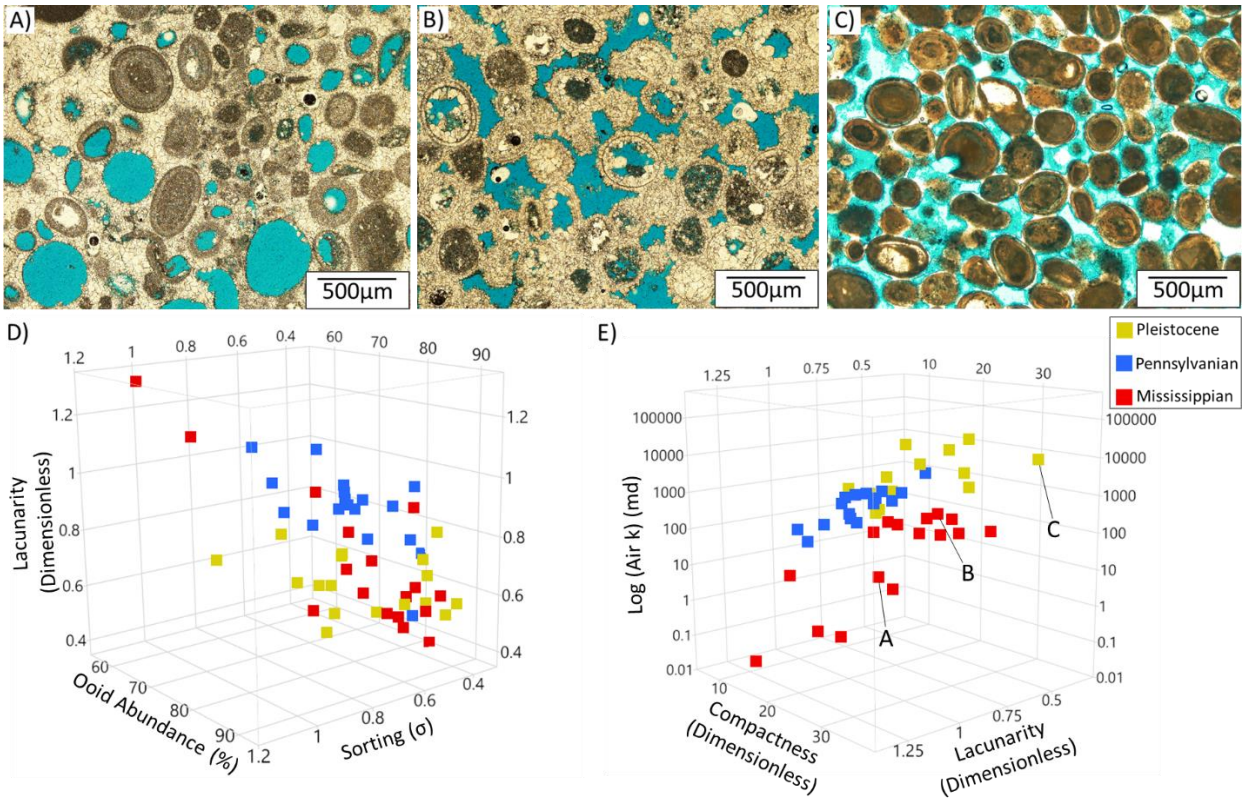

Figure 12: Illustrative thin section photomicrographs (A-C) and three dimensional scatterplots (D-E) illustrating relations among depositional fabric, pores, and Φ-k across the sample sets (age indicated by color). A) Moderately sorted Pennsylvanian sample with moderate ooid abundance includes isolated pores and low permeability (k = 0.72 mD). B) Well-sorted Pennsylvanian rock with relatively high ooid abundance contains less isolated pores and moderate permeability (k = 145 mD). C) Well-sorted Pleistocene sample with highest ooid abundance includes evenly distributed pores and exhibits highest permeability of all three samples (12.4 D). D) 3D crossplot suggesting that well-sorted sediment with high ooid abundance (%) exhibits low lacunarity (i.e., evenly distributed pore networks). E) 3D crossplot showing that sediment with low lacunarity and compact pores have high permeability. These results illustrate varied depositional fabrics are associated with distinct pore attributes, which are in turn related to changes in permeability. Collectively, these relations suggest that depositional fabric influences pore networks and petrophysical parameters across diagenetic scenarios.

Tables

Sample Group	Area or Stratigraphic Unit	Depositional Environment	Dominant Pore Type	References
Holocene	Fish Cays, Crooked-Acklins Platform, Bahamas; Schooner Cays, Great Bahama Bank, Bahamas	Ooid shoal complex	Interparticle	Ball, 1967; Rankey and Reeder, 2010, 2011, 2012; Rush and Rankey, 2017
Pleistocene	Crooked Island and Long Cay, Crooked-Acklins Platform, Bahamas	Shoreface	Interparticle and intragranular microporosity; minor moldic	Goers and Rankey, 2018, Personal Communication
Pennsylvanian	Lansing-Kansas City Grp. from Ames, Bell, Hall-Gurney, Silica, and Victory Fields (Kansas)	Mobile ooid shoal	Oomoldic; minor interparticle	Watney and French, 1988; French and Watney, 1993; Byrnes et al., 2003
Mississippian	St. Louis B from Big Bow and Sand Arroyo Creek Fields (Kansas)	Mobile ooid shoal	Interparticle	Abegg, 1991; Parham and Sutterlin, 1993; Qi and Carr, 2005

Table 1: Sedimentologic, stratigraphic, and diagenetic character of sample sets. Each group represents ooid grainstone of a distinct diagenetic scenario, ranging from un-lithified sediment (Holocene) to early diagenesis (Pleistocene) to contrasting late diagenetic end-members (Pennsylvanian, Mississippian).

Local Parameter	Definition	Description
Aspect Ratio (AR)	$\frac{Major}{Minor}$	Ratio of axis lengths of the bounding ellipse of a pore; distinguishes elongate features from star or circle shapes, but fails to distinguish stars from circles (dimensionless)
Circularity	$\frac{4\pi A}{P^2}$	Inverse of Gamma squared; sensitive to edginess or smoothness of boundaries; scale-dependent (dimensionless)
Compactness	$\mathrm{A}\sqrt{\frac{4}{\pi(Major)^2}}$	Ratio of area and length of the major ellipse axis, not sensitive to edginess (dimensionless)
Equivalent Diameter	$2\sqrt{\frac{A}{\pi}}$	Diameter of a circle with the same area as the pore; used to compare pore sizes regardless of pore shape (µm)
Gamma (γ)	$\frac{P}{2\sqrt{\pi A}}$	Ratio of pore perimeter to pore area ("unroundness"); distinguishes elongate or star shapes from circles, but fails to distinguish elongate shapes from stars (dimensionless)
Roundness	$\frac{4A}{\pi \times FD}$	Scale-independent ratio of area and Feret's Diameter; robust measure sensitive to elongate features (dimensionless)

Global Parameter	Definition	Description
Total Pore Area	$\sum A$	Sum of area of all pores (µm^2)
Total Pore Perimeter	$\sum P$	Sum of the perimeters of all pores (µm)
PoA (Perimeter over Area)	$\frac{\sum P}{\sum A}$	Describes complexity of the pore network's boundary; especially sensitive to edginess; normalized for porosity variations (1/µm)
DomSize	50th Percentile	Max pore size needed to occupy half of the pore space; given in equivalent diameter (Weger, 2006) (µm)

Table 2: Local and global DIA parameters characterizing pore size and shape, based on Russ (1998) and Weger (2006). Local parameters are calculated from the raw data produced by ImageJ, indicated by A (pore area), P (pore perimeter), Major (major axis of bounding ellipse), Minor (minor axis of bounding ellipse), and FD (Feret's Diameter: longest distance between any two points along pore boundary). In addition to these four global parameters, the mean and median of each local parameter were calculated, as well as the area-weighted average of gamma.

Rock Fabric	**Depositional Fabric**		**Diagenetic Factors**	
	Grain Size		Cement Abundance	
	Sorting		Compaction (Φ Loss)	
	Skewness		Fracture Presence (Y/N)	
	Kurtosis			
	Ooid Content (%)			
	Skeletal Content (%)			
	Composite Grain Content (%)			
	Mud Content (%)			
Pore Attributes	**Size**	**Shape**	**Spatial Distribution**	**Type**
	DomSize	PoA	Lacunarity	Intergranular Porosity
	T_2 Mode	Circularity		Moldic Porosity
	T_2 Log Mean	Compactness		
	T_2 Kurtosis	Gamma (γ)		
		Aspect Ratio (AR)		
		Roundness		
Φ - k	**Porosity**		**Permeability**	
	He Porosity (%)		Air k (md)	
	DIA Porosity (%)			
	NMR Porosity (%)			
	NMR Macroporosity (%)			
	NMR Microporosity (%)			

Table 3: Data types used throughout this study. Rock fabric includes depositional and diagenetic components and is characterized using digital petrography and point counting. Pore attributes are derived from NMR, DIA, and point counting, and quantify pore size, shape, spatial distribution, and type. These measures of rock and pore character are compared to porosity and permeability data from routine core analysis, DIA, and NMR.

Appendices

Appendix 1: *Results of Multivariate Linear Regression*

Pleistocene

Parameter of Depositional Fabric	R^2 with Φ	R^2 with k
Grain Size	**0.31**	**0.49**
Sorting	0.01	0.08
Ooid Abundance (%)	0.15	0.03
Skeletal Abundance (%)	**0.28**	0.05
% Cement of IGV	0.04	**0.61**
COPL	0.03	0.00
Pore Attribute		**R^2 with k**
DomSize		**0.38**
PoA		**0.82**
Gamma		0.18
AR		0.03
Circularity		**0.31**
Roundness		0.01
Compactness		**0.58**
Lacunarity - m		0.00
Lacunarity - Min Box Size		0.02
He Porosity		0.00
NMR Porosity		0.00
NMR Macroporosity		**0.44**
T_2 Mode		**0.43**
Intergranular Porosity		**0.59**

Pennsylvanian

Parameter of Depositional Fabric	R^2 with Φ	R^2 with k
Grain Size	0.17	0.01
Sorting	**0.62**	**0.32**
Ooid Abundance (%)	**0.63**	**0.27**
Skeletal Abundance (%)	**0.26**	0.00
% Cement of IGV	0.11	0.24
COPL	**0.42**	0.14
Pore Attribute		**R^2 with k**
DomSize		0.02
PoA		0.12
Gamma		0.02
AR		0.01
Circularity		**0.53**
Roundness		0.00
Compactness		**0.32**
Lacunarity - m		**0.59**
Lacunarity - Min Box Size		**0.50**
He Porosity		**0.33**
NMR Porosity		**0.67**
NMR Macroporosity		**0.64**
T_2 Mode		0.03
Intergranular Porosity		**0.26**

Mississippian

Parameter of Depositional Fabric	R^2 with Φ	R^2 with k
Grain Size	0.12	0.01
Sorting	**0.35**	**0.22**
Ooid Abundance (%)	0.19	**0.33**
Skeletal Abundance (%)	0.09	0.03
% Cement of IGV	0.10	**0.30**
COPL	0.04	0.00
Pore Attribute		**R^2 with k**
DomSize		**0.60**
PoA		**0.22**
Gamma		**0.33**
AR		0.03
Circularity		**0.30**
Roundness		0.04
Compactness		0.30
Lacunarity - m		**0.39**
Lacunarity - Min Box Size		**0.49**
He Porosity		**0.64**
NMR Porosity		**0.50**
NMR Macroporosity		**0.46**
T_2 Mode		**0.38**
Intergranular Porosity		0.08

Strength of correlations between individual metrics describing rocks and pores with Φ-k. Statistically significant correlations ($P \leq 0.05$) are indicated in bold.

Appendix 2: Raw Data from Holocene Samples

*Thin section photomicrographs are roughly 3.5 mm in width

BA1A-6

Grain Size (phi)	1.760
Sorting (σ)	0.684
Ooid Abundance (%)	39.645
Skeletal Abundance (%)	27.219
Intergranular Volume (%)	44.667
Cement Abundance (% of IGV)	0.000
COPL	
DomSize (µm)	
PoA (1/µm)	
Circularity (mean)	
Roundness (mean)	
Compactness (med)	
Lacunarity (Min Box Size)	
Normalized Lacunarity (Max Box Size)	
Porosity (%, NMR)	43.128
T_2LogMean (ms)	
T_2Mode Macro (ms)	349.294
Air k (md)	
Porosity (%, He)	

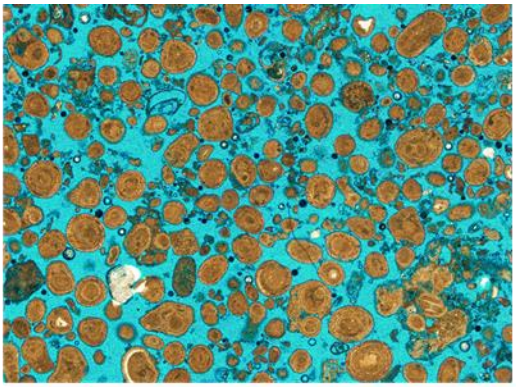

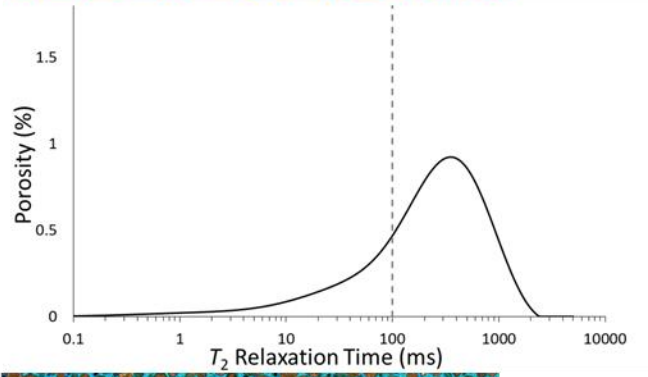

BA2-6

Grain Size (phi)	2.413
Sorting (σ)	0.673
Ooid Abundance (%)	29.586
Skeletal Abundance (%)	21.893
Intergranular Volume (%)	43.625
Cement Abundance (% of IGV)	0.000
COPL	
DomSize (µm)	
PoA (1/µm)	
Circularity (mean)	
Roundness (mean)	
Compactness (med)	
Lacunarity (Min Box Size)	
Normalized Lacunarity (Max Box Size)	
Porosity (%, NMR)	38.281
T_2LogMean (ms)	
T_2Mode Macro (ms)	349.294
Air k (md)	
Porosity (%, He)	

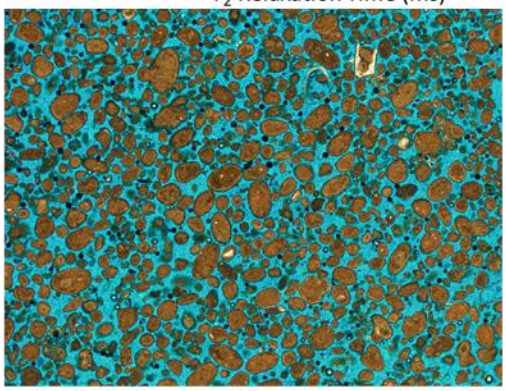

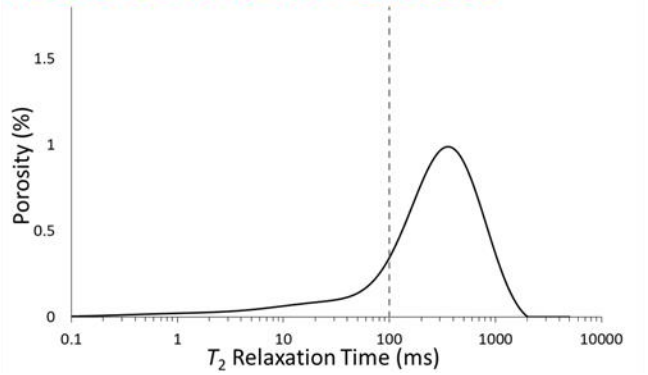

BA2-15

Grain Size (phi)	2.203
Sorting (σ)	0.545
Ooid Abundance (%)	39.475
Skeletal Abundance (%)	29.604
Intergranular Volume (%)	49.164
Cement Abundance (% of IGV)	0.000
COPL	
DomSize (µm)	
PoA (1/µm)	
Circularity (mean)	
Roundness (mean)	
Compactness (med)	
Lacunarity (Min Box Size)	
Normalized Lacunarity (Max Box Size)	
Porosity (%, NMR)	43.634
T_2LogMean (ms)	
T_2Mode Macro (ms)	392.141
Air k (md)	
Porosity (%, He)	

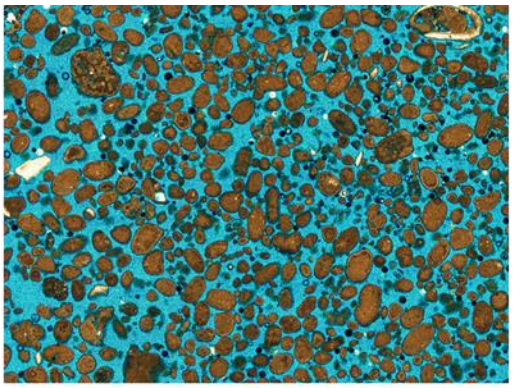

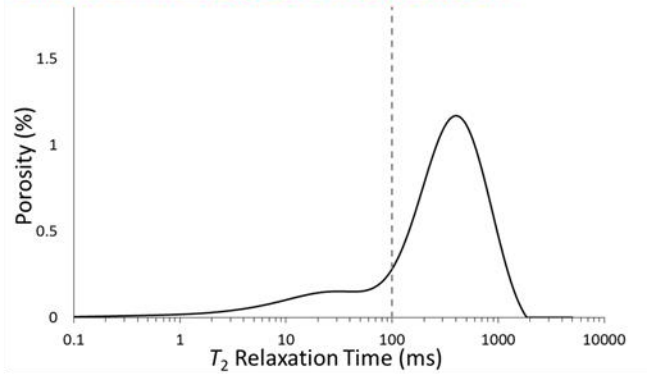

BA2-16

Grain Size (phi)	2.140
Sorting (σ)	0.590
Ooid Abundance (%)	37.158
Skeletal Abundance (%)	32.608
Intergranular Volume (%)	37.201
Cement Abundance (% of IGV)	0.000
COPL	
DomSize (µm)	
PoA (1/µm)	
Circularity (mean)	
Roundness (mean)	
Compactness (med)	
Lacunarity (Min Box Size)	
Normalized Lacunarity (Max Box Size)	
Porosity (%, NMR)	46.607
T_2LogMean (ms)	
T_2Mode Macro (ms)	329.659
Air k (md)	
Porosity (%, He)	

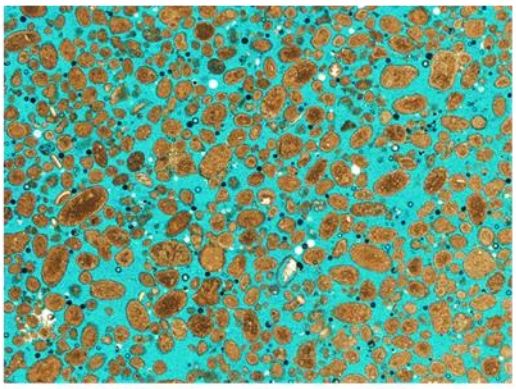

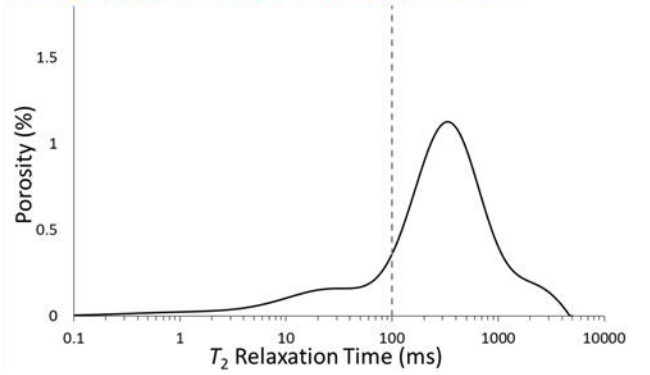

BA3-10

Grain Size (phi)	2.293
Sorting (σ)	0.480
Ooid Abundance (%)	31.677
Skeletal Abundance (%)	42.235
Intergranular Volume (%)	44.863
Cement Abundance (% of IGV)	0.000
COPL	
DomSize (µm)	
PoA (1/µm)	
Circularity (mean)	
Roundness (mean)	
Compactness (med)	
Lacunarity (Min Box Size)	
Normalized Lacunarity (Max Box Size)	
Porosity (%, NMR)	44.219
T_2LogMean (ms)	
T_2Mode Macro (ms)	311.129
Air k (md)	
Porosity (%, He)	

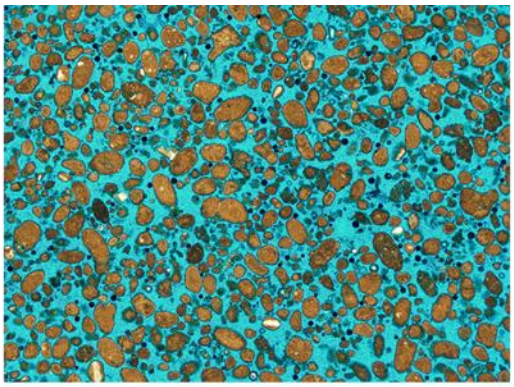

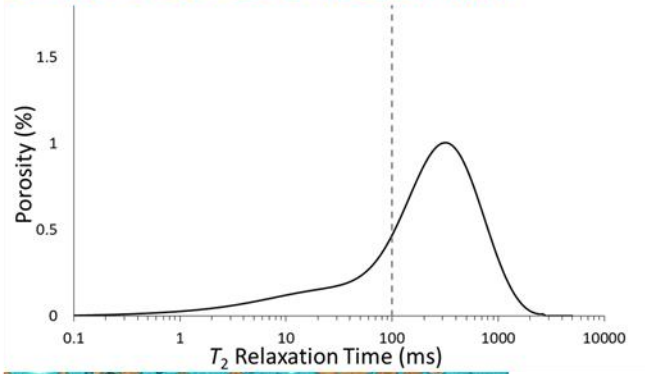

BA3-22

Grain Size (phi)	1.433
Sorting (σ)	0.634
Ooid Abundance (%)	59.333
Skeletal Abundance (%)	25.489
Intergranular Volume (%)	48.288
Cement Abundance (% of IGV)	0.000
COPL	
DomSize (µm)	
PoA (1/µm)	
Circularity (mean)	
Roundness (mean)	
Compactness (med)	
Lacunarity (Min Box Size)	
Normalized Lacunarity (Max Box Size)	
Porosity (%, NMR)	40.802
T_2LogMean (ms)	
T_2Mode Macro (ms)	370.098
Air k (md)	
Porosity (%, He)	

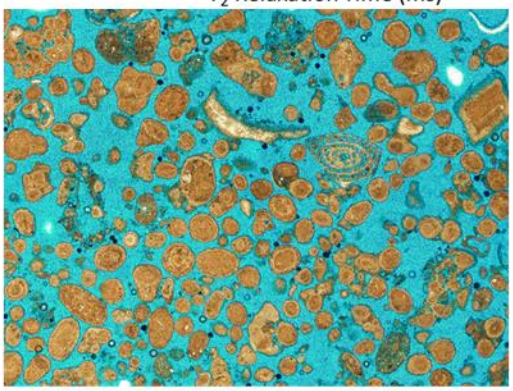

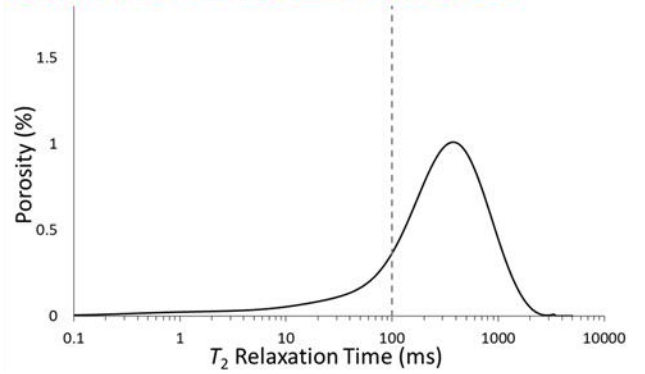

BA3-29

Grain Size (phi)	0.630
Sorting (σ)	0.490
Ooid Abundance (%)	72.132
Skeletal Abundance (%)	24.192
Intergranular Volume (%)	57.093
Cement Abundance (% of IGV)	0.000
COPL	
DomSize (µm)	
PoA (1/µm)	
Circularity (mean)	
Roundness (mean)	
Compactness (med)	
Lacunarity (Min Box Size)	
Normalized Lacunarity (Max Box Size)	
Porosity (%, NMR)	50.589
T_2LogMean (ms)	
T_2Mode Macro (ms)	1483.650
Air k (md)	
Porosity (%, He)	

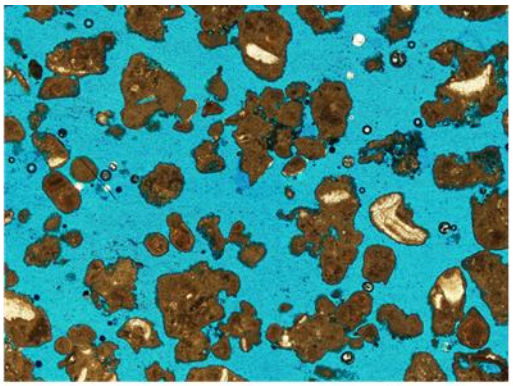

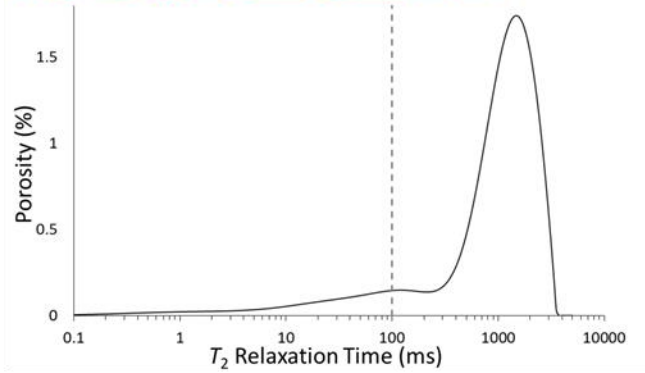

BA-7

Grain Size (phi)	2.040
Sorting (σ)	0.534
Ooid Abundance (%)	11.290
Skeletal Abundance (%)	44.624
Intergranular Volume (%)	40.068
Cement Abundance (% of IGV)	0.000
COPL	
DomSize (µm)	
PoA (1/µm)	
Circularity (mean)	
Roundness (mean)	
Compactness (med)	
Lacunarity (Min Box Size)	
Normalized Lacunarity (Max Box Size)	
Porosity (%, NMR)	46.368
T_2LogMean (ms)	
T_2Mode Macro (ms)	232.976
Air k (md)	
Porosity (%, He)	

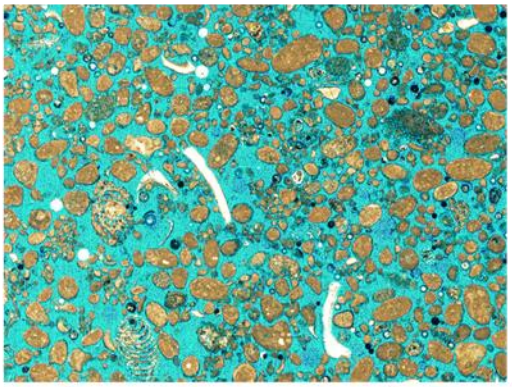

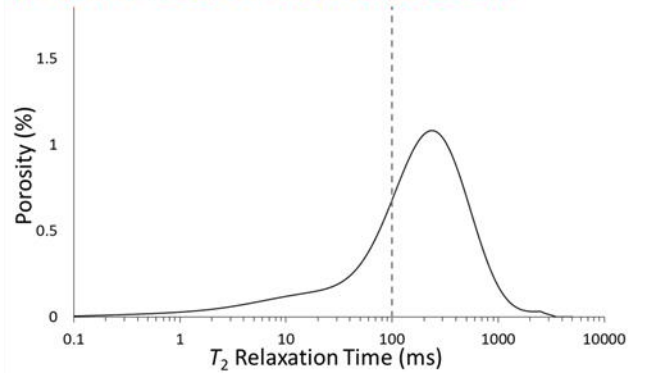

X3-21

Grain Size (phi)	1.600
Sorting (σ)	0.613
Ooid Abundance (%)	66.488
Skeletal Abundance (%)	6.486
Intergranular Volume (%)	38.127
Cement Abundance (% of IGV)	0.000
COPL	
DomSize (µm)	
PoA (1/µm)	
Circularity (mean)	
Roundness (mean)	
Compactness (med)	
Lacunarity (Min Box Size)	
Normalized Lacunarity (Max Box Size)	
Porosity (%, NMR)	41.529
T_2LogMean (ms)	
T_2Mode Macro (ms)	741.010
Air k (md)	
Porosity (%, He)	

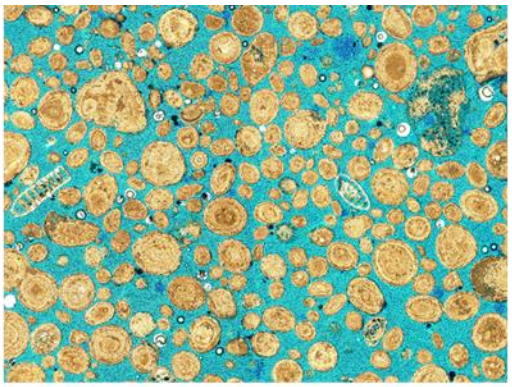

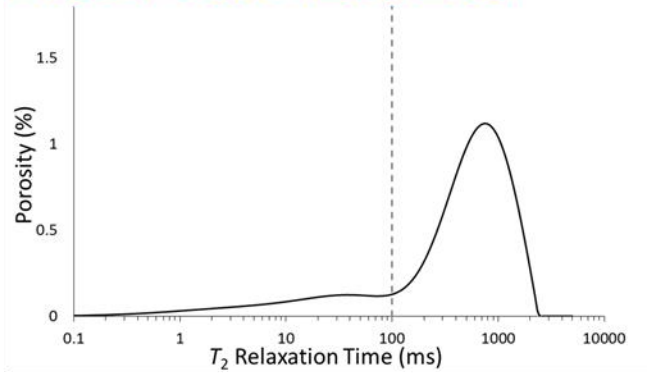

X3-25

Grain Size (phi)	1.413
Sorting (σ)	0.492
Ooid Abundance (%)	75.656
Skeletal Abundance (%)	12.501
Intergranular Volume (%)	49.159
Cement Abundance (% of IGV)	0.000
COPL	
DomSize (µm)	
PoA (1/µm)	
Circularity (mean)	
Roundness (mean)	
Compactness (med)	
Lacunarity (Min Box Size)	
Normalized Lacunarity (Max Box Size)	
Porosity (%, NMR)	42.929
T_2LogMean (ms)	
T_2Mode Macro (ms)	785.145
Air k (md)	
Porosity (%, He)	

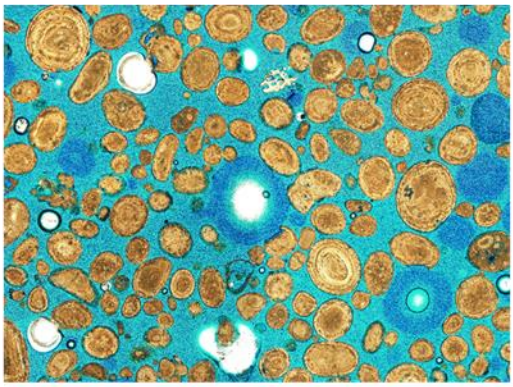

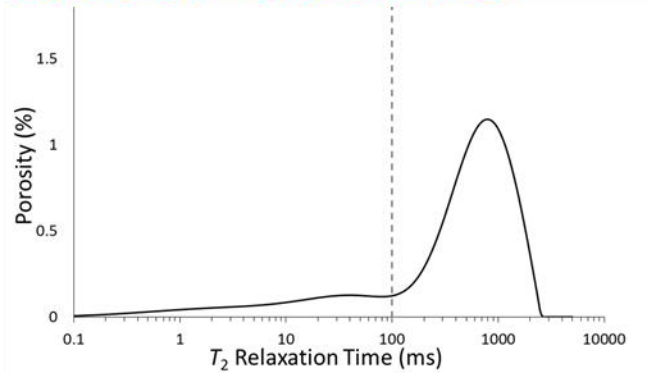

X3-28

Grain Size (phi)	1.360
Sorting (σ)	0.429
Ooid Abundance (%)	72.042
Skeletal Abundance (%)	8.065
Intergranular Volume (%)	37.374
Cement Abundance (% of IGV)	0.000
COPL	
DomSize (µm)	
PoA (1/µm)	
Circularity (mean)	
Roundness (mean)	
Compactness (med)	
Lacunarity (Min Box Size)	
Normalized Lacunarity (Max Box Size)	
Porosity (%, NMR)	41.338
T_2LogMean (ms)	
T_2Mode Macro (ms)	881.457
Air k (md)	
Porosity (%, He)	

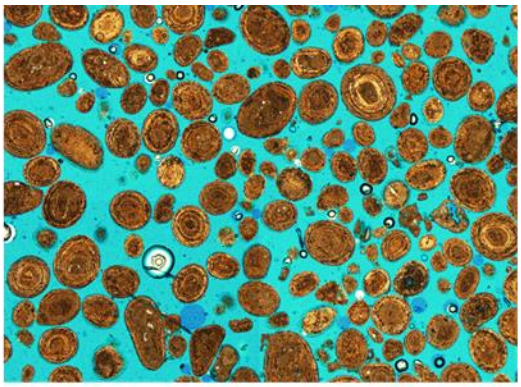

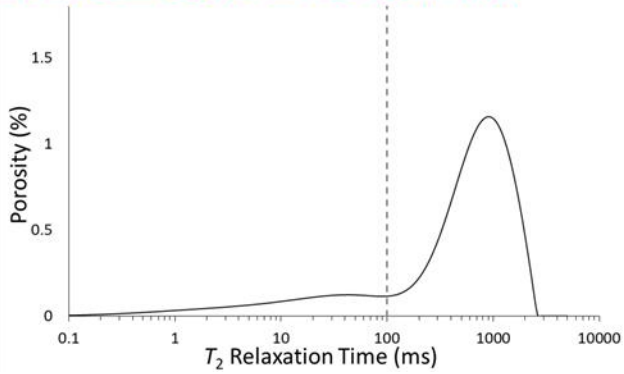

Appendix 3: Raw Data from Pleistocene Samples

*Thin section photomicrographs are roughly 3.5 mm in width

KP2-10

Grain Size (phi)	1.967
Sorting (σ)	0.716
Ooid Abundance (%)	70.588
Skeletal Abundance (%)	12.300
Intergranular Volume (%)	37.999
Cement Abundance (% of IGV)	64.036
COPL	6.691
DomSize (µm)	73.728
PoA (1/µm)	0.175
Circularity (mean)	0.244
Roundness (mean)	0.561
Compactness (med)	19.234
Lacunarity (Min Box Size)	0.772
Normalized Lacunarity (Max Box Size)	-0.748
Porosity (%, NMR)	33.690
T_2LogMean (ms)	62.498
T_2Mode Macro (ms)	548.885
Air k (md)	2090.000
Porosity (%, He)	35.039

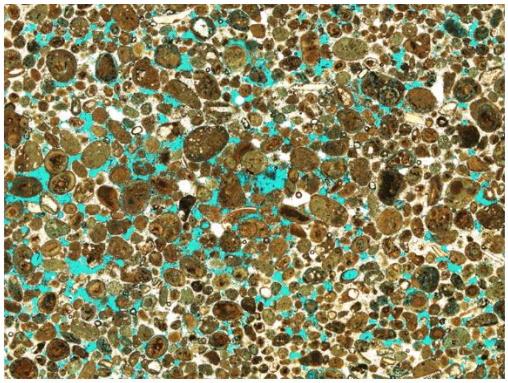

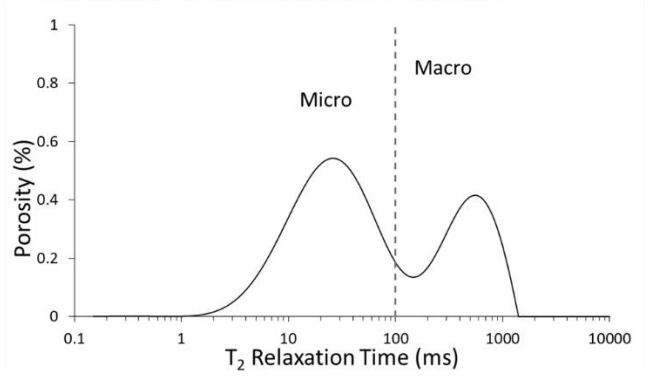

KP2-80

Grain Size (phi)	1.080
Sorting (σ)	0.401
Ooid Abundance (%)	84.996
Skeletal Abundance (%)	10.010
Intergranular Volume (%)	36.667
Cement Abundance (% of IGV)	28.181
COPL	9.138
DomSize (µm)	370.815
PoA (1/µm)	0.062
Circularity (mean)	0.174
Roundness (mean)	0.511
Compactness (med)	29.113
Lacunarity (Min Box Size)	0.639
Normalized Lacunarity (Max Box Size)	-0.588
Porosity (%, NMR)	
T_2LogMean (ms)	
T_2Mode Macro (ms)	
Air k (md)	31400.000
Porosity (%, He)	27.774

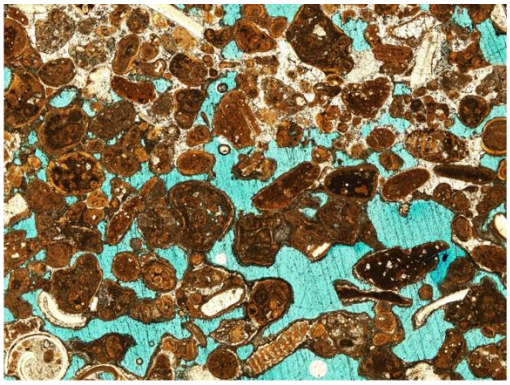

KP2-185

Grain Size (phi)	2.333
Sorting (σ)	0.525
Ooid Abundance (%)	70.855
Skeletal Abundance (%)	15.075
Intergranular Volume (%)	33.667
Cement Abundance (% of IGV)	41.584
COPL	12.356
DomSize (µm)	121.067
PoA (1/µm)	0.148
Circularity (mean)	0.174
Roundness (mean)	0.544
Compactness (med)	25.713
Lacunarity (Min Box Size)	0.548
Normalized Lacunarity (Max Box Size)	-0.534
Porosity (%, NMR)	
T_2LogMean (ms)	
T_2Mode Macro (ms)	
Air k (md)	2830.000
Porosity (%, He)	37.721

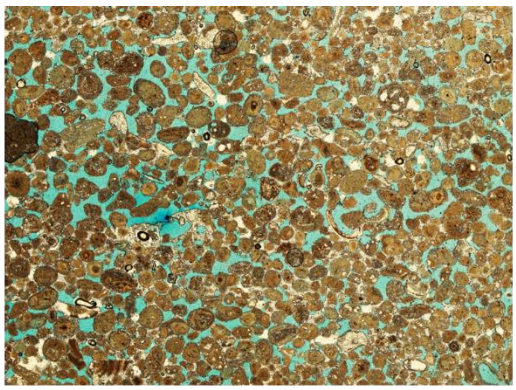

KP2-300

Grain Size (phi)	2.540
Sorting (σ)	0.538
Ooid Abundance (%)	70.527
Skeletal Abundance (%)	13.587
Intergranular Volume (%)	33.666
Cement Abundance (% of IGV)	42.574
COPL	12.357
DomSize (µm)	112.146
PoA (1/µm)	0.176
Circularity (mean)	0.171
Roundness (mean)	0.552
Compactness (med)	21.200
Lacunarity (Min Box Size)	0.371
Normalized Lacunarity (Max Box Size)	-0.367
Porosity (%, NMR)	27.980
T_2LogMean (ms)	69.069
T_2Mode Macro (ms)	548.885
Air k (md)	609.000
Porosity (%, He)	42.682

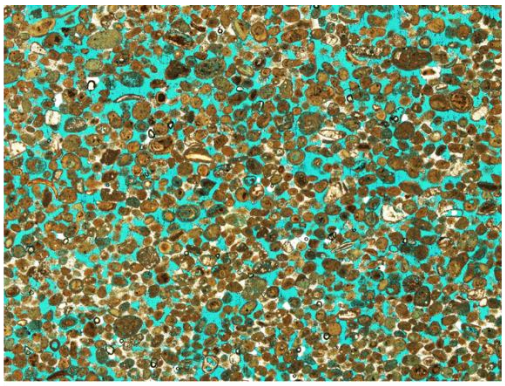

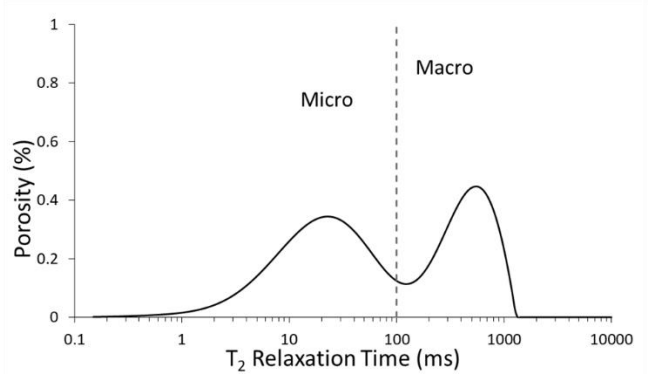

LCH9-138

Grain Size (phi)	2.193
Sorting (σ)	0.431
Ooid Abundance (%)	76.056
Skeletal Abundance (%)	13.614
Intergranular Volume (%)	28.666
Cement Abundance (% of IGV)	43.023
COPL	18.540
DomSize (µm)	129.228
PoA (1/µm)	0.132
Circularity (mean)	0.202
Roundness (mean)	0.535
Compactness (med)	20.282
Lacunarity (Min Box Size)	0.457
Normalized Lacunarity (Max Box Size)	-0.454
Porosity (%, NMR)	32.910
T_2LogMean (ms)	144.306
T_2Mode Macro (ms)	548.885
Air k (md)	7430.000
Porosity (%, He)	38.724

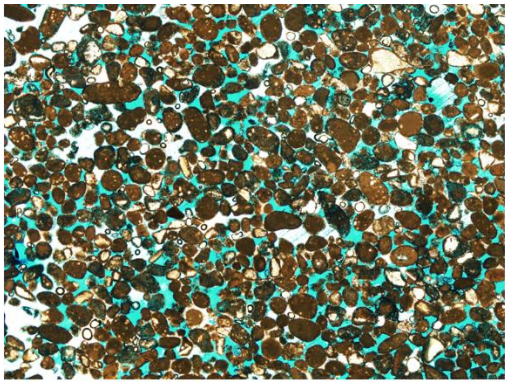

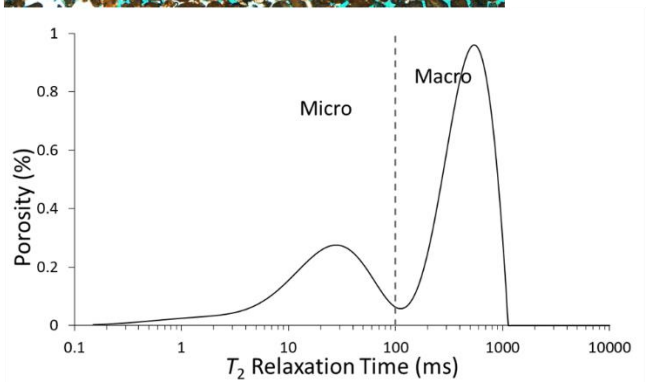

SAT2-236

Grain Size (phi)	2.410
Sorting (σ)	0.413
Ooid Abundance (%)	
Skeletal Abundance (%)	
Intergranular Volume (%)	
Cement Abundance (% of IGV)	
COPL	
DomSize (µm)	102.013
PoA (1/µm)	0.159
Circularity (mean)	0.192
Roundness (mean)	0.552
Compactness (med)	13.438
Lacunarity (Min Box Size)	0.524
Normalized Lacunarity (Max Box Size)	-0.516
Porosity (%, NMR)	34.050
T_2LogMean (ms)	70.858
T_2Mode Macro (ms)	548.885
Air k (md)	
Porosity (%, He)	34.050

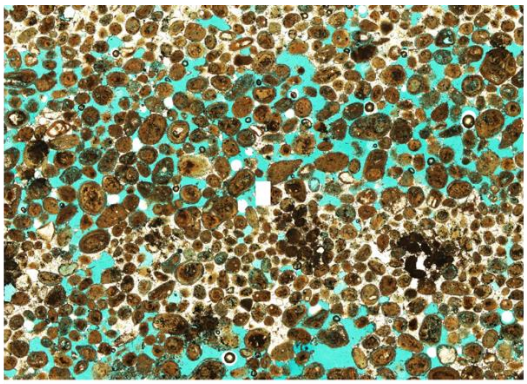

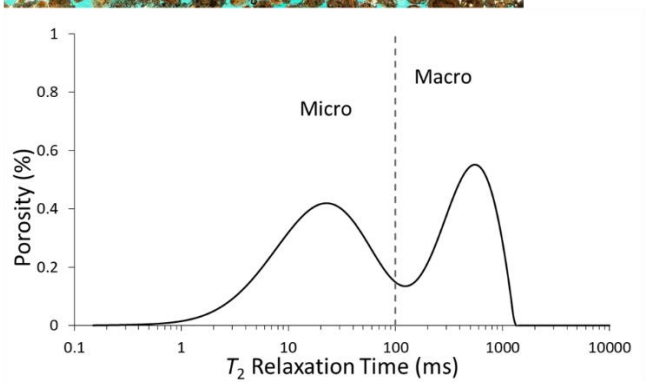

SAT2-408

Grain Size (phi)	1.950
Sorting (σ)	0.510
Ooid Abundance (%)	
Skeletal Abundance (%)	
Intergranular Volume (%)	
Cement Abundance (% of IGV)	
COPL	
DomSize (µm)	102.831
PoA (1/µm)	0.175
Circularity (mean)	0.195
Roundness (mean)	0.542
Compactness (med)	16.401
Lacunarity (Min Box Size)	0.496
Normalized Lacunarity (Max Box Size)	-0.492
Porosity (%, NMR)	36.110
T_2LogMean (ms)	28.164
T_2Mode Macro (ms)	
Air k (md)	
Porosity (%, He)	36.110

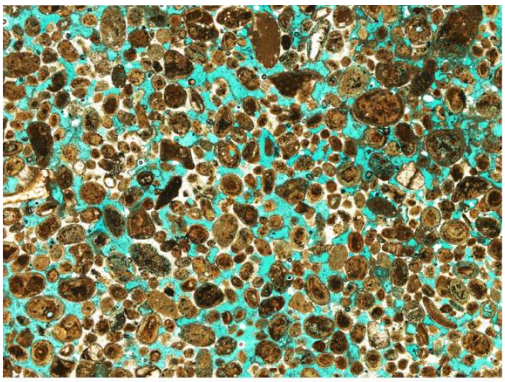

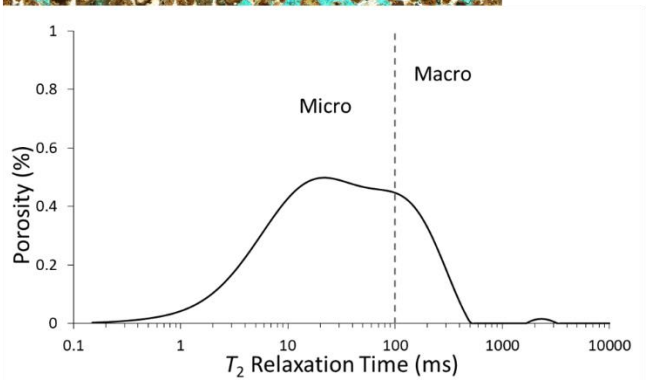

SAT3-282

Grain Size (phi)	2.157
Sorting (σ)	0.417
Ooid Abundance (%)	91.305
Skeletal Abundance (%)	4.445
Intergranular Volume (%)	39.000
Cement Abundance (% of IGV)	70.000
COPL	5.725
DomSize (µm)	127.119
PoA (1/µm)	0.204
Circularity (mean)	0.108
Roundness (mean)	0.515
Compactness (med)	10.438
Lacunarity (Min Box Size)	0.580
Normalized Lacunarity (Max Box Size)	-0.574
Porosity (%, NMR)	30.520
T_2LogMean (ms)	72.965
T_2Mode Macro (ms)	767.230
Air k (md)	70.700
Porosity (%, He)	34.013

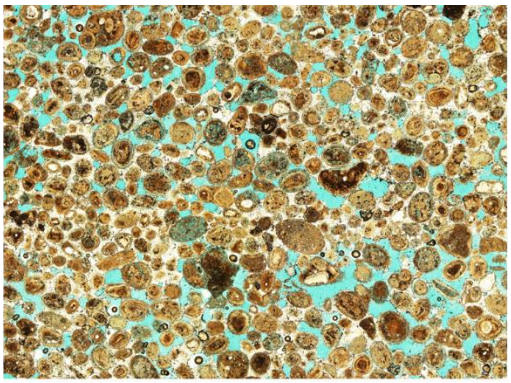

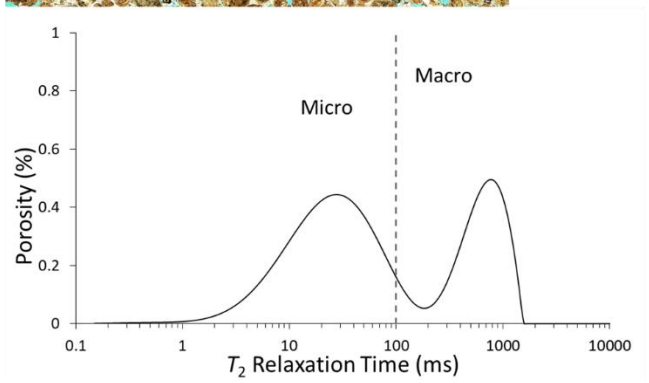

SAT3-293

Grain Size (phi)	2.210
Sorting (σ)	0.497
Ooid Abundance (%)	91.219
Skeletal Abundance (%)	4.523
Intergranular Volume (%)	31.666
Cement Abundance (% of IGV)	54.737
COPL	14.940
DomSize (µm)	117.851
PoA (1/µm)	0.151
Circularity (mean)	0.162
Roundness (mean)	0.545
Compactness (med)	14.479
Lacunarity (Min Box Size)	0.840
Normalized Lacunarity (Max Box Size)	-0.779
Porosity (%, NMR)	
T_2LogMean (ms)	
T_2Mode Macro (ms)	
Air k (md)	843.000
Porosity (%, He)	47.142

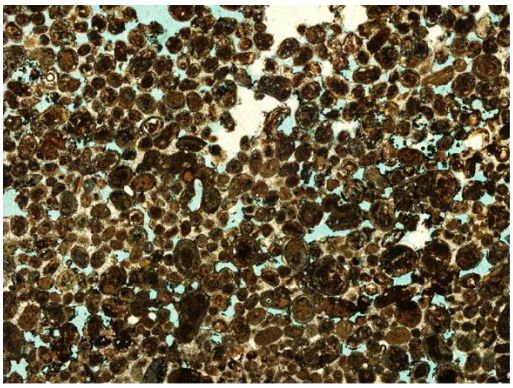

SAT4-306

Grain Size (phi)	2.363
Sorting (σ)	0.705
Ooid Abundance (%)	78.161
Skeletal Abundance (%)	5.202
Intergranular Volume (%)	41.806
Cement Abundance (% of IGV)	53.600
COPL	6.897
DomSize (µm)	158.735
PoA (1/µm)	0.208
Circularity (mean)	0.102
Roundness (mean)	0.548
Compactness (med)	12.113
Lacunarity (Min Box Size)	0.631
Normalized Lacunarity (Max Box Size)	-0.627
Porosity (%, NMR)	41.690
T_2LogMean (ms)	95.277
T_2Mode Macro (ms)	490.907
Air k (md)	
Porosity (%, He)	41.690

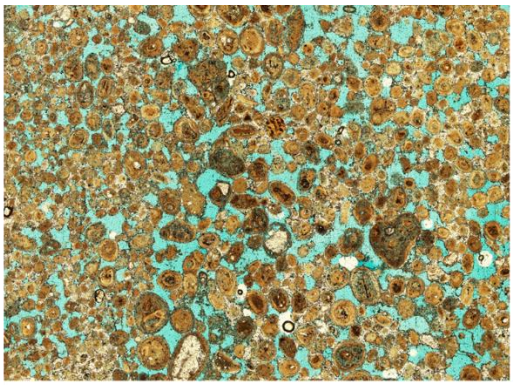

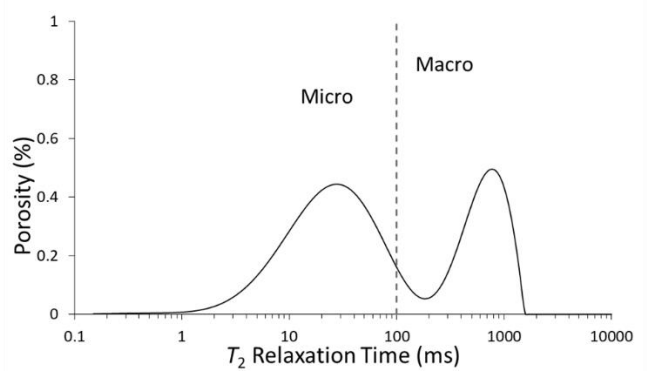

SAT4-334

Grain Size (phi)	2.387
Sorting (σ)	0.326
Ooid Abundance (%)	81.193
Skeletal Abundance (%)	7.422
Intergranular Volume (%)	33.667
Cement Abundance (% of IGV)	29.703
COPL	13.667
DomSize (µm)	200.004
PoA (1/µm)	0.136
Circularity (mean)	0.122
Roundness (mean)	0.534
Compactness (med)	16.218
Lacunarity (Min Box Size)	0.499
Normalized Lacunarity (Max Box Size)	-0.492
Porosity (%, NMR)	35.330
T_2LogMean (ms)	56.480
T_2Mode Macro (ms)	332.135
Air k (md)	2540.000
Porosity (%, He)	39.765

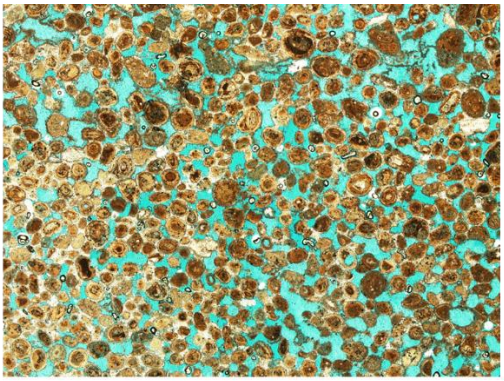

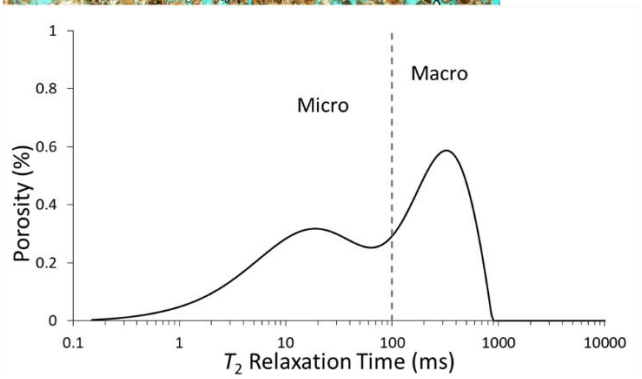

SLR7-160

Grain Size (phi)	2.110
Sorting (σ)	0.830
Ooid Abundance (%)	62.085
Skeletal Abundance (%)	22.222
Intergranular Volume (%)	30.537
Cement Abundance (% of IGV)	40.659
COPL	17.928
DomSize (µm)	131.595
PoA (1/µm)	0.202
Circularity (mean)	0.128
Roundness (mean)	0.531
Compactness (med)	16.303
Lacunarity (Min Box Size)	0.657
Normalized Lacunarity (Max Box Size)	-0.651
Porosity (%, NMR)	34.700
T_2LogMean (ms)	65.659
T_2Mode Macro (ms)	314.104
Air k (md)	549.000
Porosity (%, He)	33.946

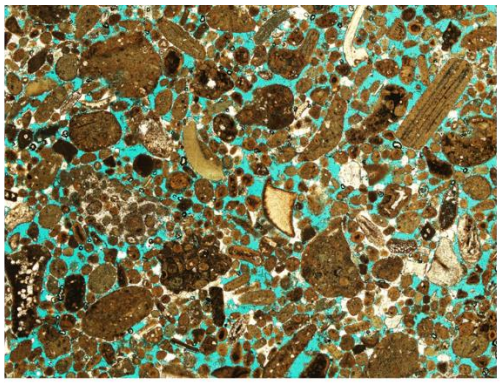

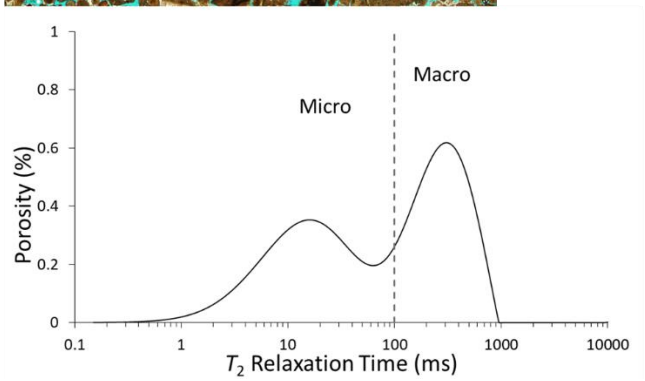

SLR8-165

Grain Size (phi)	2.953
Sorting (σ)	0.432
Ooid Abundance (%)	68.571
Skeletal Abundance (%)	12.499
Intergranular Volume (%)	29.667
Cement Abundance (% of IGV)	69.663
COPL	17.373
DomSize (µm)	135.942
PoA (1/µm)	0.261
Circularity (mean)	0.123
Roundness (mean)	0.487
Compactness (med)	11.026
Lacunarity (Min Box Size)	0.633
Normalized Lacunarity (Max Box Size)	-0.623
Porosity (%, NMR)	38.300
T_2LogMean (ms)	69.285
T_2Mode Macro (ms)	332.135
Air k (md)	315.000
Porosity (%, He)	36.331

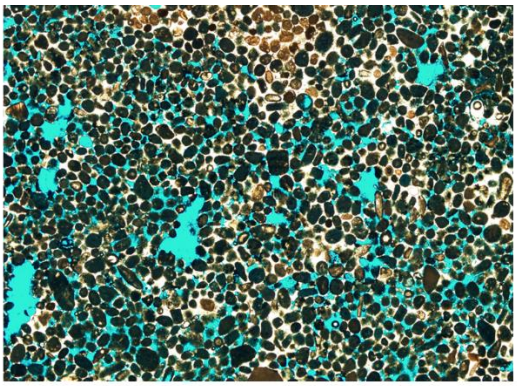

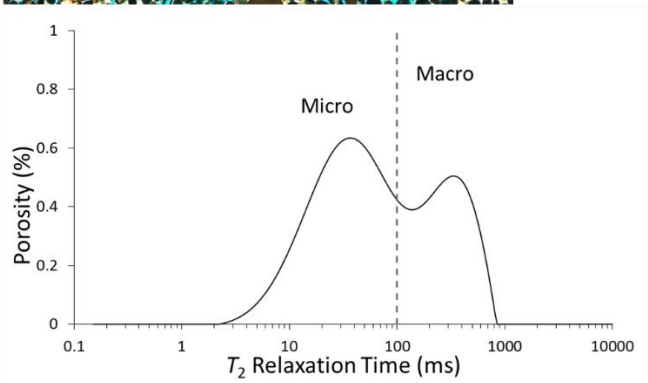

SLR8-365

Grain Size (phi)	2.600
Sorting (σ)	0.485
Ooid Abundance (%)	71.161
Skeletal Abundance (%)	15.494
Intergranular Volume (%)	28.330
Cement Abundance (% of IGV)	75.291
COPL	18.925
DomSize (µm)	59.363
PoA (1/µm)	0.250
Circularity (mean)	0.183
Roundness (mean)	0.510
Compactness (med)	13.656
Lacunarity (Min Box Size)	0.651
Normalized Lacunarity (Max Box Size)	-0.640
Porosity (%, NMR)	
T_2LogMean (ms)	
T_2Mode Macro (ms)	
Air k (md)	132.000
Porosity (%, He)	29.785

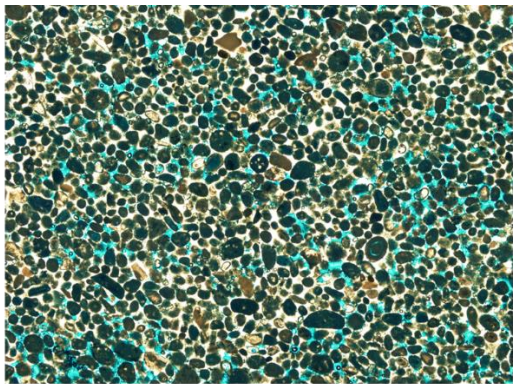

SLR9-180

Grain Size (phi)	2.898
Sorting (σ)	0.440
Ooid Abundance (%)	66.996
Skeletal Abundance (%)	9.900
Intergranular Volume (%)	32.666
Cement Abundance (% of IGV)	62.000
COPL	14.096
DomSize (µm)	64.367
PoA (1/µm)	0.262
Circularity (mean)	0.190
Roundness (mean)	0.552
Compactness (med)	15.449
Lacunarity (Min Box Size)	0.397
Normalized Lacunarity (Max Box Size)	-0.378
Porosity (%, NMR)	36.620
T_2LogMean (ms)	60.938
T_2Mode Macro (ms)	280.926
Air k (md)	
Porosity (%, He)	36.620

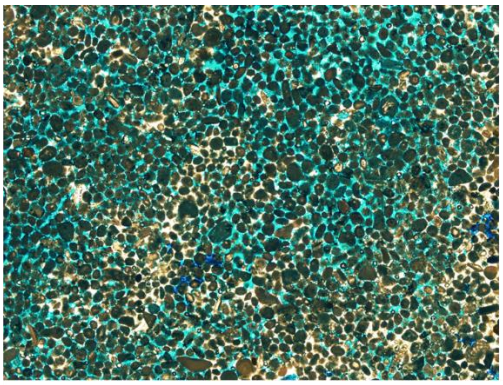

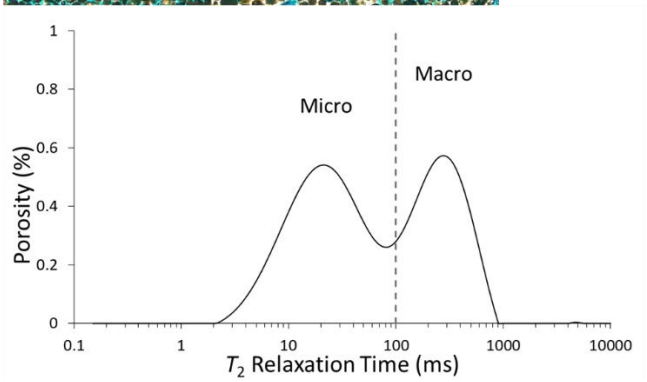

WP1-395

Grain Size (phi)	1.767
Sorting (σ)	0.317
Ooid Abundance (%)	80.098
Skeletal Abundance (%)	5.911
Intergranular Volume (%)	31.333
Cement Abundance (% of IGV)	39.361
COPL	15.355
DomSize (µm)	173.598
PoA (1/µm)	0.083
Circularity (mean)	0.222
Roundness (mean)	0.507
Compactness (med)	18.637
Lacunarity (Min Box Size)	0.651
Normalized Lacunarity (Max Box Size)	-0.645
Porosity (%, NMR)	25.220
T_2LogMean (ms)	82.873
T_2Mode Macro (ms)	686.190
Air k (md)	12900.000
Porosity (%, He)	38.937

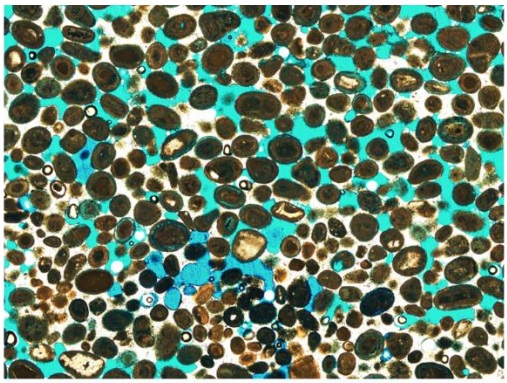

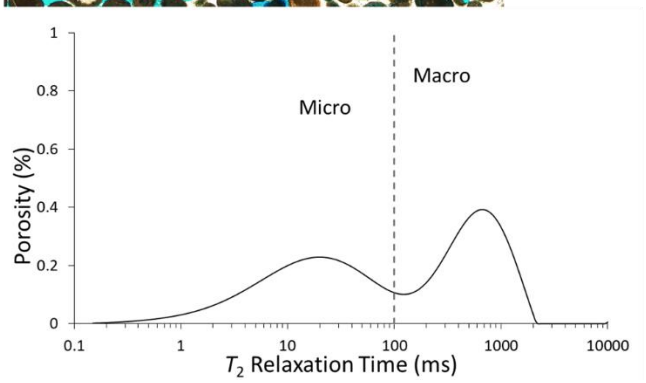

WP1-468

Grain Size (phi)	1.820
Sorting (σ)	0.392
Ooid Abundance (%)	88.136
Skeletal Abundance (%)	2.339
Intergranular Volume (%)	41.667
Cement Abundance (% of IGV)	44.800
COPL	1.377
DomSize (µm)	185.951
PoA (1/µm)	0.115
Circularity (mean)	0.210
Roundness (mean)	0.447
Compactness (med)	9.833
Lacunarity (Min Box Size)	0.514
Normalized Lacunarity (Max Box Size)	-0.510
Porosity (%, NMR)	44.720
T_2LogMean (ms)	122.900
T_2Mode Macro (ms)	686.190
Air k (md)	
Porosity (%, He)	44.720

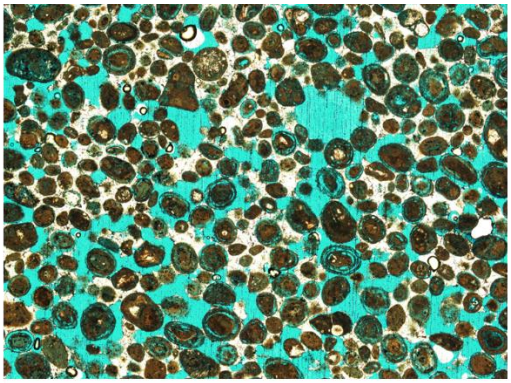

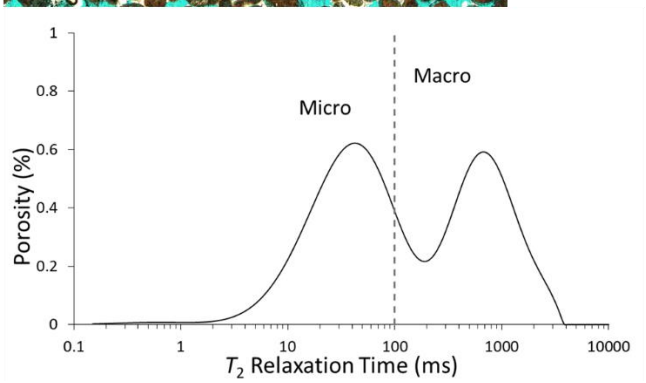

WP2-120

Grain Size (phi)	1.593
Sorting (σ)	0.557
Ooid Abundance (%)	64.945
Skeletal Abundance (%)	16.765
Intergranular Volume (%)	41.667
Cement Abundance (% of IGV)	55.200
COPL	0.240
DomSize (µm)	227.063
PoA (1/µm)	0.101
Circularity (mean)	0.200
Roundness (mean)	0.516
Compactness (med)	16.760
Lacunarity (Min Box Size)	0.529
Normalized Lacunarity (Max Box Size)	-0.514
Porosity (%, NMR)	30.490
T_2LogMean (ms)	124.452
T_2Mode Macro (ms)	811.272
Air k (md)	
Porosity (%, He)	30.490

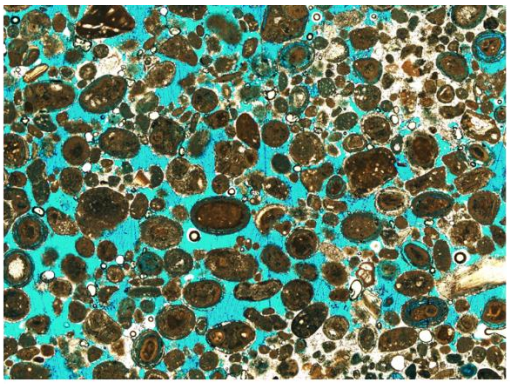

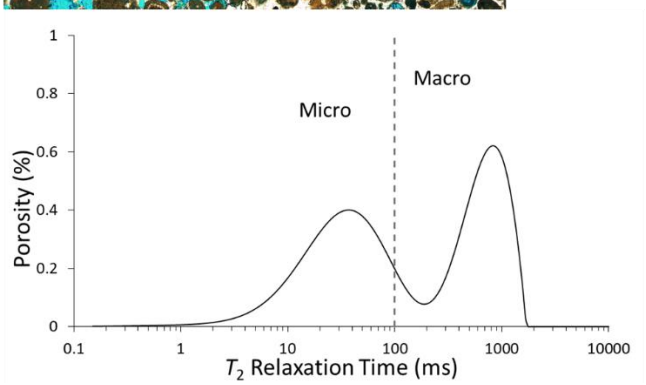

WPB-280

Grain Size (phi)	1.897
Sorting (σ)	0.434
Ooid Abundance (%)	82.039
Skeletal Abundance (%)	3.901
Intergranular Volume (%)	31.334
Cement Abundance (% of IGV)	37.234
COPL	15.354
DomSize (µm)	147.016
PoA (1/µm)	0.102
Circularity (mean)	0.198
Roundness (mean)	0.531
Compactness (med)	36.816
Lacunarity (Min Box Size)	0.525
Normalized Lacunarity (Max Box Size)	-0.522
Porosity (%, NMR)	37.560
T_2LogMean (ms)	83.991
T_2Mode Macro (ms)	519.087
Air k (md)	12400.000
Porosity (%, He)	38.943

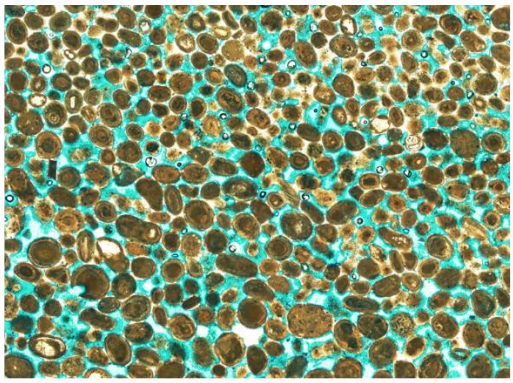

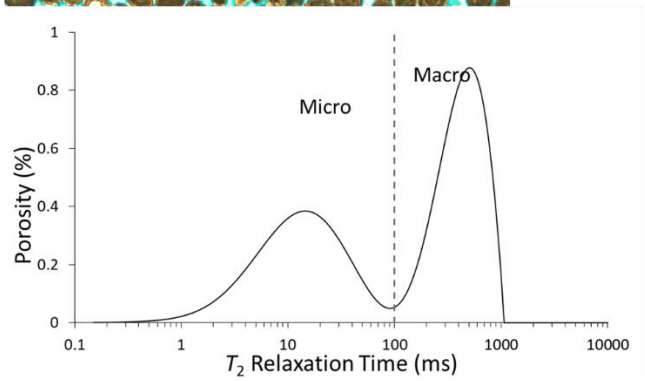

Appendix 4: Raw Data from Pennsylvanian Samples

*Thin section photomicrographs are roughly 3.5 mm in width

Penn 1

Grain Size (phi)	1.713
Sorting (σ)	0.261
Ooid Abundance (%)	97.108
Skeletal Abundance (%)	1.391
Intergranular Volume (%)	38.611
Cement Abundance (% of IGV)	77.419
COPL	9.855
DomSize (µm)	121.839
PoA (1/µm)	0.115
Circularity (mean)	0.223
Roundness (mean)	0.592
Compactness (med)	21.097
Lacunarity (Min Box Size)	0.547
Normalized Lacunarity (Max Box Size)	-0.541
Porosity (%, NMR)	22.210
T_2LogMean (ms)	442.282
T_2Mode Macro (ms)	1199.090
Air k (md)	145.500
Porosity (%, He)	21.500

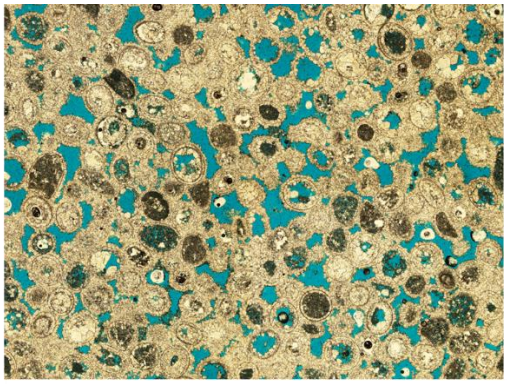

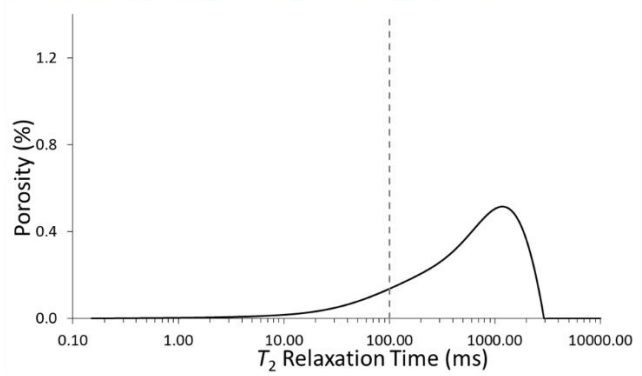

Penn 3

Grain Size (phi)	1.643
Sorting (σ)	0.282
Ooid Abundance (%)	90.012
Skeletal Abundance (%)	0.000
Intergranular Volume (%)	41.000
Cement Abundance (% of IGV)	79.545
COPL	6.892
DomSize (µm)	172.925
PoA (1/µm)	0.074
Circularity (mean)	0.253
Roundness (mean)	0.559
Compactness (med)	23.846
Lacunarity (Min Box Size)	0.517
Normalized Lacunarity (Max Box Size)	-0.485
Porosity (%, NMR)	29.960
T_2LogMean (ms)	767.236
T_2Mode Macro (ms)	1874.030
Air k (md)	48.600
Porosity (%, He)	28.800

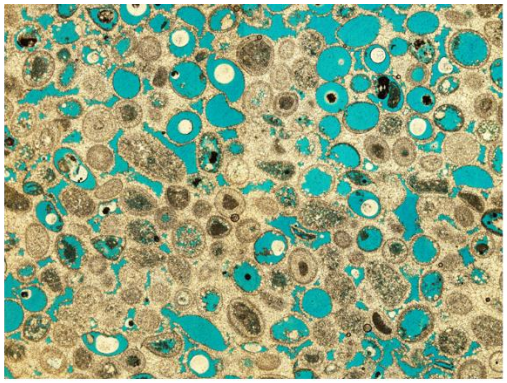

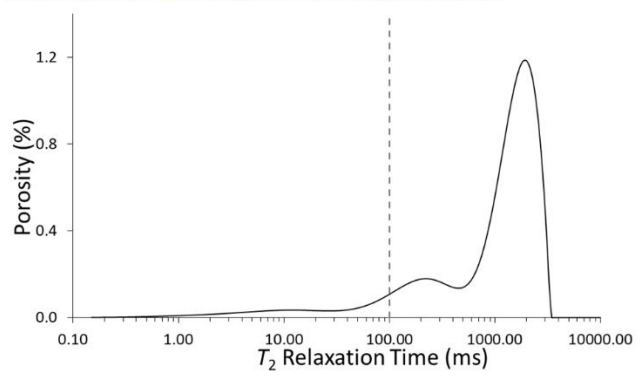

Penn 4

Grain Size (phi)	1.700
Sorting (σ)	0.261
Ooid Abundance (%)	93.531
Skeletal Abundance (%)	0.000
Intergranular Volume (%)	39.761
Cement Abundance (% of IGV)	85.826
COPL	8.453
DomSize (µm)	169.188
PoA (1/µm)	0.071
Circularity (mean)	0.239
Roundness (mean)	0.600
Compactness (med)	21.321
Lacunarity (Min Box Size)	0.475
Normalized Lacunarity (Max Box Size)	-0.465
Porosity (%, NMR)	29.800
T_2LogMean (ms)	876.684
T_2Mode Macro (ms)	2215.640
Air k (md)	91.800
Porosity (%, He)	27.600

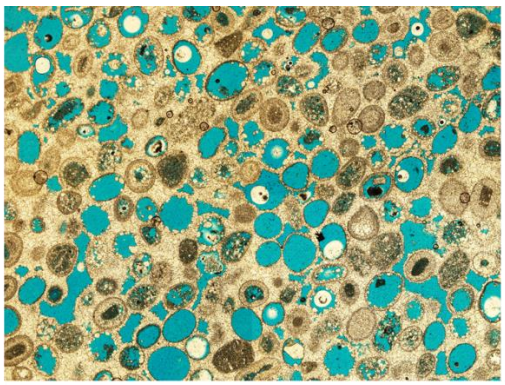

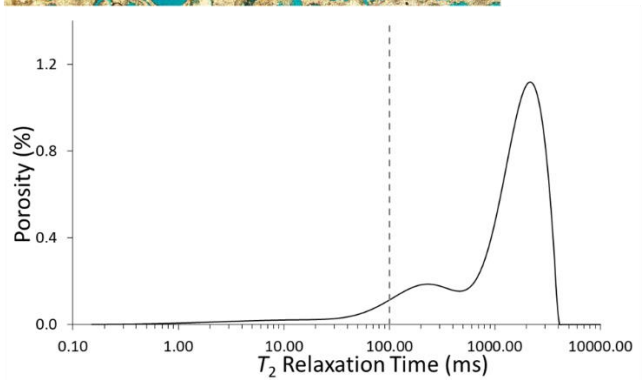

Penn 12

Grain Size (phi)	1.737
Sorting (σ)	0.248
Ooid Abundance (%)	85.341
Skeletal Abundance (%)	0.000
Intergranular Volume (%)	33.455
Cement Abundance (% of IGV)	97.249
COPL	15.997
DomSize (µm)	174.644
PoA (1/µm)	0.068
Circularity (mean)	0.225
Roundness (mean)	0.602
Compactness (med)	26.176
Lacunarity (Min Box Size)	0.408
Normalized Lacunarity (Max Box Size)	-0.399
Porosity (%, NMR)	28.650
T_2LogMean (ms)	771.826
T_2Mode Macro (ms)	1585.090
Air k (md)	51.600
Porosity (%, He)	28.900

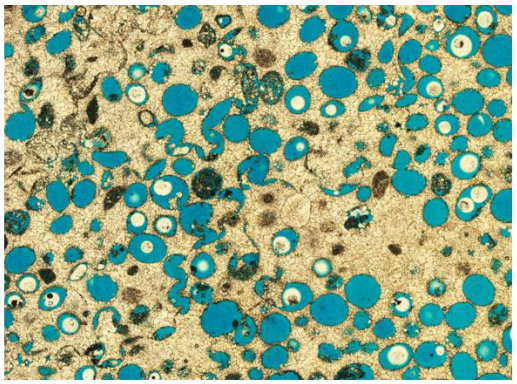

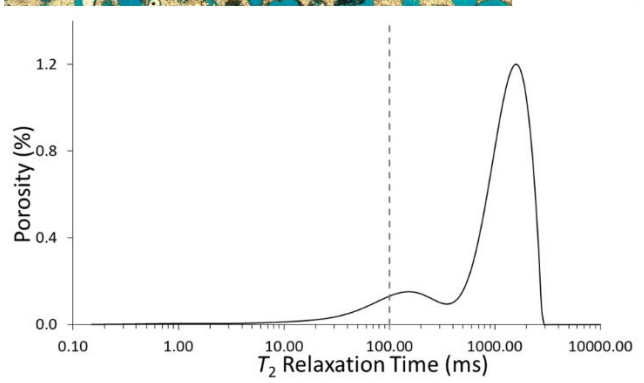

Penn 14

Grain Size (phi)	0.993
Sorting (σ)	0.563
Ooid Abundance (%)	89.284
Skeletal Abundance (%)	10.690
Intergranular Volume (%)	39.905
Cement Abundance (% of IGV)	81.890
COPL	8.274
DomSize (µm)	215.500
PoA (1/µm)	0.090
Circularity (mean)	0.230
Roundness (mean)	0.531
Compactness (med)	13.696
Lacunarity (Min Box Size)	0.550
Normalized Lacunarity (Max Box Size)	-0.538
Porosity (%, NMR)	20.000
T_2LogMean (ms)	317.270
T_2Mode Macro (ms)	857.841
Air k (md)	40.020
Porosity (%, He)	23.100

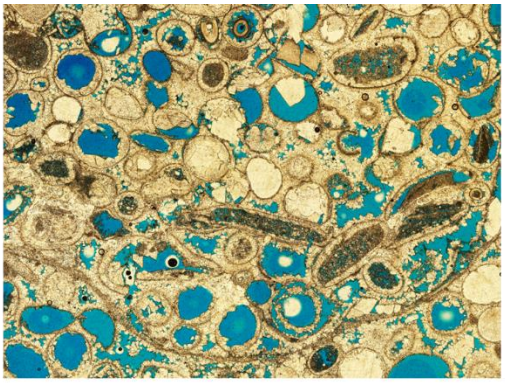

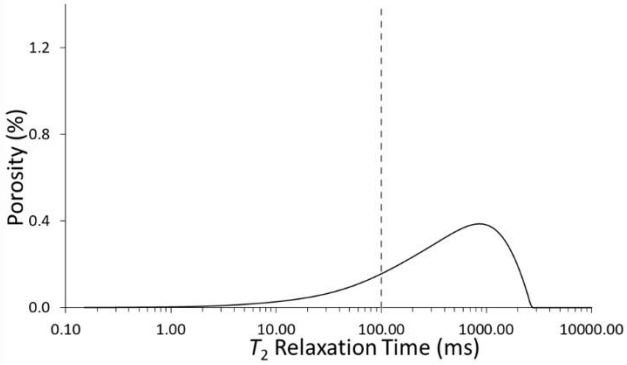

Penn 20A

Grain Size (phi)	1.740
Sorting (σ)	0.255
Ooid Abundance (%)	94.013
Skeletal Abundance (%)	0.000
Intergranular Volume (%)	38.000
Cement Abundance (% of IGV)	95.193
COPL	15.709
DomSize (µm)	135.526
PoA (1/µm)	0.133
Circularity (mean)	0.186
Roundness (mean)	0.569
Compactness (med)	13.009
Lacunarity (Min Box Size)	0.360
Normalized Lacunarity (Max Box Size)	-0.355
Porosity (%, NMR)	22.960
T_2LogMean (ms)	175.256
T_2Mode Macro (ms)	1072.430
Air k (md)	38.344
Porosity (%, He)	26.300

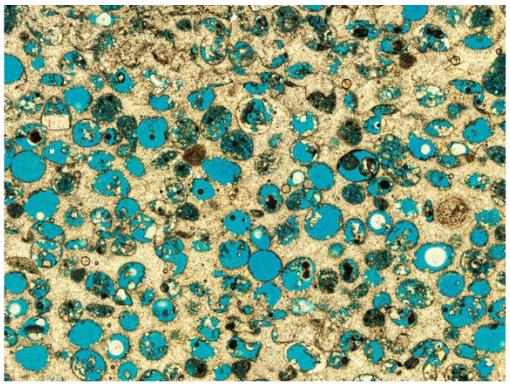

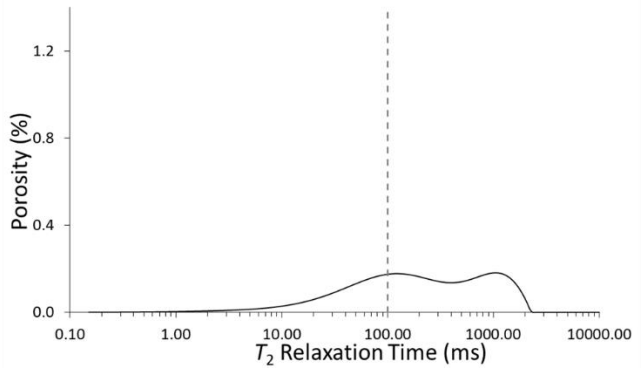

Penn 30

Grain Size (phi)	2.057
Sorting (σ)	0.272
Ooid Abundance (%)	91.097
Skeletal Abundance (%)	1.020
Intergranular Volume (%)	42.592
Cement Abundance (% of IGV)	93.478
COPL	0.614
DomSize (µm)	107.155
PoA (1/µm)	0.119
Circularity (mean)	0.173
Roundness (mean)	0.611
Compactness (med)	36.551
Lacunarity (Min Box Size)	0.844
Normalized Lacunarity (Max Box Size)	-0.828
Porosity (%, NMR)	
T_2LogMean (ms)	
T_2Mode Macro (ms)	
Air k (md)	
Porosity (%, He)	

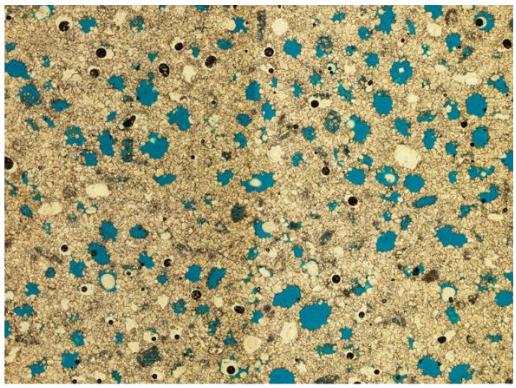

Penn 91

Grain Size (phi)	1.853
Sorting (σ)	0.311
Ooid Abundance (%)	83.334
Skeletal Abundance (%)	7.826
Intergranular Volume (%)	37.000
Cement Abundance (% of IGV)	97.500
COPL	11.749
DomSize (µm)	173.698
PoA (1/µm)	0.087
Circularity (mean)	0.141
Roundness (mean)	0.616
Compactness (med)	15.320
Lacunarity (Min Box Size)	0.627
Normalized Lacunarity (Max Box Size)	-0.614
Porosity (%, NMR)	16.050
T_2LogMean (ms)	498.927
T_2Mode Macro (ms)	1417.670
Air k (md)	0.670
Porosity (%, He)	24.900

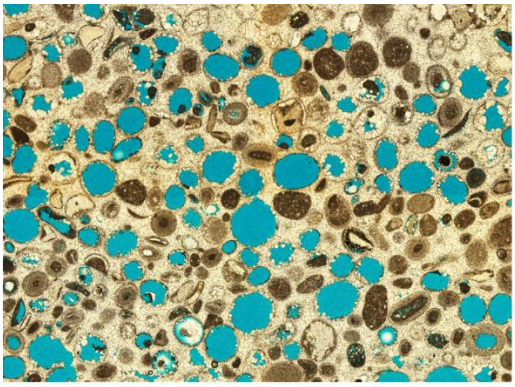

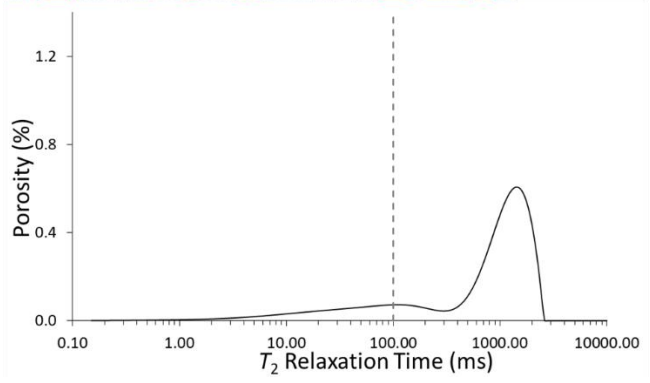

Penn 95

Grain Size (phi)	0.820
Sorting (σ)	0.459
Ooid Abundance (%)	80.851
Skeletal Abundance (%)	7.547
Intergranular Volume (%)	34.333
Cement Abundance (% of IGV)	97.321
COPL	14.714
DomSize (µm)	201.343
PoA (1/µm)	0.175
Circularity (mean)	0.105
Roundness (mean)	0.570
Compactness (med)	10.401
Lacunarity (Min Box Size)	0.906
Normalized Lacunarity (Max Box Size)	-0.844
Porosity (%, NMR)	6.620
T_2LogMean (ms)	66.863
T_2Mode Macro (ms)	
Air k (md)	0.050
Porosity (%, He)	14.900

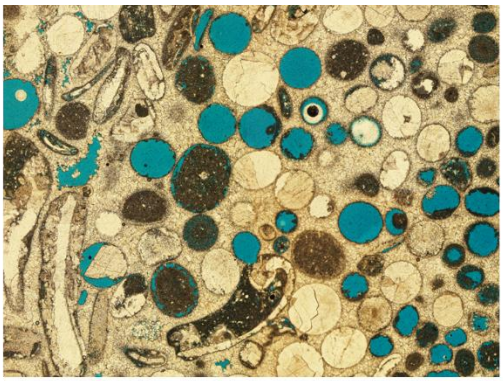

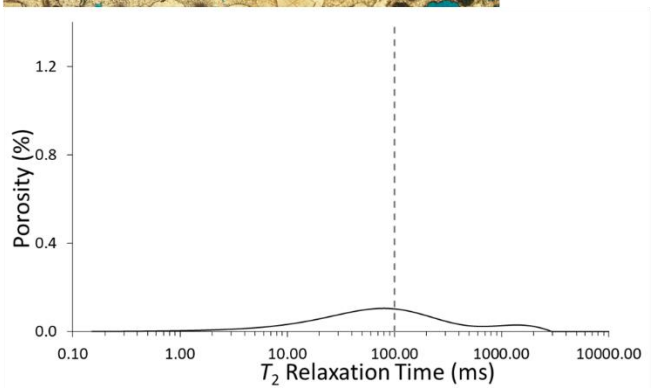

Penn 105

Grain Size (phi)	0.300
Sorting (σ)	0.625
Ooid Abundance (%)	60.407
Skeletal Abundance (%)	28.022
Intergranular Volume (%)	29.660
Cement Abundance (% of IGV)	98.968
COPL	19.457
DomSize (µm)	138.499
PoA (1/µm)	0.247
Circularity (mean)	0.129
Roundness (mean)	0.547
Compactness (med)	11.487
Lacunarity (Min Box Size)	1.074
Normalized Lacunarity (Max Box Size)	-0.918
Porosity (%, NMR)	10.660
T_2LogMean (ms)	127.911
T_2Mode Macro (ms)	
Air k (md)	3.980
Porosity (%, He)	10.000

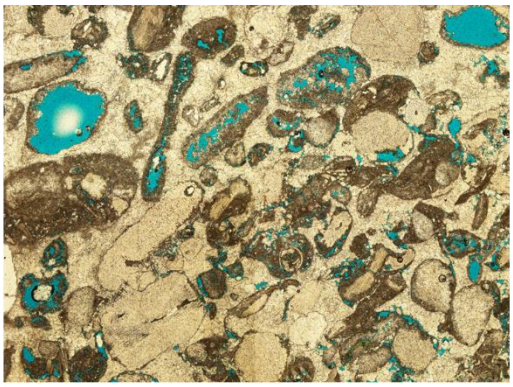

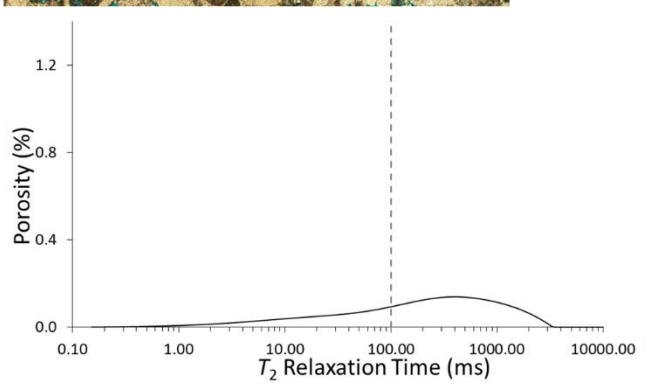

Penn 110

Grain Size (phi)	1.620
Sorting (σ)	0.390
Ooid Abundance (%)	87.574
Skeletal Abundance (%)	3.297
Intergranular Volume (%)	40.666
Cement Abundance (% of IGV)	99.237
COPL	7.318
DomSize (µm)	211.704
PoA (1/µm)	0.105
Circularity (mean)	0.101
Roundness (mean)	0.579
Compactness (med)	9.885
Lacunarity (Min Box Size)	0.551
Normalized Lacunarity (Max Box Size)	-0.522
Porosity (%, NMR)	26.430
T_2LogMean (ms)	773.034
T_2Mode Macro (ms)	1499.040
Air k (md)	0.720
Porosity (%, He)	30.000

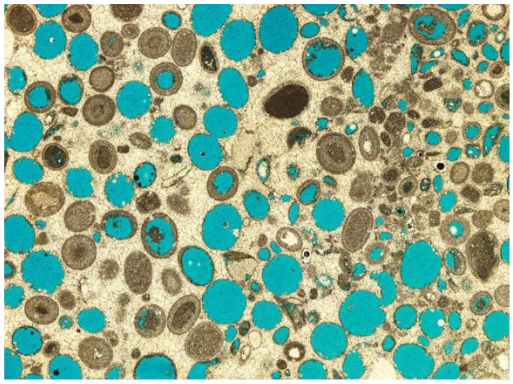

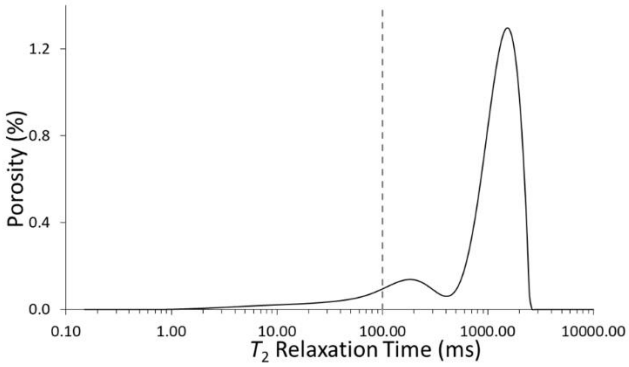

Penn 112

Grain Size (phi)	1.497
Sorting (σ)	0.410
Ooid Abundance (%)	85.393
Skeletal Abundance (%)	0.000
Intergranular Volume (%)	37.468
Cement Abundance (% of IGV)	100.000
COPL	11.207
DomSize (µm)	203.074
PoA (1/µm)	0.140
Circularity (mean)	0.090
Roundness (mean)	0.575
Compactness (med)	9.835
Lacunarity (Min Box Size)	0.767
Normalized Lacunarity (Max Box Size)	-0.682
Porosity (%, NMR)	7.370
T_2LogMean (ms)	109.031
T_2Mode Macro (ms)	
Air k (md)	0.020
Porosity (%, He)	19.300

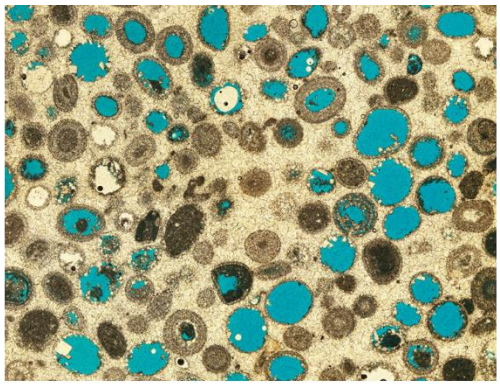

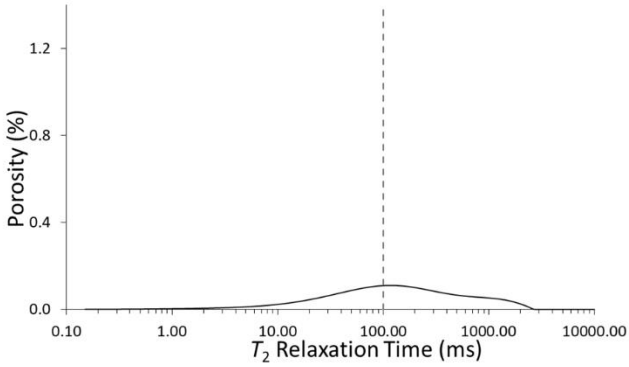

Penn 113

Grain Size (phi)	1.083
Sorting (σ)	0.248
Ooid Abundance (%)	89.756
Skeletal Abundance (%)	7.924
Intergranular Volume (%)	41.481
Cement Abundance (% of IGV)	99.249
COPL	6.272
DomSize (µm)	326.022
PoA (1/µm)	0.106
Circularity (mean)	0.128
Roundness (mean)	0.555
Compactness (med)	11.493
Lacunarity (Min Box Size)	0.541
Normalized Lacunarity (Max Box Size)	-0.510
Porosity (%, NMR)	29.240
T_2LogMean (ms)	733.519
T_2Mode Macro (ms)	1981.610
Air k (md)	39.250
Porosity (%, He)	29.900

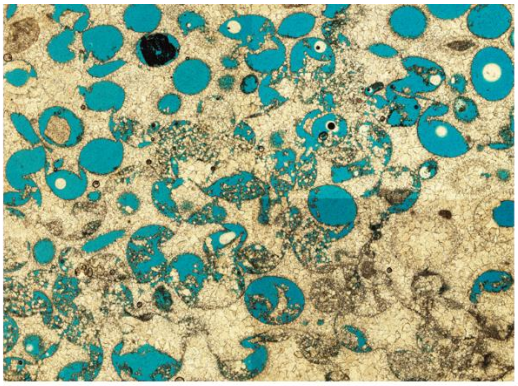

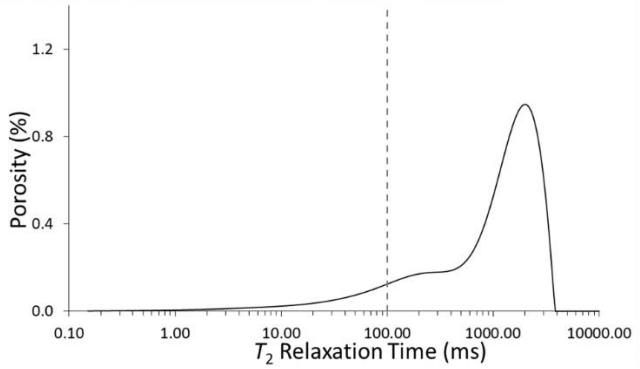

Penn 114

Grain Size (phi)	0.987
Sorting (σ)	0.374
Ooid Abundance (%)	96.570
Skeletal Abundance (%)	4.258
Intergranular Volume (%)	38.275
Cement Abundance (% of IGV)	98.374
COPL	10.257
DomSize (µm)	336.295
PoA (1/µm)	0.059
Circularity (mean)	0.198
Roundness (mean)	0.564
Compactness (med)	15.075
Lacunarity (Min Box Size)	0.469
Normalized Lacunarity (Max Box Size)	-0.437
Porosity (%, NMR)	
T_2LogMean (ms)	
T_2Mode Macro (ms)	
Air k (md)	20.283
Porosity (%, He)	30.474

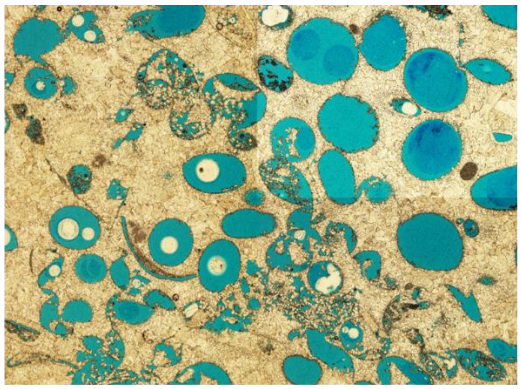

Penn 116

Grain Size (phi)	1.113
Sorting (σ)	0.329
Ooid Abundance (%)	88.890
Skeletal Abundance (%)	1.536
Intergranular Volume (%)	42.012
Cement Abundance (% of IGV)	99.395
COPL	1.695
DomSize (µm)	264.102
PoA (1/µm)	0.052
Circularity (mean)	0.180
Roundness (mean)	0.592
Compactness (med)	18.976
Lacunarity (Min Box Size)	0.464
Normalized Lacunarity (Max Box Size)	-0.434
Porosity (%, NMR)	22.940
T_2LogMean (ms)	634.159
T_2Mode Macro (ms)	1585.090
Air k (md)	24.990
Porosity (%, He)	25.800

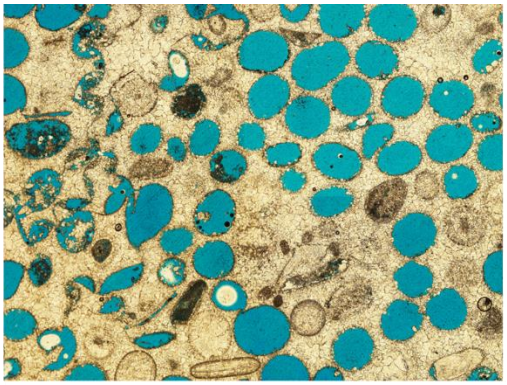

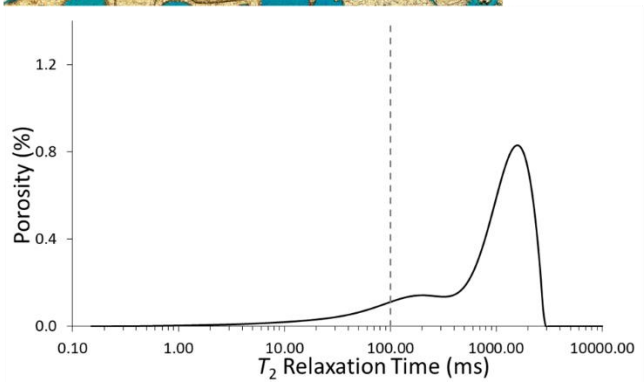

Penn 137

Grain Size (phi)	1.487
Sorting (σ)	0.378
Ooid Abundance (%)	82.032
Skeletal Abundance (%)	13.579
Intergranular Volume (%)	35.031
Cement Abundance (% of IGV)	95.395
COPL	11.000
DomSize (µm)	196.011
PoA (1/µm)	0.126
Circularity (mean)	0.117
Roundness (mean)	0.558
Compactness (med)	11.031
Lacunarity (Min Box Size)	0.609
Normalized Lacunarity (Max Box Size)	-0.587
Porosity (%, NMR)	20.430
T_2LogMean (ms)	435.013
T_2Mode Macro (ms)	1340.700
Air k (md)	21.770
Porosity (%, He)	21.400

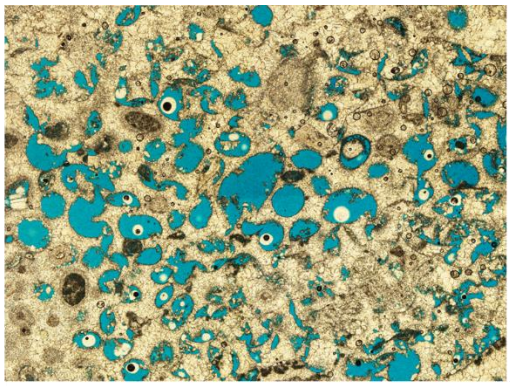

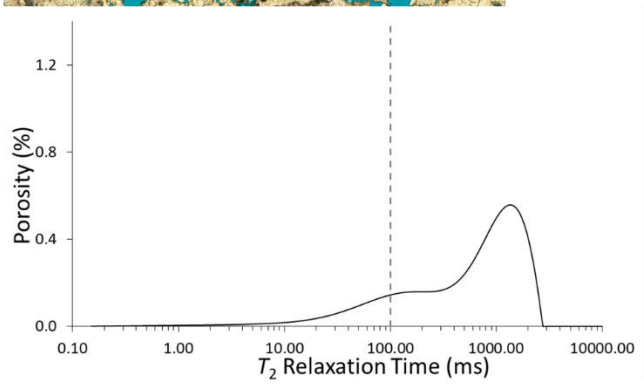

Penn 171

Grain Size (phi)	1.607
Sorting (σ)	0.863
Ooid Abundance (%)	71.262
Skeletal Abundance (%)	2.470
Intergranular Volume (%)	33.171
Cement Abundance (% of IGV)	94.117
COPL	18.109
DomSize (µm)	231.796
PoA (1/µm)	0.087
Circularity (mean)	0.154
Roundness (mean)	0.556
Compactness (med)	14.847
Lacunarity (Min Box Size)	1.329
Normalized Lacunarity (Max Box Size)	-1.094
Porosity (%, NMR)	6.320
T_2LogMean (ms)	109.704
T_2Mode Macro (ms)	1199.090
Air k (md)	0.050
Porosity (%, He)	10.400

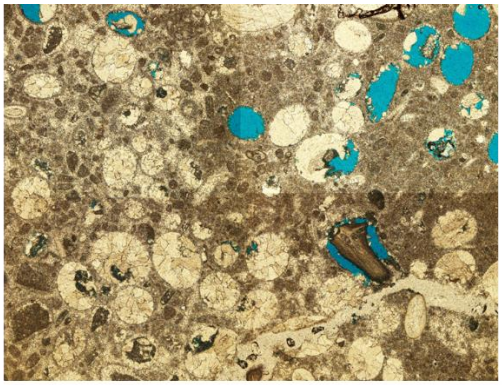

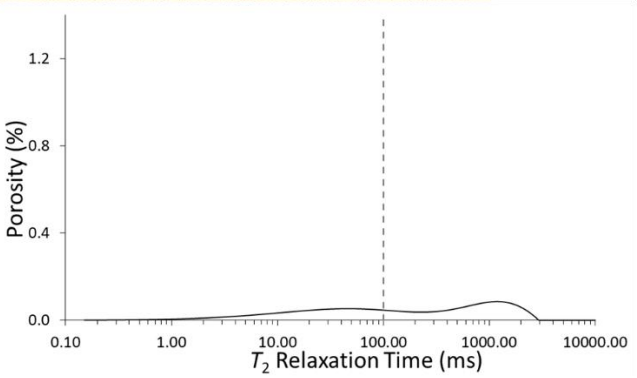

Appendix 5: Raw Data from Mississippian Samples

*Thin section photomicrographs are roughly 3.5 mm in width

M1

Grain Size (phi)	1.767
Sorting (σ)	0.499
Ooid Abundance (%)	64.602
Skeletal Abundance (%)	19.026
Intergranular Volume (%)	24.999
Cement Abundance (% of IGV)	56.002
COPL	23.348
DomSize (µm)	44.462
PoA (1/µm)	0.242
Circularity (mean)	0.285
Roundness (mean)	0.519
Compactness (med)	12.482
Lacunarity (Min Box Size)	0.917
Normalized Lacunarity (Max Box Size)	-0.905
Porosity (%, NMR)	11.700
T_2LogMean (ms)	249.554
T_2Mode Macro (ms)	1014.210
Air k (md)	82.300
Porosity (%, He)	10.294

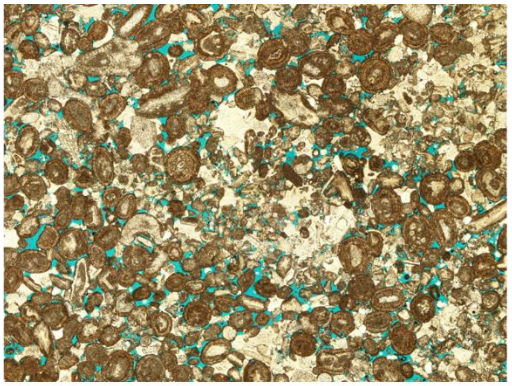

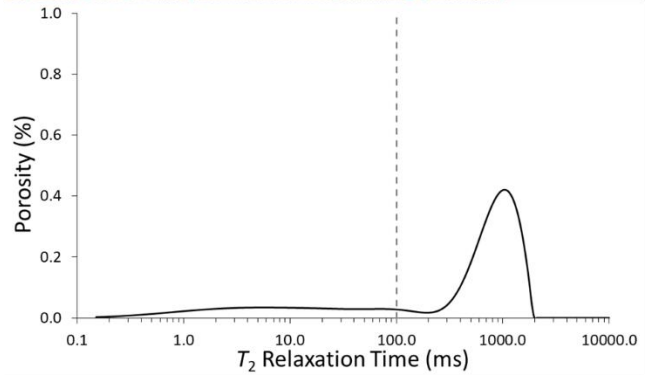

M2

Grain Size (phi)	1.673
Sorting (σ)	0.532
Ooid Abundance (%)	62.711
Skeletal Abundance (%)	27.118
Intergranular Volume (%)	22.001
Cement Abundance (% of IGV)	71.210
COPL	26.271
DomSize (µm)	43.070
PoA (1/µm)	0.250
Circularity (mean)	0.297
Roundness (mean)	0.489
Compactness (med)	12.099
Lacunarity (Min Box Size)	1.045
Normalized Lacunarity (Max Box Size)	-1.025
Porosity (%, NMR)	10.980
T_2LogMean (ms)	247.545
T_2Mode Macro (ms)	1072.430
Air k (md)	76.300
Porosity (%, He)	9.983

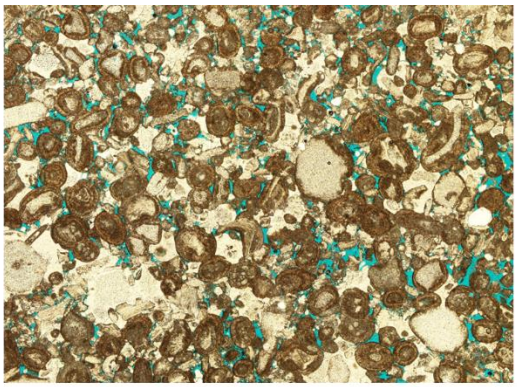

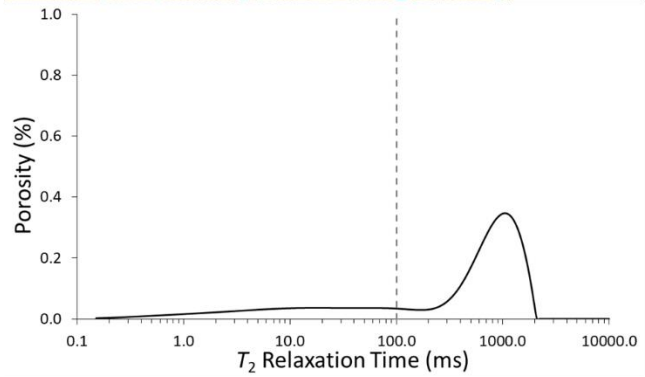

M3

Grain Size (phi)	1.630
Sorting (σ)	0.391
Ooid Abundance (%)	67.002
Skeletal Abundance (%)	15.353
Intergranular Volume (%)	18.792
Cement Abundance (% of IGV)	62.500
COPL	28.578
DomSize (µm)	51.732
PoA (1/µm)	0.242
Circularity (mean)	0.230
Roundness (mean)	0.538
Compactness (med)	13.453
Lacunarity (Min Box Size)	1.026
Normalized Lacunarity (Max Box Size)	-1.012
Porosity (%, NMR)	9.600
T_2LogMean (ms)	137.999
T_2Mode Macro (ms)	686.190
Air k (md)	37.300
Porosity (%, He)	8.665

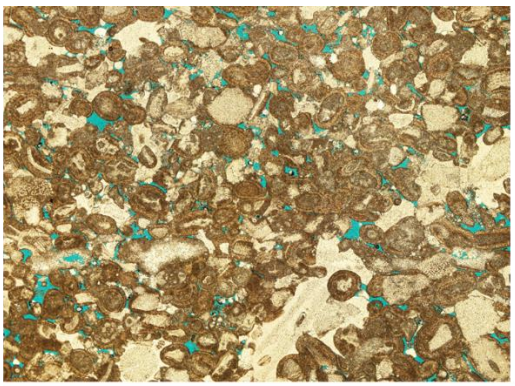

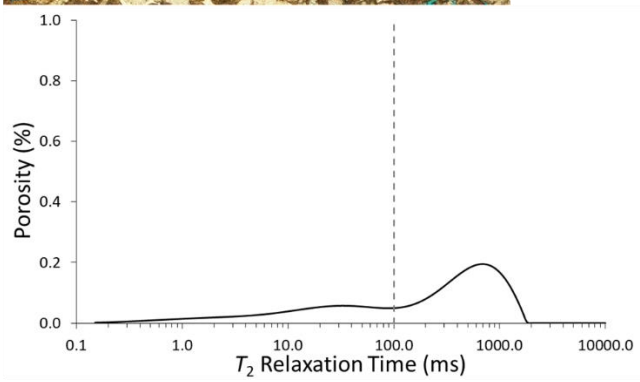

M4

Grain Size (phi)	1.340
Sorting (σ)	0.494
Ooid Abundance (%)	66.939
Skeletal Abundance (%)	24.082
Intergranular Volume (%)	18.666
Cement Abundance (% of IGV)	48.216
COPL	28.980
DomSize (µm)	98.061
PoA (1/µm)	0.131
Circularity (mean)	0.285
Roundness (mean)	0.546
Compactness (med)	18.538
Lacunarity (Min Box Size)	0.819
Normalized Lacunarity (Max Box Size)	-0.813
Porosity (%, NMR)	11.880
T_2LogMean (ms)	142.989
T_2Mode Macro (ms)	1014.210
Air k (md)	413.000
Porosity (%, He)	11.059

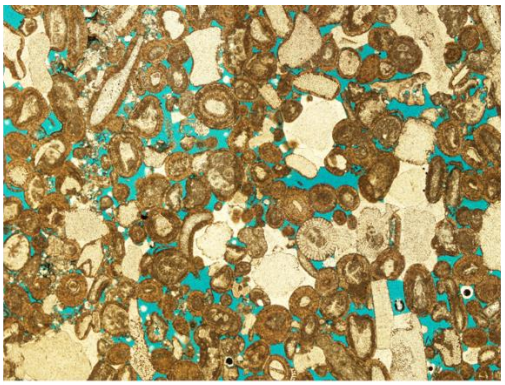

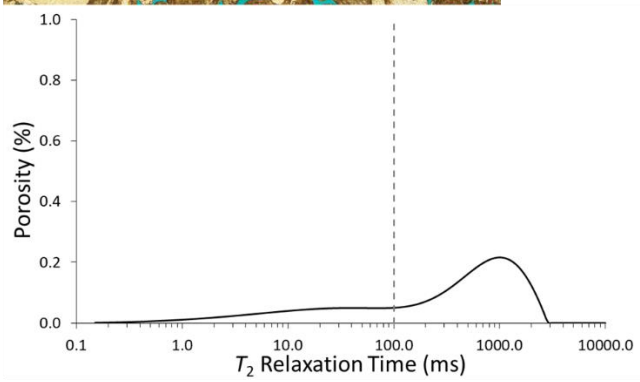

M5

Grain Size (phi)	1.550
Sorting (σ)	0.383
Ooid Abundance (%)	71.232
Skeletal Abundance (%)	19.267
Intergranular Volume (%)	27.000
Cement Abundance (% of IGV)	74.074
COPL	20.548
DomSize (µm)	74.016
PoA (1/µm)	0.166
Circularity (mean)	0.269
Roundness (mean)	0.518
Compactness (med)	15.691
Lacunarity (Min Box Size)	0.825
Normalized Lacunarity (Max Box Size)	-0.816
Porosity (%, NMR)	14.910
T_2LogMean (ms)	158.737
T_2Mode Macro (ms)	767.230
Air k (md)	
Porosity (%, He)	13.732

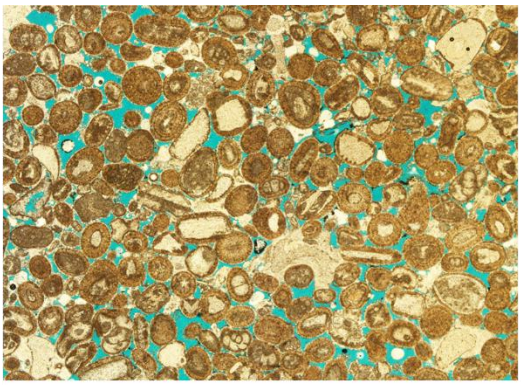

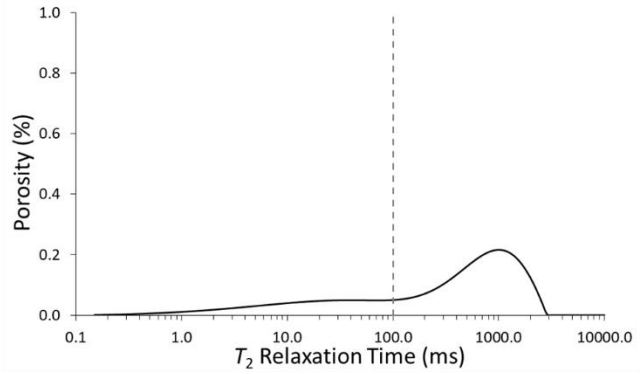

M6

Grain Size (phi)	1.730
Sorting (σ)	0.270
Ooid Abundance (%)	79.999
Skeletal Abundance (%)	10.613
Intergranular Volume (%)	18.333
Cement Abundance (% of IGV)	56.363
COPL	28.980
DomSize (µm)	98.485
PoA (1/µm)	0.190
Circularity (mean)	0.166
Roundness (mean)	0.516
Compactness (med)	16.056
Lacunarity (Min Box Size)	0.919
Normalized Lacunarity (Max Box Size)	-0.909
Porosity (%, NMR)	15.840
T_2LogMean (ms)	99.788
T_2Mode Macro (ms)	808.776
Air k (md)	416.000
Porosity (%, He)	13.268

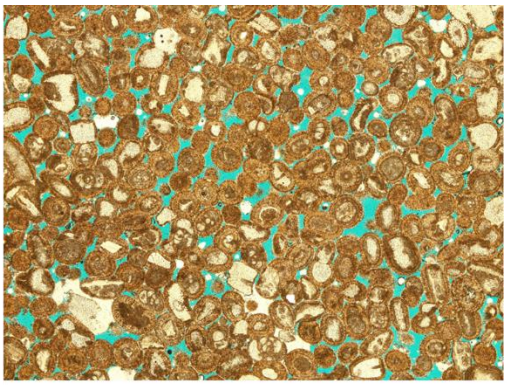

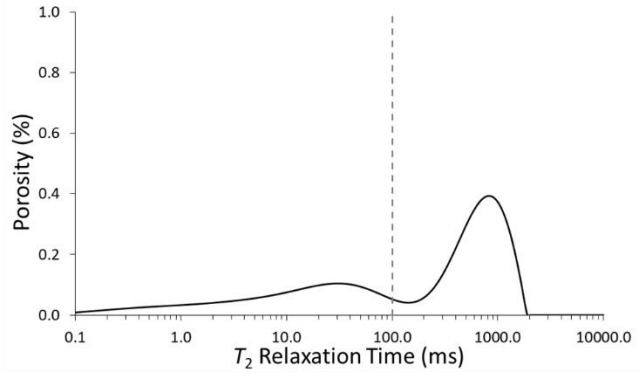

M7

Grain Size (phi)	1.453
Sorting (σ)	0.447
Ooid Abundance (%)	77.043
Skeletal Abundance (%)	14.117
Intergranular Volume (%)	13.805
Cement Abundance (% of IGV)	41.463
COPL	32.973
DomSize (µm)	94.639
PoA (1/µm)	0.203
Circularity (mean)	0.160
Roundness (mean)	0.509
Compactness (med)	14.595
Lacunarity (Min Box Size)	0.926
Normalized Lacunarity (Max Box Size)	-0.880
Porosity (%, NMR)	16.830
T_2LogMean (ms)	152.746
T_2Mode Macro (ms)	972.172
Air k (md)	
Porosity (%, He)	16.830

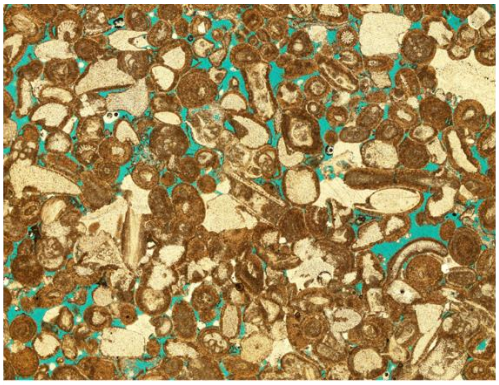

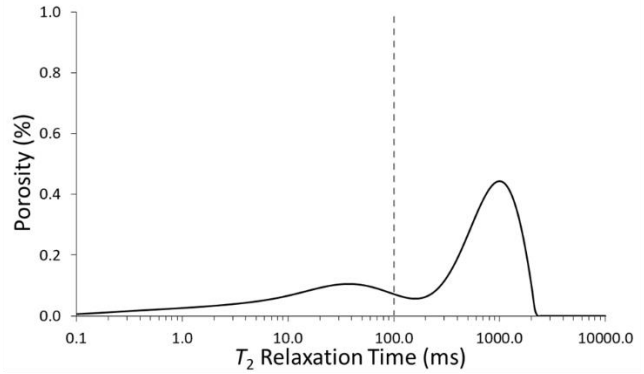

M8

Grain Size (phi)	1.487
Sorting (σ)	0.518
Ooid Abundance (%)	75.224
Skeletal Abundance (%)	14.480
Intergranular Volume (%)	26.000
Cement Abundance (% of IGV)	56.412
COPL	21.622
DomSize (µm)	117.865
PoA (1/µm)	0.168
Circularity (mean)	0.150
Roundness (mean)	0.548
Compactness (med)	18.992
Lacunarity (Min Box Size)	0.821
Normalized Lacunarity (Max Box Size)	-0.809
Porosity (%, NMR)	14.760
T_2LogMean (ms)	189.059
T_2Mode Macro (ms)	725.579
Air k (md)	597.000
Porosity (%, He)	15.285

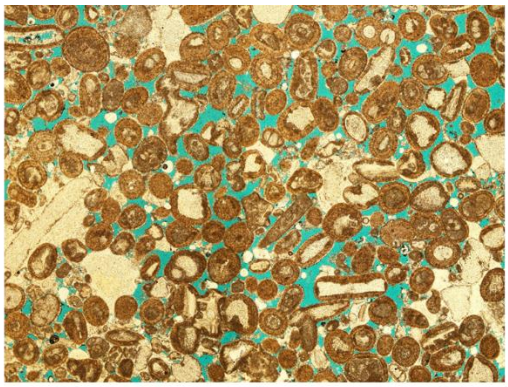

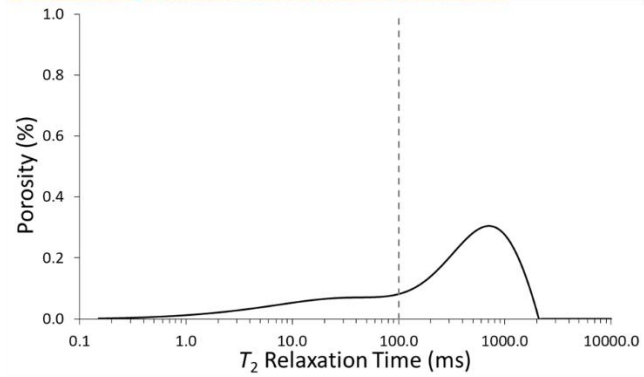

M9

Grain Size (phi)	1.407
Sorting (σ)	0.409
Ooid Abundance (%)	78.161
Skeletal Abundance (%)	16.216
Intergranular Volume (%)	12.416
Cement Abundance (% of IGV)	54.051
COPL	33.778
DomSize (µm)	91.561
PoA (1/µm)	0.199
Circularity (mean)	0.155
Roundness (mean)	0.511
Compactness (med)	16.629
Lacunarity (Min Box Size)	0.895
Normalized Lacunarity (Max Box Size)	-0.888
Porosity (%, NMR)	12.770
T_2LogMean (ms)	225.210
T_2Mode Macro (ms)	1014.210
Air k (md)	222.000
Porosity (%, He)	10.950

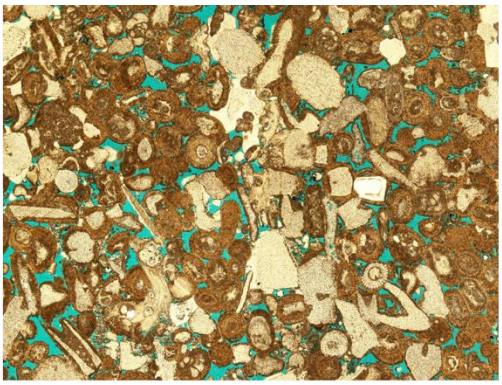

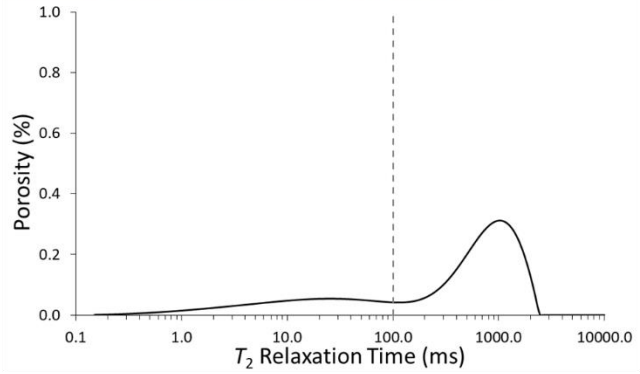

M11

Grain Size (phi)	1.527
Sorting (σ)	0.380
Ooid Abundance (%)	73.077
Skeletal Abundance (%)	23.077
Intergranular Volume (%)	27.000
Cement Abundance (% of IGV)	45.000
COPL	27.665
DomSize (µm)	161.634
PoA (1/µm)	0.114
Circularity (mean)	0.174
Roundness (mean)	0.488
Compactness (med)	16.089
Lacunarity (Min Box Size)	0.849
Normalized Lacunarity (Max Box Size)	-0.834
Porosity (%, NMR)	12.750
T_2LogMean (ms)	588.789
T_2Mode Macro (ms)	1772.300
Air k (md)	636.000
Porosity (%, He)	11.837

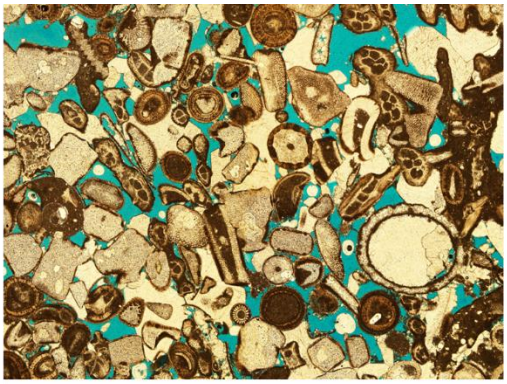

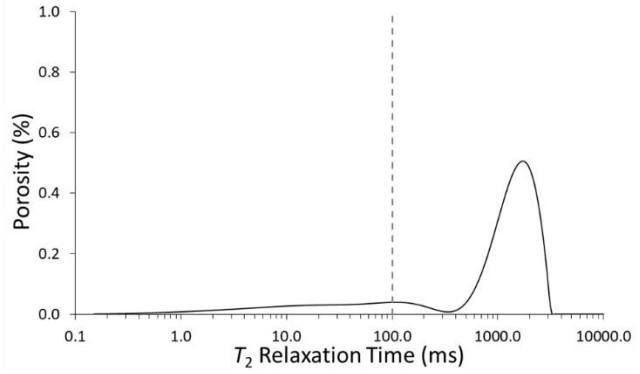

M12

Grain Size (phi)	1.643
Sorting (σ)	0.402
Ooid Abundance (%)	83.950
Skeletal Abundance (%)	6.996
Intergranular Volume (%)	18.644
Cement Abundance (% of IGV)	56.361
COPL	29.589
DomSize (µm)	92.284
PoA (1/µm)	0.197
Circularity (mean)	0.157
Roundness (mean)	0.538
Compactness (med)	15.923
Lacunarity (Min Box Size)	0.898
Normalized Lacunarity (Max Box Size)	-0.869
Porosity (%, NMR)	12.630
T_2LogMean (ms)	483.521
T_2Mode Macro (ms)	1585.090
Air k (md)	581.000
Porosity (%, He)	12.349

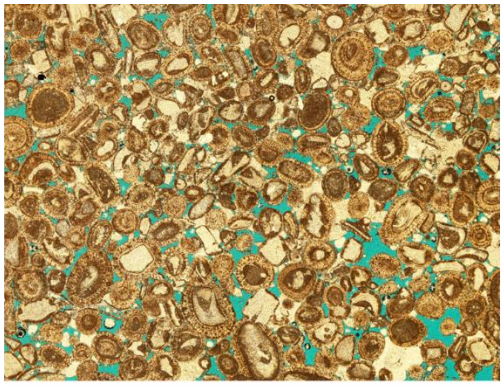

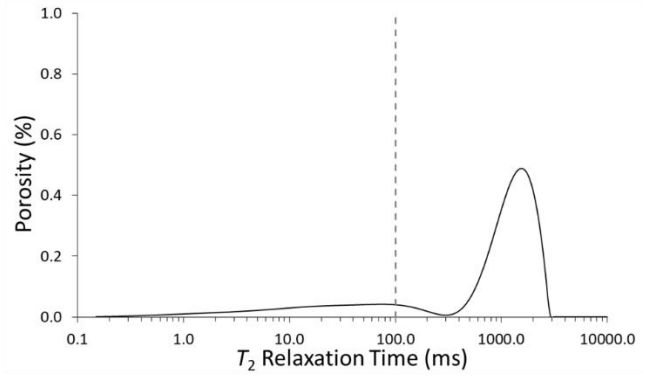

M14

Grain Size (phi)	1.367
Sorting (σ)	0.484
Ooid Abundance (%)	79.413
Skeletal Abundance (%)	7.172
Intergranular Volume (%)	26.087
Cement Abundance (% of IGV)	60.000
COPL	21.954
DomSize (µm)	94.427
PoA (1/µm)	0.225
Circularity (mean)	0.129
Roundness (mean)	0.540
Compactness (med)	20.656
Lacunarity (Min Box Size)	0.968
Normalized Lacunarity (Max Box Size)	-0.937
Porosity (%, NMR)	12.120
T_2LogMean (ms)	411.893
T_2Mode Macro (ms)	1499.040
Air k (md)	201.000
Porosity (%, He)	11.449

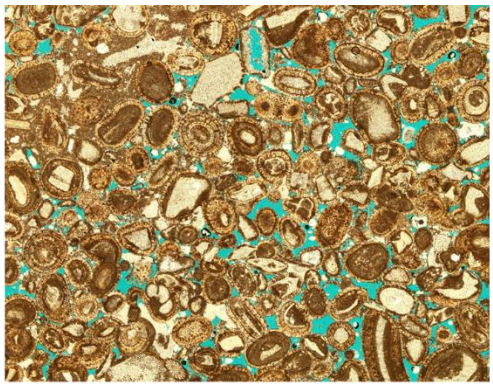

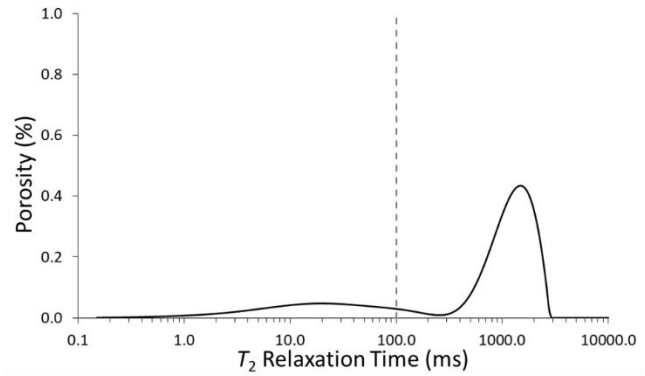

M15

Grain Size (phi)	2.297
Sorting (σ)	0.250
Ooid Abundance (%)	78.380
Skeletal Abundance (%)	10.359
Intergranular Volume (%)	25.752
Cement Abundance (% of IGV)	55.844
COPL	22.233
DomSize (µm)	82.414
PoA (1/µm)	0.233
Circularity (mean)	0.169
Roundness (mean)	0.556
Compactness (med)	15.194
Lacunarity (Min Box Size)	0.434
Normalized Lacunarity (Max Box Size)	-0.431
Porosity (%, NMR)	21.170
T_2LogMean (ms)	358.890
T_2Mode Macro (ms)	1493.520
Air k (md)	1134.000
Porosity (%, He)	19.462

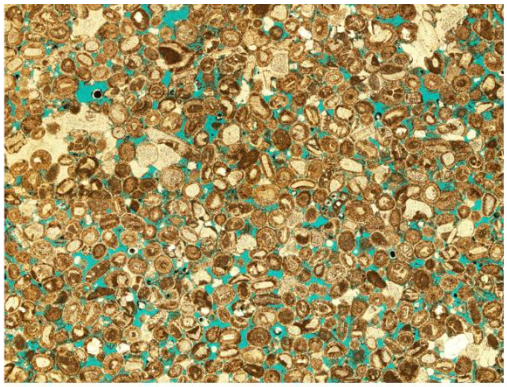

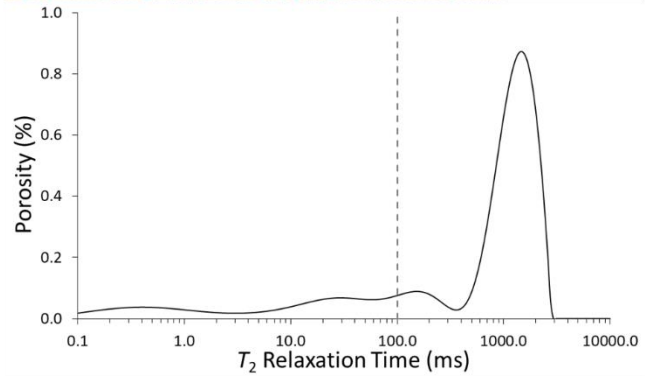

M16

Grain Size (phi)	2.423
Sorting (σ)	0.346
Ooid Abundance (%)	70.191
Skeletal Abundance (%)	13.943
Intergranular Volume (%)	31.334
Cement Abundance (% of IGV)	60.637
COPL	16.346
DomSize (µm)	69.316
PoA (1/µm)	0.242
Circularity (mean)	0.167
Roundness (mean)	0.541
Compactness (med)	15.082
Lacunarity (Min Box Size)	0.847
Normalized Lacunarity (Max Box Size)	-0.837
Porosity (%, NMR)	13.800
T_2LogMean (ms)	279.702
T_2Mode Macro (ms)	1321.100
Air k (md)	129.000
Porosity (%, He)	12.491

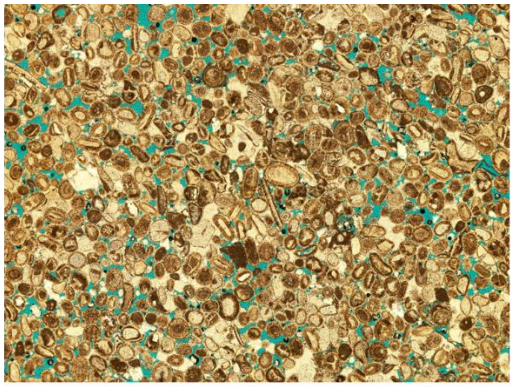

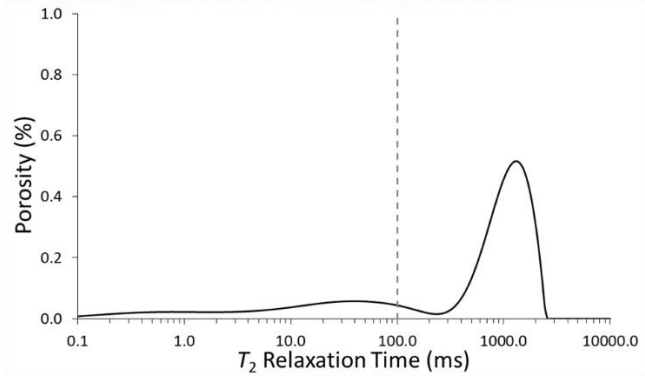

M17

Grain Size (phi)	2.180
Sorting (σ)	0.238
Ooid Abundance (%)	79.524
Skeletal Abundance (%)	8.572
Intergranular Volume (%)	30.000
Cement Abundance (% of IGV)	60.000
COPL	17.143
DomSize (µm)	81.808
PoA (1/µm)	0.199
Circularity (mean)	0.166
Roundness (mean)	0.541
Compactness (med)	18.422
Lacunarity (Min Box Size)	0.669
Normalized Lacunarity (Max Box Size)	-0.666
Porosity (%, NMR)	
T_2LogMean (ms)	
T_2Mode Macro (ms)	
Air k (md)	601.000
Porosity (%, He)	14.633

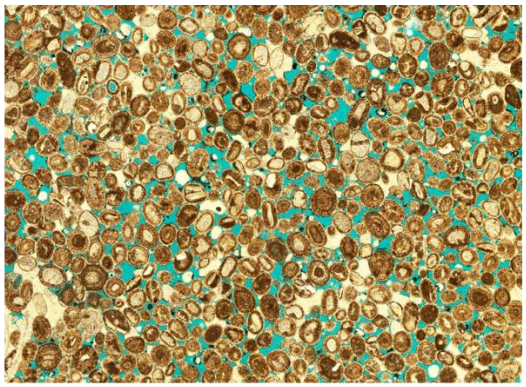

M18

Grain Size (phi)	0.817
Sorting (σ)	0.300
Ooid Abundance (%)	69.113
Skeletal Abundance (%)	27.414
Intergranular Volume (%)	14.000
Cement Abundance (% of IGV)	42.857
COPL	32.818
DomSize (µm)	187.106
PoA (1/µm)	0.104
Circularity (mean)	0.151
Roundness (mean)	0.515
Compactness (med)	19.155
Lacunarity (Min Box Size)	0.796
Normalized Lacunarity (Max Box Size)	-0.787
Porosity (%, NMR)	15.440
T_2LogMean (ms)	276.337
T_2Mode Macro (ms)	1321.100
Air k (md)	912.000
Porosity (%, He)	18.739

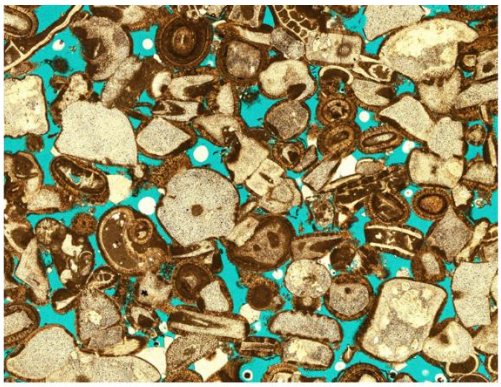

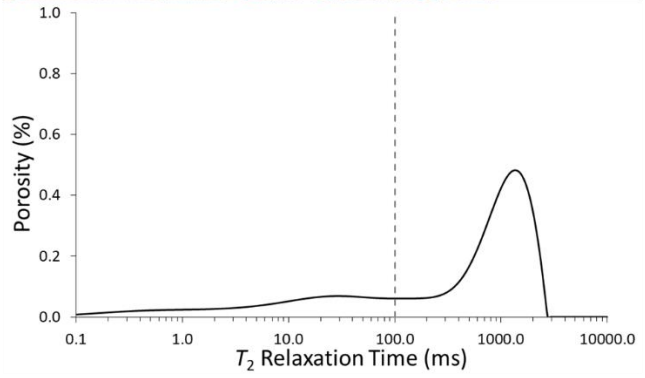

M19

Grain Size (phi)	2.237
Sorting (σ)	0.274
Ooid Abundance (%)	79.328
Skeletal Abundance (%)	8.172
Intergranular Volume (%)	30.435
Cement Abundance (% of IGV)	62.638
COPL	16.625
DomSize (µm)	81.499
PoA (1/µm)	0.209
Circularity (mean)	0.174
Roundness (mean)	0.526
Compactness (med)	13.765
Lacunarity (Min Box Size)	0.726
Normalized Lacunarity (Max Box Size)	-0.713
Porosity (%, NMR)	16.810
T_2LogMean (ms)	306.538
T_2Mode Macro (ms)	1321.100
Air k (md)	473.000
Porosity (%, He)	15.628

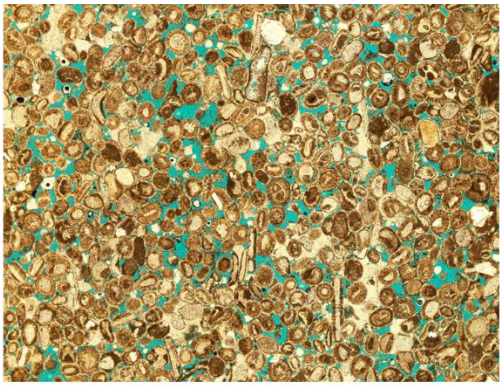

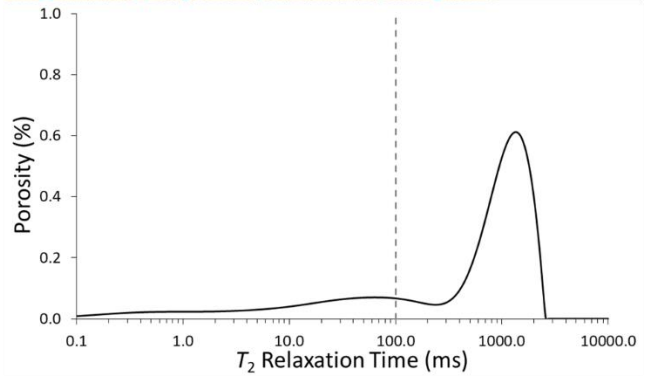

M20

Grain Size (phi)	2.323
Sorting (σ)	0.255
Ooid Abundance (%)	69.015
Skeletal Abundance (%)	16.113
Intergranular Volume (%)	30.000
Cement Abundance (% of IGV)	65.557
COPL	18.310
DomSize (µm)	68.055
PoA (1/µm)	0.198
Circularity (mean)	0.213
Roundness (mean)	0.544
Compactness (med)	16.777
Lacunarity (Min Box Size)	0.671
Normalized Lacunarity (Max Box Size)	-0.669
Porosity (%, NMR)	15.730
T_2LogMean (ms)	304.217
T_2Mode Macro (ms)	1404.670
Air k (md)	313.000
Porosity (%, He)	14.369